Chalcogenide Letters

Tech Science Press

http://doi.org/10.32604/cl.2026.086712

REVIEW

2D Chalcogenide Nanomaterial for Energy Storage Devices: Synthesis, Characterization and DFT Approach

Holy Oghenewona Ovwiurhobo[1], Marius O. Eji[2], Adil Alshoaibi[3], Ndanduleni Lethole[4], Chawki Awada[3], Shumaila Islam[3], Nisrin Alnaim[3] and Fabian I. Ezema[1,4,*]

[1]Nano Research Group, University of Nigeria, Nsukka, Enugu, Nigeria
[2]Department of Physics, Miami University, Oxford, OH, USA
[3]Department of Physics, College of Science, King Faisal University, Al Ahsa, Saudi Arabia
[4]Department of Physics, Sefako Makgatho Health Sciences University, Medunsa, South Africa
*Corresponding Author: Fabian I. Ezema. Email: fabian.ezema@unn.edu.ng

Received: 04 June 2026; Accepted: 28 August 2026; Published: 18 September 2026

ABSTRACT: Several studies have reported a growing interest in nanomaterials beyond conventional graphite, driven by the rapid global demand for sustainable, high-performance energy storage. Among these materials, two-dimensional (2D) transition metal chalcogenides (TMCs), molybdenum- and tin-based systems such as molybdenum disulfide (MoS_2) and tin (IV) disulfide (SnS_2) in particular, have emerged as promising candidates for next-generation electrochemical energy storage devices (EESDs). This is owing to their unique X-M-X sandwich architectures, tunable electronic properties, and versatile intercalation chemistry. Despite several studies on 2D TMCs and their applications in EESDs, a gap still exists, as there is no comprehensive review that integrates advanced synthesis routes and multi-scale characterization with phase engineering (particularly the 2H-to-1T transition) and defect engineering strategies, not just for MoS_2 and SnS_2 but also for other 2D TMCs (e.g., WS_2 and ReS_2), while taking advantage of Density Functional Theory (DFT) as a predictive tool for electronic structure, ion adsorption energies, and diffusion barriers. Additionally, the review examines the sustainable utilization of local mineral precursors, such as Nigerian lithium-bearing ores, for the production of 2D TMCs. Overall, this review provides a comprehensive framework for the rational design and optimization of 2D chalcogenide-based nanomaterials for high-capacity lithium-, sodium-, and potassium-ion storage devices.

KEYWORDS: 2D transition metal chalcogenides; MoS_2, phase engineering; defect engineering; density functional theory; electrochemical energy storage; intercalation kinetics

1 Introduction

Energy generation and sustainable energy storage present critical challenges for both developing and industrialized nations. While many developing countries, such as Nigeria, possess abundant natural resources for energy generation, concerns regarding the sustainability and efficient utilization of these resources persist [1]. Globally, the rapid proliferation of electric vehicles, portable electronics, and renewable energy technologies has further intensified the demand for high-performance, cost-effective, and sustainable electrochemical energy storage devices (EESDs) that offer high energy density, high power density, long cycle life, and compatibility with earth-abundant ion chemistries beyond lithium [2–5]. Conventional graphite-based anodes have historically dominated commercial batteries; however, their limited theoretical capacity and slow ion diffusion, particularly for larger Na^+ and K^+ ions, present significant obstacles for

next-generation high-power energy storage applications [6]. Among all the potential materials used for electrochemical energy storage, 2D TMCs, which are currently considered one of the most promising material platforms for such applications, have attracted greater interest from researchers to alleviate these limitations. Their layered van der Waals structure, customizable electrical characteristics, high theoretical surface area, adjustable interlayer spacing, and remarkable chemical adaptability across many compositions and crystal phases are all credited with this promise [7–9]. Reversible intercalation, conversion, and pseudocapacitive storage of Li^+, Na^+, and K^+ ions are possible due to the unique X-M-X layered configuration that provides electrochemically accessible sites in large quantities while promoting rapid intercalation and adsorption of ions [5,7,10–12]. High surface-to-volume ratios and the tunability of interlayer spacing in materials such as MoS_2, WS_2, and SnS_2 provide improved ion transport rates and electrochemical access.

Besides the two-dimensional morphology, the outstanding electrochemical behavior of 2D TMCs is attributed to the evolution of structure and composition of those materials [13]. This structural diversity is caused by the coexistence of metastable and thermodynamically stable crystalline phases with different electrical properties. For group-6 TMCs, including MoS_2 and WS_2, the semiconducting 2H phase that has trigonal prismatic coordination of transition metal atoms is the thermodynamic ground state [14,15]. In turn, the metastable metallic 1T phase with octahedral metal coordination is very suitable for fast electrochemical processes owing to enhanced electronic conductivity and decreased ion diffusion barriers [7,15,16]. Consequently, precise control over crystal phase transformation, particularly the conversion from the semiconducting 2H phase to the metallic 1T phase, together with the intentional introduction of atomic defects such as chalcogen vacancies, has emerged as one of the most effective strategies for improving electronic conductivity, increasing active sites, and accelerating ion transport [10,17,18] (see Fig. 1).

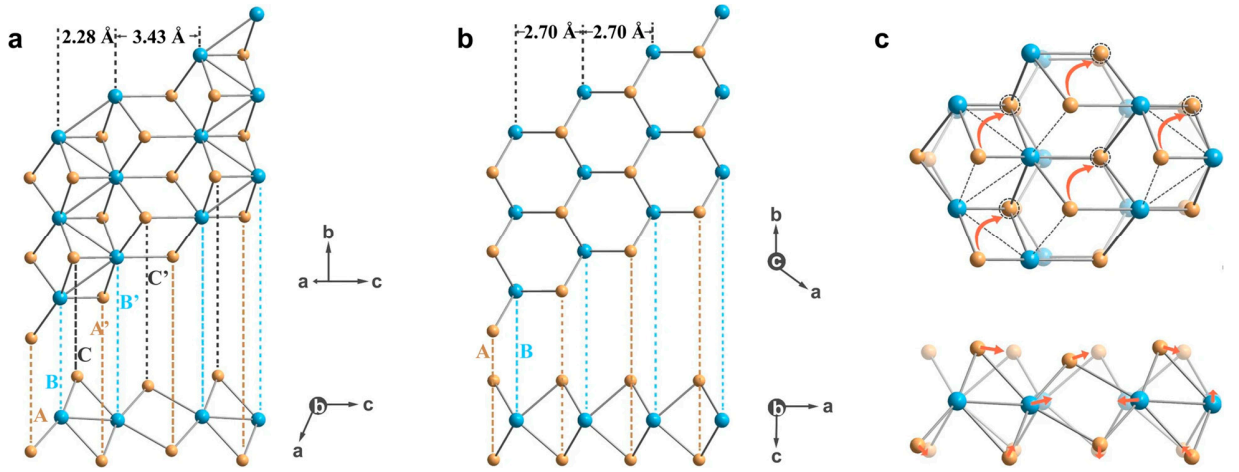

Figure 1: (**a**) Crystal structures of 1T′ WS_2, where W and S atoms coordinate in an octahedral configuration and stack in an A/A'-B/B'-C/C' mode. (**b**) Crystal structures of 1H WS_2, where W and S atoms coordinate in a trigonal prismatic configuration and stack in an A-B-A mode. (**c**) Top view (upper) and side view (lower) of crystal lattices when overlapping of a layer of 1T′ WS_2 on top of a layer of 1H WS_2. Color code: blue and orange spheres represent W and S, respectively. The broken W–W and W–S bonds are labeled by dash lines, and the directions of W and S atoms displacements are indicated by orange arrows. Each S atom that dissociates from a W atom after breaking the W–S bond moves to a new position (marked by a dotted line circle) and forms a new W–S bond. Reproduced from [19] under a Creative Commons Attribution 3.0 Unported Licence.

Beyond the well-researched MoS_2 systems, the variety of 2D chalcogenides has been greatly expanded by recent breakthroughs. Vanadium chalcogenides like VS_2 and VSe_2, rhenium-based layered compounds with intrinsically anisotropic crystal structures, and selenium-based materials like WSe_2, $SnSe_2$, and $ReSe_2$ display special combinations of orbital hybridization, chalcogen polarizability, interlayer spacing, and phase stability that are not possible in sulfide-only compositions [11,17]. Several of these materials provide electrochemical performances that are comparable to or better than those of traditional MoS_2 in certain ion-storage applications, according to experimental and theoretical studies [20,21]. Thus, heterointerface engineering successfully suppresses nanosheet restacking, minimizes phase reversion, permits volumetric expansion during cycling, and produces electrochemical performances better than those of the individual components [2,18,22]. his is demonstrated by the development of mixed-dimensional hybrid architectures that combine 2D chalcogenides with graphene, carbon nanotubes, metal oxides, and metal-organic frameworks.

Significant advancements in synthesizing techniques have been accomplished concurrently with these experimental discoveries. While bottom-up methods like chemical vapor deposition (CVD), hydrothermal synthesis, and solvothermal synthesis offer better control over crystal quality, layer thickness, morphology, defect concentration, and phase purity, top-down methods like liquid-phase exfoliation offer scalable production of few-layer nanosheets [23,24]. However, despite significant advancements in experimental synthesis, understanding the atomistic mechanisms behind crystal growth, defect formation, phase evolution, and electrochemical activity remains a fundamental challenge.

As a result, Density Functional Theory (DFT) has developed from a post-synthesis interpretive tool into predictive design software that helps with electrochemical performance engineering, materials discovery, and synthesis optimization [3,25,26]. DFT uses charge-density difference analysis, Bader charge partitioning, projected density of states (PDOS), crystal orbital Hamilton population (COHP) analysis, and nudged elastic band (NEB) calculations in addition to standard calculations of adsorption energies and ion diffusion barriers to uncover the atomistic origins of charge transfer, chemical bonding, diffusion pathways, and redox behavior [3,25,27]. By facilitating effective exploration of compositional and structural design areas that are otherwise unreachable through experimentation alone, the recent integration of DFT with machine-learning algorithms has further expedited computational materials discovery [25,28]. As a result, DFT is being used as a theoretical microscope to anticipate new high-performance chalcogenide compositions before production and to supplement experimental characterization [28,29].

Despite these impressive developments, a number of significant obstacles still stand in the way of turning laboratory-scale findings into useful energy storage solutions. Due to differences in phase composition, defect density, layer thickness, and microstructural uniformity, electrochemical performance frequently varies significantly between nominally identical synthesis protocols, with two- to five-fold differences commonly reported across independent laboratories [30–32]. Furthermore, despite a number of stabilization techniques, the intrinsic trade-off between improved electrochemical performance and long-term structural stability is created by the thermodynamic metastability of the metallic 1T phase [10,15]. Comparably, there are still few systematic quantitative comparisons between sulfide and selenide chalcogenides across various alkali-ion chemistries, and little is known about the atomistic mechanisms controlling potassium-ion storage, which is distinguished by a larger ionic radius, higher diffusion barriers, and greater volumetric expansion than lithium or sodium [3,5,21,29].

This research work combines the practical outcomes with theoretical insights derived from Density Functional Theory for a critical assessment of recent advances in 2D transition metal chalcogenides as electrochemical energy storage materials. The mechanisms of interaction between phase engineering, defect chemistry, and ion diffusion; the thermodynamic limitations of the metallic 1T phase; comparisons

of the storage mechanisms of Li^+, Na^+, and K^+; benchmarking sulfides and selenide chalcogenides; and design strategies for hybrid electrode systems are all discussed. To offer a comprehensive and useful framework for rational design of the next generation of 2D chalcogenide-based electrochemical energy storage systems, the current obstacles, future perspectives and opportunities, including local mining sources, are finally addressed.

2 2D Chalcogenide Nanomaterials

2.1 Definition and Dimensionality in Nanoscale TMCs

The term two-dimensional (2D) chalcogenide nanomaterials is reserved for inorganic compounds with anisotropic bonding, comprising very strong in-plane covalent bonding but relatively weaker out-of-plane van der Waals bonding. The distinctive feature of these compounds is that the layered or chain-type structure leads to anisotropic optical, electrical, and physical properties [11,14]. The TMC, designated as MX_2, where M is the transition metal and X is the chalcogen, is considered a nanomaterial when its thickness is reduced to the atomic level (100 nm or lower).

At this thickness, electron confinement leads to an indirect-to-direct transition of bandgaps in compounds such as MoS_2, affecting their redox potential, thus making them more suitable for use as an energy storage material. The higher theoretical capacity of TMCs compared with their bulk analog is associated with this transformation [13].

2.2 Comparison of TMCs with Other 2D Nanomaterials

The 2D era was pioneered by numerous other 2D nanomaterials. Graphene is among the most well-known. Highly regarded and thoroughly investigated, graphene is suitable for nearly every use in materials science, including the regeneration of bone tissue [8]. One issue with graphene, however, is that it lacks the chemical diversity needed for sophisticated electrochemical storage. This is because graphene's sp2-hybridized carbon atoms make it chemically inert. Despite its superior electron transport capabilities, it is unable to store large amounts of energy through redox processes due to the absence of surface functional groups [18]. This gap is filled by 2D chalcogenide nanomaterials, which offer:

- **Variable Oxidation States:** Transition metals in TMCs can exist in a variety of oxidation states, such as Mo^{4+} to Mo^{6+}, which enables faradaic (battery-like) charge storage that graphene is unable to accomplish.
- **Polymorphism:** TMC nanoparticles can exist in several structural phases, such as 2H, 1T, and 1T′, in contrast to graphene's inflexible hexagonal lattice. DFT is essential for predicting which phase will offer optimal electronic conductivity for a given battery chemistry [25].

2.3 Advantages of Nanostructuring for Electrochemical Energy Storage Devices (EESDs)

Electrochemical Energy Storage Devices (EESDs) are one of the key areas where 2D chalcogenide nanomaterials are applied. This is due to their unique nanoscale architecture resulting from shortened diffusion pathways. For instance, by reducing the material thickness to a few nanometers, the diffusion distance for ions (Li^+, Na^+) is minimized, leading to ultra-fast charging capabilities [21].

Furthermore, nanomaterials have a high percentage of atoms residing on the surface, leading to a shift in the energy storage mechanism from slow, bulk-controlled diffusion to fast, surface-controlled pseudocapacitance. This is known as surface-dominated kinetics. Additionally, another unique architectural feature is defect density. This comes into play when synthesizing at the nanoscale, allowing the precise

introduction of chalcogen vacancies. These vacancies serve as 'hotspots' that reduce the adsorption energy of ions, thereby increasing the overall energy density of the storage device [17,21].

2.4 Atomic and Crystal Structure

2.4.1 The X-M-X Sandwich Layering

Various layers, including monolayer, bilayer, and trilayer, form part of the 2D chalcogenide nanomaterials. The trilayer structure, which involves two outside layers of chalcogen anions (X) surrounding the middle layer of transition metal atoms (M), is a distinct property of these materials. Different coordination symmetry among the metals (such as molybdenum sulfide MoS_2, and titanium diselenide $TiSe_2$ or the post-transition metal in tin sulfide SnS_2) defines these properties.

The thickness of a single tri-layer is approximately 0.6 to 0.7 nm, but the true potential for energy storage lies in the van der Waals gallery—the physical gap between these sandwiches. Unlike other 2D materials, the layers are held together by weak dispersion forces rather than ionic or covalent bonds. This allows the lattice to "breathe" during the insertion of large ions, providing excellent structural flexibility and resilience during repeated charge-discharge cycles [11] (see Fig. 2).

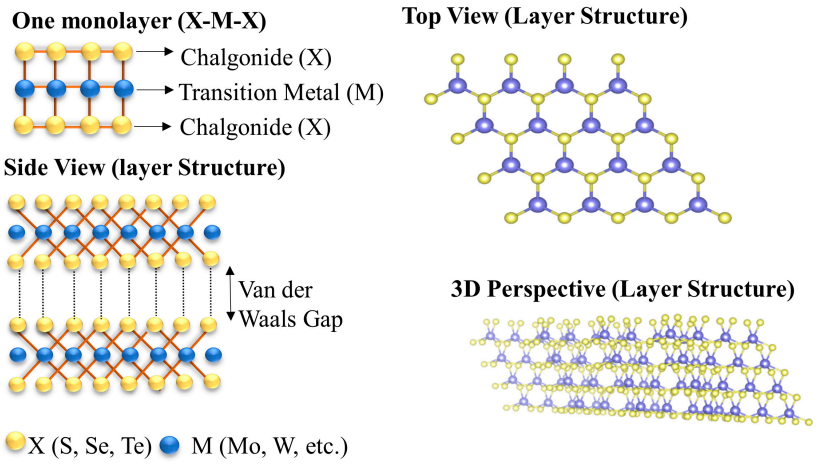

Figure 2: Schematic illustration of the X-M-X sandwich layered structure of two-dimensional transition metal chalcogenides (e.g., MoS_2), showing in-plane covalent bonding and interlayer van der Waals gap. Adapted from [11].

2.4.2 Intralayer Covalent Bonding vs. Interlayer van der Waals Forces

Nanomaterials, especially 2D chalcogenides, derive their chemical stability from the strong in-plane covalent bonding between the d-orbitals of metals and chalcogen p-orbitals. The high-energy bonds derived from this structure ensure that nanosheets remain intact during high-rate charge or discharge cycles [14,33].

Additionally, the weak interlayer van der Waals forces represent a low energy barrier for ion diffusion. Lu et al. [34] showed that by calculating the cleavage (exfoliation) energy of these layers using a DFT approach, researchers can identify which TMCs are the most easily exfoliated. The findings from their research suggest that materials with lower cleavage energies are easier to synthesize into 2D forms and offer faster pathways for alkali metal (e.g., Na^+ and K^+) ion transport.

2.4.3 Coordination Geometries: Trigonal Prismatic vs. Octahedral

One unique aspect of the atomic arrangement of transition metals is that they are not fixed, meaning mobile electrons dictate a material's electronic personality [35]. Two major phases exist with regard to

coordination geometries of 2D chalcogenide nanomaterials: trigonal prismatic (2H phase) and octahedral (1T phase). In the 2H phase, metal atoms are coordinated by six chalcogens in a D_{3h} symmetry. Such an arrangement leads to the splitting of the d-orbitals, creating a bandgap and making the material a semiconductor. On the other hand, in the 1T phase, metal atoms are coordinated in an octahedral geometry. This leads to overlapping of electronic states at the Fermi level, resulting in metallic behavior [35,36].

In recent times, there has been more focus on structural development. One such study highlighted the transition from the 2H to 1T phase structure as a result of a subtle glide of one chalcogen plane [37]. This structural glide is energy intensive, and their study provides a new DFT-based roadmap for lowering this transition energy through the introduction of specific lattice strains, which is vital for creating highly conductive electrodes needed in high-power supercapacitors (see Fig. 3).

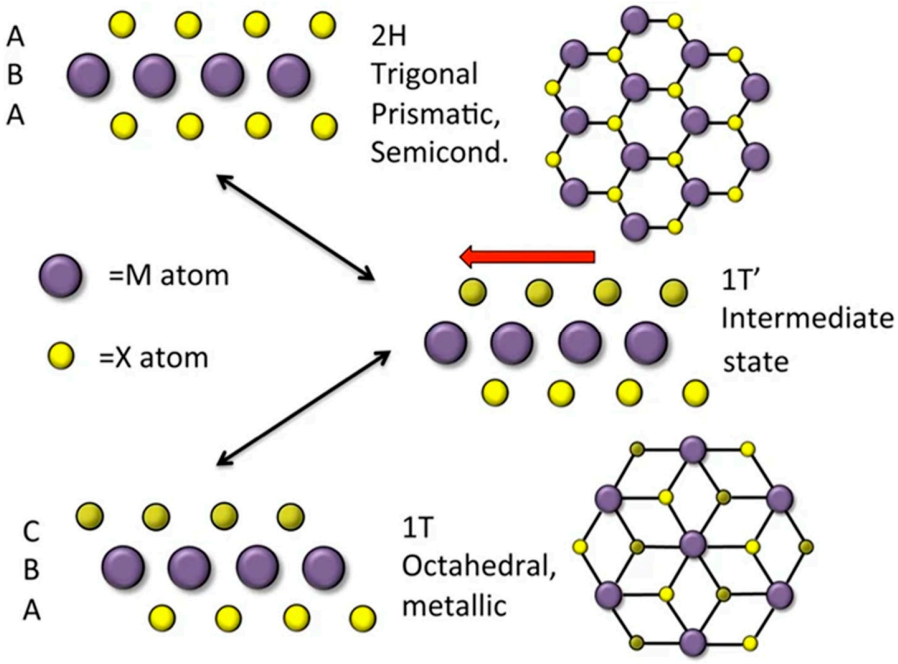

Figure 3: Model of the 2H-1T phase transition in MoX_2 films. The 2H phase is trigonal prismatic and the material is a semiconductor. The 1T phase is octahedral and the material is metallic. The 1T′ phase is an intermediate state. Reproduce from [35] under a Creative Commons Attribution (CC BY 4.0) license.

2.5 Phase Engineering, Defect Chemistry, and Their Coupled Mechanistic Framework in 2D Chalcogenides

Phase engineering is the manipulation of the atomic arrangement within a 2D lattice to tune its electronic conductivity and electrochemical reactivity. Phase engineering of 2D materials not only covers conventional structural and metal-insulator transitions but also magnetic states, strongly correlated band structures, and topological phases [38]. Li et al. [17] demonstrated that strategic phase engineering of TMDs (particularly the 2H to 1T transition) significantly enhances their performance in surface-enhanced Raman scattering (SERS) due to improved electronic conductivity and charge transfer in the metallic 1T phase. These results demonstrate how phase control can be used to customize electrical characteristics for a variety of uses, such as electrochemical energy storage.

Defect engineering and phase engineering have been separately discussed as two different techniques that can be applied to enhance the electrochemical properties of 2D transition metal chalcogenides. However,

it is important to note that there is no clear-cut distinction between these two phenomena from a mechanical perspective. Defects in the lattice, lattice strains, and phase changes are interrelated phenomena at the atomistic level, all of which regulate the charge-storing capacity, ion transport kinetics, and electronic structure of these materials.

The principal issue related to the application of the DFT approach is the capability of the 2D chalcogenide nanomaterials to undergo phase transitions between semiconductor and metal phases. This factor dictates the efficiency of electron transfer during the charging process.

2.5.1 The 2H to 1T Transition: Structural Mechanism and Energy Landscape

In TMCs such as MoS_2, the 2H to 1T phase transition is marked by an ordered glide of the chalcogen plane relative to the core metal layer. As a consequence, the coordination of the metal is changed from trigonal prismatic (D_{3h}) to octahedral (O_h) symmetry. It involves more than mere rearrangement of geometry; rather, it involves the rearrangement of the d-orbital splitting of the transition metal, resulting in the reduction of the band gap in the 2H phase and the emergence of degenerate states in the 1T phase at the Fermi level, responsible for the metallic character of the 1T phase. The energy barrier for the 2H to 1T phase transition in pristine MoS_2 is calculated using density functional theory (DFT) to be around 0.84 eV per formula unit under ambient conditions [39].

2.5.2 Influence of Chalcogen Vacancies on Transition Barrier and Electronic Structure

The chalcogen vacancies disturb the symmetry of the crystal field in which the metal ion is located and thus act as effective structural defects that facilitate the 2H to 1T transformation. Coordination of the molybdenum atom in the vicinity of the defect changes from trigonal prismatic to pentagonal due to the creation of the sulfur vacancy in MoS_2. Even before a full structural transition takes place, this local symmetry breaking provides mid-gap electronic states that partially occupy the conduction band minimum, moving the Fermi level into the metallic regime [40,41].

Sulfur vacancies lower the effective 2H to 1T transition barrier by up to 0.3 eV when compared to the pristine lattice, according to DFT simulations utilizing the nudged elastic band (NEB) approach. This reduction occurs because the bonding environment of the vacancy-perturbed metal center is already asymmetrically distorted, requiring less mechanical effort to undergo chalcogen plane glide. Interestingly, the structural change is preceded and facilitated by the electronic reconfiguration caused by vacancies, suggesting that phase engineering and defect engineering are simultaneous processes functioning within the same atomic framework [40,41].

Chalcogen vacancies modify ion transport via three mechanistically different routes in addition to decreasing the transition barrier. First, the adsorption energy of alkali metal ions is greatly decreased by the localized electrostatic wells that vacancies produce at the material's surface. According to DFT estimates, the adsorption energies for Li^+ on defect-engineered MoS_2 vary from about −1.8 to −3.2 eV, depending on the number of vacancies, while on pristine 2H-MoS_2 they are about −1.2 eV. This differential provides a significant thermodynamic driving force for ion uptake. Second, the diffusion barrier for ion migration along the interlayer gallery is directly lowered by the local expansion of the interlayer van der Waals spacing caused by lattice distortion surrounding each vacancy. Third, local charge-transfer kinetics at the electrode-electrolyte interface are improved by the somewhat metallic electronic character generated by vacancy-associated mid-gap states, which lowers the charge-transfer resistance as determined by electrochemical impedance spectroscopy. Ion adsorption, interlayer accessibility, and charge transfer are all simultaneously enhanced by vacancy-driven electronic structural alteration; these effects are synergistic rather than additive.

Defect-engineered transition metal chalcogenide (TMC) electrodes routinely outperform both pristine 2H-phase and chemically converted 1T-phase counterparts in electrochemical benchmarking studies, which can be explained by this synergy [42].

2.5.3 The Role of Lattice Strain as a Coupled Variable

In this concept, lattice strain is a third mechanistically related variable. Similar to vacancy formation, biaxial tensile strain acts at a collective rather than a local scale, changing chalcogen-metal bond lengths and weakening the crystal field splitting energy through substrate engineering, heterostructure growth, or mechanical bending. According to DFT simulations, the 2H to 1T transition barrier can be lowered below the thermal energy available at moderate processing temperatures with a biaxial tensile strain of roughly 3 to 5%, allowing strain-assisted phase conversion without the need for chemical intercalation or high synthesis temperatures [15,43,44]. Tensile strain not only promotes phase conversion but also raises the interlayer van der Waals gap in MoS_2 above its native value of about 0.62 nm. For big ions like Na^+ and K^+, whose ionic radii would ordinarily result in considerable intercalation stress and structural deterioration during repeated charge-discharge cycling, this expansion immediately lowers the diffusion barrier [45–47].

Instead of acting individually, strain and vacancies work together. Because the local lattice weakening close to defect sites increases the bond-length response to applied strain, vacancy-rich regions show increased strain sensitivity. This implies that local phase conversion in vacancy-dense domains can be triggered by even small substrate-induced strain, leaving vacancy-free regions in the thermodynamically stable 2H phase. The outcome is a spatially heterogeneous electrode microstructure where semiconducting 2H and metallic 1T domains coexist. Electrochemically, such microstructural coexistence is beneficial: 2H domains offer chemical stability and structural integrity during repeated cycling, whereas 1T domains give excellent electronic conductivity and quick charge-transfer kinetics. By simultaneously designing vacancy concentration and applied strain within a single design strategy, it is possible to adjust the percentage of these domains and, consequently, the overall electrochemical performance [43,48,49].

2.5.4 Unified Mechanistic Framework

Chalcogen vacancies, lattice strain, and the 2H to 1T phase transition are not three distinct engineering factors, but rather an interrelated trinity, as shown by the mechanistic linkages described above. The presence of vacancies modifies the density of electronic states and reduces the transition energy barrier. This is further enhanced and locally modulated by strain. All these three parameters, namely charge transfer resistance, kinetics of diffusion, and ion adsorption energy, are simultaneously regulated by the resulting phase composition. In this regard, instead of individually fine-tuning all three parameters, they need to be optimized simultaneously through a single DFT-based design methodology to optimize the electrochemical activity of the two-dimensional chalcogenides [50–52]. The preparation process, characterization procedures, and theoretical modeling discussed in the following sections are rooted in this perspective.

2.6 Thermodynamic Metastability of the 1T Phase: Stability Limits, Phase Reversion, and Cycling Degradation

In Section 2.5, we have seen some of the known electrochemical advantages of the metallic 1T phase in 2D transition metal chalcogenides. The metastability of the 1T phase relative to the 2H phase from a thermodynamic point of view, under ambient and electrochemical operating conditions, is an important yet often overlooked limitation. The thermodynamic driving force for reversion to the 2H phase, the

experimental evidence of phase degradation upon cycling, and the effects that such instability would have on the long-term behavior of devices must be considered for 1T-phase TMDCs [53].

2.6.1 Thermodynamic Basis of 1T Phase Metastability

The position of the 1T phase on the energy surface of TMC polymorphs plays a critical role in determining the metastability of the materials. In the case of group-6 TMCs such as MoS_2 and WS_2, DFT calculations have revealed that the total energy of the 1T phase is higher than the 2H phase energy by 0.2 to 0.8 eV per formula unit. This range depends on both the nature of the chalcogen and the method of computation [54–57]. Because of the energy difference, the 1T phase cannot be a thermodynamic ground state but occupies a local energy minimum that is isolated from the 2H global minimum by a kinetic barrier. Thus, the 1T phase can be considered kinetically stabilized and remains stable only while there is insufficient thermal energy in the system to overcome the energy barrier to reversion. Under ambient temperature conditions, the energy barrier is sufficient for the appearance of stability for short periods of time, which is one explanation for why fresh 1T TMCs may seem stable during initial electrochemical tests [58,59].

However, several destabilizing factors that do not exist under static storage conditions are created by the electrochemical system. These include mechanical stresses due to lattice strains from the disruption of the octahedral coordination symmetry of the 1T phase by the ion insertion during the charging process. The increased temperature caused by resistive heating during high-rate cycling contributes to the thermal activation energy needed to cross the reversion barrier. Overall, these electrochemical factors facilitate the 1T-2H reversion in ways that cannot be identified by static stability measurements done outside the operating cell [60].

2.6.2 Experimental Evidence for Phase Reversion during Cycling

The phenomenon of phase reversion to the 1T phase upon electrochemical cycling has been confirmed experimentally in various TMC systems and characterization techniques. The transformation of phases has been commonly observed by Raman spectroscopy through phase-specific vibrational signatures determined by the positions and intensities of the E^1_{2g} and A_{1g} bands. In all cases of 1T-MoS_2 studied by the chemical exfoliation method, 2H-phase Raman lines gradually appear after prolonged cycling. An increased temperature and high current density expedite the phase reversion process [53,61].

These findings are additionally corroborated by X-ray photoelectron spectroscopy (XPS), which reveals systematic changes in Mo 3d binding energy toward 2H-characteristic values. This demonstrates that the phase reversion observed by Raman spectroscopy is not a surface-only phenomenon but rather a true bulk structural shift. The formation of 2H-phase domains within initially 1T-dominant microstructures has been directly seen by high-resolution transmission electron microscopy (HR-TEM) analyses of cycled 1T-MoS_2 electrodes. Increased mechanical stress concentration occurs at the boundaries between these stages. Increased local resistance and preferred structural degradation in later cycles are linked to these phase border locations. Establishing a mechanistic connection between the capacity decrease frequently seen in long-term cycling studies of 1T-phase TMC electrodes, phase reversion, and microstructural evolution [53,60,62].

A distinct but equally important type of structural deterioration has been documented in SnS_2-based systems that adopt the 1T coordination geometry as their ground state instead of a metastable polymorph. During deep sodiation, SnS_2 electrodes experience increasing amorphization and tin nanoparticle exsolution rather than phase reversion. This process irrevocably destroys the layered structure and is driven by a conversion reaction mechanism. This discrepancy between conversion-dominated degradation in SnS_2

and intercalation-dominated degradation in MoS_2 highlights the importance of considering the specific degradation mechanism of each TMC chemistry when assessing long-term cycle stability [63,64].

2.6.3 Structural Evolution and Capacity Fade Mechanisms

Beyond phase reversion, a number of parallel processes are involved in the structural evolution of 1T-phase transition metal chalcogenide (TMC) electrodes during prolonged cycling. Fatigue results from mechanical stress caused by volume increases due to ion intercalation and deintercalation within the electrode microstructure. Such fatigue is encouraged by factors such as restacking of nanosheets, exfoliation, and a gradual decrease in accessible surface area. Restacking of the nanosheets is particularly harmful, as it reduces the effective inter-layer spacing of ions resulting from ion diffusion, which hinders the electrochemical benefits associated with the expanded van der Waals gallery of the 1T phase. Chalcogen vacancies may serve as nucleation sites for structural changes. The activation barrier for both phase reversal and amorphization is lowered by the local lattice distortion surrounding these vacancies [65,66].

Electrochemical impedance spectroscopy (EIS) analysis of aged 1T-phase TMC electrodes has consistently shown a progressive increase in charge-transfer resistance (Rct) with increasing cycle number. Parallel Raman and X-ray photoelectron spectroscopy (XPS) investigations show that this rise is correlated with a decrease in the metallic 1T domain percentage. These results suggest that phase reversion, rather than electrolyte breakdown or solid electrolyte interphase (SEI) evolution, which are the main degradation mechanisms in graphite-based anodes, is mechanistically linked to capacity fade and rate performance degradation [65,67].

2.6.4 Strategies for Stabilizing the 1T Phase against Reversion

To prevent thermodynamically induced reversion to the 2H phase during prolonged cycling, a number of techniques have been devised to kinetically stabilize the 1T phase. By sterically impeding the chalcogen plane glide necessary for the 1T to 2H structural transition, covalent functionalization of the TMC surface with organic molecules or polymer coatings has been demonstrated to prevent reversion. By partially filling the d-orbital manifold and decreasing the energy advantage of the 2H configuration, heteroatom doping, especially with electron-donating species like nitrogen or rhenium, stabilizes the 1T phase and hence lowers the thermodynamic driving force for reversion. By mechanically limiting the interlayer geometry and offering continuous conductive pathways that reduce local heating during high-rate cycling, substrate confinement techniques—in which TMC nanosheets are anchored to carbon nanotube networks, graphene scaffolds, or metal-organic framework matrices-simultaneously suppress phase reversion and nanosheet restacking [58,68–71].

Despite these developments, a stabilization technique that works for all TMC chemistries, operating temperatures, and ion storage systems has not yet been shown. Therefore, the development of stabilizing techniques that are efficient, scalable, and compatible with existing electrode manufacturing procedures is essential for the actual deployment of 1T-phase TMC electrodes in commercial energy storage devices. A thorough grasp of the present state and potential future course of two-dimensional chalcogenide research for energy storage applications requires a serious evaluation of this constraint in addition to the proven electrochemical benefits of the 1T phase.

2.6.5 Quantitative Benchmarking of Key Electrochemical and Theoretical Parameters

The Use of qualitative performance comparisons between transition metal chalcogenide (TMC) systems is a major drawback of the review articles that are currently available in this sector. To close this gap,

Table 1 shows quantitative DFT-calculated and experimentally observed parameters for representative electrode systems based on MoS_2, WS_2, and SnS_2. This technology enables direct numerical benchmarking across phase variations, ion storage chemistries, and synthesis techniques. Adsorption energies (Eads), diffusion barriers (Ea), experimentally determined electronic conductivity values, and reported specific capacities under established testing conditions are among the gathered parameters. To enable a direct comparison of 2H and 1T phase performance within the same material system, phase identity is specifically mentioned in the aforementioned studies. Table 1 is intended to be a helpful guide for researchers selecting material compositions and phase engineering targets for certain ion storage applications.

Table 1: Quantitative comparison of DFT-calculated and experimental parameters for representative MoS_2-, WS_2-, and SnS_2-based electrode system.

Material	Phase	Ion System	Eads (eV)	Ea (eV)	Conductivity (S/m)	Specific Capacity (mAh/g)	Ref.
MoS_2	2H	Li^+	−1.20	0.49	~10^{-3}	167 (theoretical)	[72,73]
MoS_2	1T	Li^+	−2.15	0.21	~10^{5}	335 (theoretical)	[72]
MoS_2 (vacancy-engineered)	1T	Li^+	−3.20	0.15	~10^{5}	1290 (experimental)	[74,75]
MoS_2 (expanded interlayer)	2H/1T	Na^+	−1.68	0.28	~10^{3}	854 (experimental)	[61,73,76]
MoS_2	2H	K^+	−0.89	0.56	~10^{-3}	98 (experimental)	[61]
MoS_2	1T	K^+	−1.74	0.31	~10^{5}	245 (experimental)	[53]
WS_2	2H	Li^+	−1.35	0.44	~10^{-2}	174 (theoretical)	[73,77]
WS_2	1T	Li^+	−2.28	0.19	~10^{5}	348 (theoretical)	[77,78]
WS_2	2H	Na^+	−1.52	0.38	~10^{-2}	195 (experimental)	[78,79]
WS_2 (heterostructure)	1T	Na^+	−2.41	0.22	~10^{4}	508 (experimental)	[76,79]
SnS_2	1T	Li^+	−1.94	0.33	~10^{1}	645 (experimental)	[80]
SnS_2	1T	Na^+	−1.71	0.41	~10^{1}	583 (experimental)	[64]
SnS_2 (N-doped)	1T	Na^+	−2.18	0.29	~10^{2}	738 (experimental)	[81]
SnS_2 (carbon composite)	1T	K^+	−1.58	0.35	~10^{2}	426 (experimental)	[82]
MoS_2/graphene hybrid	1T	Na^+	−2.53	0.18	~10^{5}	916 (experimental)	[83]
WS_2/CNT hybrid	1T	K^+	−1.92	0.26	~10^{4}	389 (experimental)	[84–86]

Table 1 shows a number of tendencies that are not apparent from qualitative comparisons alone. First, moving from the 2H to the 1T phase lowers the diffusion barrier (Ea) by around 50 to 60 percent in all three transition metal chalcogenide (TMC) systems and ion chemistries. This result shows that phase change always improves kinetics. Second, the inclusion of vacancies in 1T-MoS_2 significantly reduces the adsorption energy (Eads) and Ea, outperforming the outcomes of phase conversion alone. This is consistent with the mechanistic approach in Section 2.5 and illustrates the combined benefits of engineering both phase and faults. Third, K^+ storage systems exhibit the biggest differences between experimental specific capacities and the theoretical values predicted by density functional theory (DFT). As discussed in Section 2.6, this is caused by partial phase conversion, nanosheet restacking, solid electrolyte interphase (SEI) development, and the instability of the 1T phase during cycling. Fourth, the highest experimental specific capacities in all

ion systems are obtained by hybrid electrodes that mix 1T-phase TMCs with graphene or carbon nanotube scaffolds. This supports the heterointerface engineering techniques discussed later. All things considered, these figures establish a baseline for assessing upcoming materials advancements in this area.

2.7 Theoretical Foundation: The DFT Approach

While DFT gives the mechanical justification for these discoveries, experimental synthesis and characterization provide actual physical confirmation of a material's performance. Before experimental production and testing, DFT serves as a reliable computational framework for predicting electrical characteristics, phase stability, ion transport kinetics, and defect formation energetics in the context of 2D chalcogenide nanomaterials [17]. To speed up the identification of new materials, DFT has advanced beyond standalone computer studies and is now increasingly coupled with machine learning. Kim et al. [28] illustrated this integration by developing a DFT-verified database and machine learning framework for producing high-entropy carbides with enhanced mechanical properties. One obvious use of this method is the rapid screening and optimization of 2D TMCs for electrochemical energy storage applications. Band structure analysis and total energy calculations are only two aspects of the present DFT toolkit for researching 2D chalcogenides. It now includes crystal orbital Hamilton population analysis, charge-density difference analysis, Bader charge partitioning, projected density of states decomposition, and nudged elastic band pathway mapping, each of which offers a unique and complementary window into the atomistic mechanisms controlling ion storage performance.

2.7.1 Introduction to Density Functional Theory in Material Science

All condensed matter systems, whether crystalline, amorphous, molecular, or nanoscale, consist of collections of atoms and electrons bound together by electromagnetic interactions. The complete quantum mechanical description of such a system is contained in the many-body Schrödinger equation:

$$i\hbar\frac{\partial}{\partial t}\Phi(\mathrm{r};\mathrm{t}) = \left(-\sum_{i}^{N}\frac{\hbar^2}{2m_i}\frac{\partial^2}{\partial r_i^2} + \sum_{i<j}^{N}\frac{\mathrm{e}^2 Z_i Z_j}{|r_i - r_j|}\right)\Phi(\mathrm{r};\mathrm{t}) \tag{1}$$

where $\Phi(\mathrm{r};\ t)$ is the many-body wavefunction for N particles, where each particle has its own mass m_i, charge Z_i and position r_i. Despite its apparent compactness, this equation is computationally intractable for systems containing more than a few electrons, owing to the exponential scaling of the wavefunction with particle number [87].

Density Functional Theory (DFT) is a quantum mechanical modeling method used to investigate the electronic structure of many-body systems. Instead of attempting to solve the complex Schrödinger equation for every individual electron, which is computationally impossible for large systems, DFT relies on the Hohenberg-Kohn theorems. These theorems state that all ground-state properties of a system are determined by its electron density n(r) rather than by its individual wavefunctions. For 2D TMCs, researchers solve the Kohn-Sham equations to determine the spatial distribution of electrons. This method makes it possible to calculate the crystal lattice's total energy, which is essential for figuring out whether the 2H or 1T phase is more stable in a given setting [25].

2.7.2 Electronic Density of States and Band Structure Modeling

The Density of States (DOS) is a valuable outcome of DFT calculations for energy storage applications. By mapping the DOS, it is possible to clearly display the electronic energy distribution within a material.

This technique allows for the accurate identification of the bandgap, or the energy range devoid of electronic energy levels. According to DFT simulations, the bandgap shifts from indirect to direct when the material is reduced to a monolayer, which dramatically changes the material's electrochemical and optical properties.

Important details on metallic behavior are also provided by the DOS. According to DFT investigations, the 1T phase possesses a sizable density of states at the Fermi level (EF), a crucial indicator of metallic conductivity. According to recent research, doping TMCs with early transition metals like vanadium can induce metallic-like characteristics and improve charge-transfer performance by shifting the Fermi level into the conduction band [31].

2.7.3 Projected Density of States and Orbital-Resolved Electronic Structure

The projected density of states (pDOS) reveals which particular atoms and orbitals dominate the electronic states at and near the Fermi level by breaking down the total electronic contribution into individual atomic and orbital components, whereas the total DOS gives an overall picture of electronic structure. Because it pinpoints the exact electronic states involved in charge transfer during ion adsorption and intercalation, this orbital resolution is essential for understanding ion-storage mechanisms in 2D chalcogenides.

Mo d-orbitals, particularly the dz^2 orbital in the valence band maxima, dominate the states close to the Fermi level in the 2H phase of MoS_2, according to pDOS analysis, with a minor contribution from sulfur p-orbitals at the band margins. The Mo d-orbital character is dramatically redistributed in the pDOS upon transition to the 1T phase, with the previously divided dz^2 $dxy/dx^2 - y^2$ and dxz/dyz manifolds collapsing into overlapping contributions at the Fermi level. Changes in conductivity and charge-transfer resistance that have been measured experimentally can be directly linked to this orbital collapse, which is the electronic fingerprint of the 2H to 1T transition.

Furthermore, pDOS analysis of vacancy-containing supercells reveals the emergence of localized mid-gap states with mixed Mo d and S p character, providing atomistic confirmation that chalcogen vacancies introduce electronic states that enhance ion adsorption and modify charge-transfer kinetics as discussed in Section 2.5. The degree of orbital hybridization between the alkali metal s-orbitals and the TMC d and p states is revealed by pDOS calculations of TMC surfaces with adsorbed Li^+, Na^+, or K^+ ions for ion-specific storage studies. This directly quantifies the strength and nature of the ion-surface chemical interaction [88–91].

2.7.4 Charge-Density Difference Maps and Electron Transfer Visualization

Charge-density difference (CDD) maps, which provide real-space information about where electrons accumulate and deplete within the crystal, provide a spatially resolved visualization of electron redistribution upon ion adsorption or phase transition, in addition to the energy-integrated view of the DOS and pDOS. CDD maps are produced by subtracting the electron densities of the distinct subsystems (the TMC surface and the adsorbed ion separately) from the electron density of the combined adsorbed system:

$$\Delta\rho(r) = \rho(\text{TMC} + \text{ion}) - \rho(\text{TMC}) - \rho(\text{ion}) \quad (2)$$

Positive $\Delta\rho(r)$ regions suggest electron accretion, while negative $\Delta\rho(r)$ regions indicate electron depletion. Strong electron accumulation between the adsorbed ion and the nearest chalcogen atoms is routinely shown in CDD maps for alkali metal ion adsorption on MoS_2, with comparable electron depletion surrounding the alkali metal center. This demonstrates that ion adsorption is more than merely electrostatic

contact; it also entails significant charge transfer from the TMC surface to the adsorbed ion. This charge-transfer property directly affects the magnitude of the local work function change at the electrode-electrolyte interface, the strength of ion binding, and the reversibility of adsorption during cycling.

CDD maps made between the 2H and 1T phases of MoS_2 are used to visualize the spatial redistribution of electron density associated with the chalcogen plane glide for phase transition research. Consistent with the loss of crystal field stabilization energy that propels the metallic behavior of the 1T configuration, these maps show how electron density shifts from metal-chalcogen bonding regions in the 2H phase to non-bonding regions in the 1T phase. By localizing the electronic perturbation caused by chalcogen vacancies to within approximately two unit cells of the defect site, CDD maps determine the spatial range over which vacancy-induced electronic restructuring influences ion adsorption and charge-transfer kinetics in defect-containing systems [92,93].

2.7.5 Bader Charge Analysis and Quantitative Charge Transfer

Bader charge analysis offers a rigorous mathematical framework for dividing the total electron density of a system into contributions linked to individual atoms, whereas CDD maps offer qualitative spatial representation of charge redistribution. This method, developed by Bader and colleagues, uses zero-flux surfaces in the electron density, where all electron density is attributed to the enclosing atom, to determine atomic volumes. A quantitative indicator of ionic character and charge transfer magnitude, the Bader charge for each atom is then calculated as the difference between its nuclear charge and its assigned electron population.

Bader analysis measures the exact amount of charge transferred from the TMC electrode to adsorbed alkali metal ions in the context of 2D chalcogenide ion storage. Bader analysis usually assigns 0.85 to 0.90 electrons to the deposited lithium core for Li^+ adsorption on virgin 2H-MoS_2, showing near-complete ionization and strong electrostatic interaction. The transferred charge for Na^+ adsorption under similar conditions is usually lower, ranging from 0.78 to 0.84 electrons [94,95]. This is in line with the greater diffusion barriers and poorer adsorption energies for sodium compared to lithium shown in DFT-NEB experiments. According to Bader analysis, chalcogen vacancy production redistributes electron density from the vacancy site to nearby metal atoms, increasing their effective negative charge and strengthening their electrostatic attraction for positively charged alkali metal ions. This quantitative charge redistribution, which links the defect engineering techniques covered in Section 2.5 to an accurately measured electronic driving force, causes the experimentally observed increase in ion adsorption capacity at vacancy sites. Bader analysis provides a quantitative electronic basis for the enhanced ion adsorption and charge-transfer kinetics of the metallic phase in phase transition studies by confirming that Mo atoms in the 1T phase carry a systematically higher effective negative charge than their 2H counterparts due to the different orbital occupancies associated with octahedral versus trigonal prismatic coordination [91,96,97].

2.7.6 Crystal Orbital Hamilton Population Analysis

Direct evaluation of the bonding or antibonding nature of electronic states as a function of energy is made possible by crystal orbital Hamilton population (COHP) analysis, which offers a bond-resolved breakdown of the overall band structure energy into contributions from individual atom pairs. COHP analysis provides an orbital-level interpretation of structural stability, phase preference, and bond evolution during ion intercalation by identifying which occupied electronic states stabilize and which destabilize particular chemical bonds, in contrast to the DOS, which counts states regardless of their bonding role.

According to COHP analysis of the metal-chalcogen bond [98], the occupied electronic states close to the valence band maximum in the 2H phase of 2D TMC systems are mostly bonding in character, which contributes to the thermodynamic stability of the trigonal prismatic coordination. The structural lability of the 1T phase and its thermodynamic metastability relative to the 2H configuration are directly caused by the transition to the 1T phase, which introduces partial occupation of metal-chalcogen antibonding states near the Fermi level, lowering the net bonding strength of the metal-chalcogen interaction [99]. This COHP-derived understanding links macroscopic phase stability behavior to the bonding type of certain electronic states, offering a rigorous quantum mechanical justification for the experimental finding of 1T phase reversal covered in Section 2.6.

In order to determine whether ion adsorption strengthens or weakens the host lattice metal-chalcogen interactions, COHP analysis of the ion-TMC interaction quantifies the bonding contribution of the hybridized alkali metal and TMC orbitals revealed by pDOS analysis [100]. Lithium insertion partially populates Mo-S antibonding states, gradually reducing the intralayer covalent bonding with increasing lithiation depth, according to studies on Li intercalation in MoS_2. The prediction of this bond weakening by COHP analysis before experimental testing demonstrates the predictive and preventive value of this computational approach in directing electrode design toward operating voltage windows that avoid irreversible structural degradation. This bond weakening is the atomistic precursor to the structural amorphization and conversion reactions observed experimentally at deep discharge states.

2.7.7 Nudged Elastic Band Calculations for Ion Diffusion Pathways

The classic DFT-based method for mapping the minimal energy pathway (MEP) for ion migration between neighboring stable adsorption sites inside the TMC lattice is the nudged elastic band (NEB) method. To prevent image collapse onto either endpoint, the NEB approach builds a chain of intermediate atomic configurations (images) connecting the initial and final states of the diffusion event. All of the images along the chain are concurrently relaxed under a spring force constraint. The energy maximum along the relaxed chain defines the transition state, and the energy difference between this maximum and the initial adsorption minimum defines the diffusion barrier Ea [43].

Two distinct migration paths for in-plane diffusion within a single TMC layer are shown by NEB simulations for MoS_2: a direct hopping track between adjacent hollow sites above the hexagonal Mo lattice and an indirect approach via bridge sites between surrounding S atoms. The indirect pathway consistently displays a lower Ea in DFT-NEB calculations, indicating that the favored mode of ion migration in MoS_2 is bridge-site hopping rather than direct hollow-to-hollow transit. Strategically positioning sulfur vacancies along the favored migration pathway can lower Ea by eliminating the electrostatic repulsion that takes place at bridge-site transition states because bridge sites are located adjacent to the Mo-S bonds that are most prone to vacancy formation. Defect engineering can benefit from this route selectivity.

Particularly for Na^+ and K^+, whose ionic radii approach or surpass the native interlayer gap, NEB calculations reveal much larger Ea values for interlayer diffusion compared to in-plane migration. For thick electrode films, interlayer diffusion is the rate-limiting step because it regulates ion transport between neighboring TMC layers. Interlayer NEB simulations on expanded-spacing MoS_2 structures show that increasing the interlayer distance from 0.62 nm to around 0.90 nm reduces the interlayer Na^+ diffusion barrier by up to 40%. This gives the interlayer expansion options discussed in Section 2.5 quantitative atomistic support. The NEB calculations on 1T-phase MoS_2 consistently produce lower Ea values than comparable estimates on the 2H phase for all three alkali metal ions. This demonstrates that the electronic structural change associated with the phase transition directly increases ion diffusion kinetics rather than

only improving electronic conductivity and establishes a twofold kinetic benefit of phase engineering that is only fully exposed through NEB analysis [45].

2.7.8 Adsorption Energies and Their Role in Ion Storage Capacity

The ion adsorption energy (Eads) calculated by DFT quantifies the thermodynamic driving force for ion binding at a specific surface or subsurface site and is defined as:

$$\text{Eads} = \text{E(TMC + ion)} - \text{E(TMC)} - \text{E(ion)} \quad (3)$$

where stronger and thermodynamically more favorable ion binding is indicated by a higher negative Eads. The electrode's theoretical storage capacity is directly correlated with this number: sites with sufficiently negative Eads values facilitate reversible ion storage, sites with insufficiently negative values do not retain ions during discharge, and sites with excessively negative values may trap ions irreversibly, reducing Coulombic efficiency [26,42,101].

DFT calculations of Eads over the MoS_2 surface at various lithiation levels show a consistent impact of adsorption strength on surface coverage. Electrostatic repulsion between co-adsorbed ions causes Eads to become less negative as ion coverage rises. By defining a theoretical maximum storage capacity beyond which further ion adsorption becomes thermodynamically unfavorable, this coverage-dependent behavior offers a DFT-derived upper bound for experimental capacity optimization. Chalcogen vacancy sites consistently exhibit greater negative Eads values than pristine basal plane sites in all alkali metal ions and TMC systems studied; the augmentation is highest for K^+ because potassium adsorption is more sensitive to the local electrostatic environment than lithium. It is clear from systematic DFT Eads mapping [42,102,103] that vacancy engineering is a more successful performance enhancement method for K-ion storage than for Li-ion storage. This conclusion would not be apparent from experimental capacity measurements alone. Practical design implications result from this ion-specific vacancy sensitivity.

2.7.9 Integrating the DFT Toolbox: From Atomistic Insight to Electrode Design

Combining the computational methods described in Sections 2.7.2–2.7.8 is more efficient than using them separately. A thorough DFT characterization of a 2D chalcogenide electrode material for ion storage applications incorporates total energy calculations for phase stability assessment, pDOS and COHP analysis for electronic structure and bonding characterization, CDD maps and Bader analysis for charge transfer quantification, Eads mapping for storage capacity prediction, and NEB calculations for diffusion kinetics evaluation. Together, these tools provide an atomistic description of how phase identity, defect concentration, lattice strain, and composition all contribute to self-consistent and mutually validating electrochemical performance [103,104].

DFT′s function in 2D chalcogenide research has changed as a result of this integrated computational framework. It is now a predictive design platform that directs synthesis choices before experiments, rather than a supporting tool that verifies experimental results after the fact. Researchers can find the best material configurations computationally and focus experimental synthesis efforts on the most promising candidates by creating DFT-derived phase stability maps, adsorption energy landscapes, and diffusion barrier profiles as functions of composition and defect concentration. This greatly speeds up the development cycle from conceptual framework to functional electrode. Future experimental and computational developments in 2D chalcogenide energy storage research can be systematically assessed using the quantitative benchmarks created by this toolbox, which are listed in Table 1 of Section 2.6.5 [104,105].

2.7.10 DFT as a Synthesis Optimization Tool

From being a post-synthesis characterization tool, DFT has developed into a potent prediction framework that is used throughout the actual synthesis planning phase. DFT calculations now allow researchers to anticipate phase stability under certain processing conditions, find energetically advantageous reaction paths, and optimize synthesis parameters before investing experimental resources, instead of validating experimental results after the fact. To be more precise, DFT is used to simulate surface diffusion and nucleation processes on particular substrates, determine the lowest-energy synthesis pathways toward a target phase, and compute the decomposition energies of precursor molecules. DFT can thereby forecast the ideal growth temperatures and pressures for the intended 2H or 1T phase; and assess the thermodynamic stability and formation energy of the metastable 1T phase as a function of dopant concentration and identity, directing the choice of stabilizing agents compatible with scalable fabrication processes [25,106].

The predictive power of DFT-guided synthesis optimization is well illustrated by the work of Hojaji et al. [26], who explored 1T-MoS_2 as a cathode host for lithium-sulfur batteries by examining the adsorption affinity of pristine and defect-engineered 1T-MoS_2 substrates toward lithium polysulfides (LiPSs). A major performance limitation of lithium-sulfur batteries is the polysulfide shuttle effect, arising from the rapid migration of dissolved LiPS intermediates to the anode and the sluggish conversion kinetics of the LiPS reaction chain. Using DFT, Hojaji et al. calculated the adsorption energies of LiPS species on pristine 1T-MoS_2 and on 1T-MoS_2 surfaces containing one and two sulfur vacancies, mapped the Gibbs free energy profiles for the full LiPS conversion chain, and identified the preferred migration pathways and activation energies for the rate-limiting Li_2S_4 to Li_2S conversion step. A clear example of computation-first synthesis design in the 2D chalcogenide area was established by the experimental validation of the optimized 1T-MoS_2 structures found computationally (Fig. 4), which showed better Li-S battery performance commensurate with the DFT predictions.

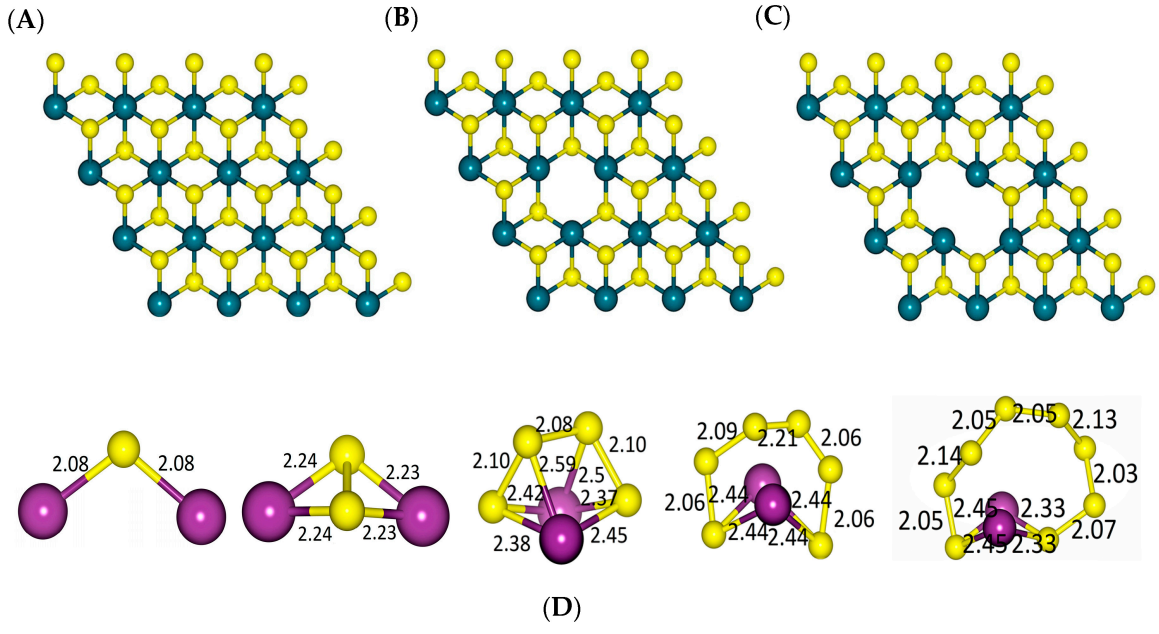

Figure 4: The optimized structures of (**A**) 1T-MoS_2, (**B**) 1T-MoS_2-1S, and (**C**) 1TMoS_2-2S and (**D**) Li2Sn (n = 1, 2, 4, 6, and 8), where teal, violet, and yellow colours denote Mo, Li, and S atoms, respectively. Atom bond lengths are in Å. Reproduced from [26] under a Creative Commons Attribution (CC BY 4.0) license.

Li-S systems are not the only ones that can benefit from this DFT-guided synthesis optimization method. The same computational methodology has been used to screen heterostructure combinations for suppressed nanosheet restacking, determine dopant concentrations that stabilize the 1T phase against thermal reversion, and predict ideal CVD growth temperatures for phase-selective MoS_2 deposition. By combining DFT synthesis optimization with the advanced characterization toolbox described in Sections 2.7.2–2.7.9, researchers can create a closed computational-experimental loop in which DFT predictions guide synthesis, characterization validates the predicted structures, and differences between prediction and experiment inform improved DFT models, gradually converging on materials with optimized electrochemical performance.

2.8 Comparative Analysis of Sulfide and Selenide 2D Chalcogenides: From MoS_2 to WSe_2, SnS_2, and $ReSe_2$

While MoS_2 has been the standard 2D transition metal chalcogenide for electrochemical energy storage research, a comprehensive assessment of the field requires a methodical comparison with other chalcogenide systems like SnS_2, WSe_2, and $ReSe_2$. The substitution of selenium for sulfur as the chalcogen atom fundamentally changes the orbital hybridization, electrical conductivity, ion polarizability, redox kinetics, and structural stability of the MX_2 lattice. Understanding how chalcogen identity regulates these properties is necessary to select the optimal TMC chemistry for specific ion storage applications [5].

2.8.1 How Chalcogen Identity Controls Orbital Hybridization and Electronic Conductivity

The shift from sulfide to selenide chalcogenides introduces a heavier and more polarizable chalcogen atom with a larger atomic radius (1.84 Å for Se versus 1.04 Å for S), a higher primary quantum number, and more diffuse valence orbitals. Taken together, these differences alter the metal-chalcogen bond in three mechanistically important ways. First, compared to the analogous sulfide, stronger covalent metal-chalcogen bonding is produced by the greater orbital overlap between the more diffuse Se 4p orbitals and the metal d-orbitals, which narrows the bandgap and changes the electronic structure toward metallic behavior. This explains why selenide-based TMCs often have higher intrinsic electrical conductivity than their sulfide counterparts and why WSe_2 has a smaller bandgap of about 1.2 eV in the monolayer limit compared to 1.8 eV for WS_2. Second, the 1T phase is thermodynamically closer to the 2H phase in selenide systems and can be accessible under milder synthesis conditions due to the reduced crystal field splitting energy in selenides compared to sulfides, which lowers the energetic cost for the 2H to 1T transition. Third, the dielectric screening of Coulombic interactions within the TMC layer is improved by the greater polarizability of the Se anion, which lowers the effective electron-electron repulsion and further stabilizes metallic behavior in the 1T configuration [57,107–109].

2.8.2 SnS_2: Intercalation and Conversion Mechanisms

In contrast to MoS_2, where the 1T phase must be induced by external intervention, SnS_2 adopts the CdI_2 crystal structure with tin atoms octahedrally coordinated by six sulfur atoms in a 1T configuration that represents the thermodynamic ground state rather than a metastable polymorph. Because of its native 1T coordination, SnS_2 has intrinsic metallic-like electronic conductivity without requiring phase engineering, which makes it a desirable electrode material for ion storage applications where ease of production is crucial. Interlayer expansion techniques similar to those used for MoS_2 are motivated by the mild limits on Na^+ and K^+ intercalation kinetics imposed by the approximately 5.9 Å interlayer spacing of SnS_2, which is slightly lower than that of MoS_2 [110–112].

Unlike the primarily intercalation-based mechanism of MoS_2, the electrochemical storage mechanism of SnS_2 comprises a dual-stage procedure. The Sn-S bonds are broken, and SnS_2 is reduced to metallic tin nanoparticles embedded in a Li_2S or Na_2S matrix during the initial lithiation or sodiation. Following this conversion, the tin nanoparticles undergo an alloying reaction with either sodium or lithium, resulting in the formation of Li-Sn or NaSn alloy phases. When conversion and alloying contributions are taken into consideration, SnS_2's potential capacity for lithium storage is roughly 1232 mAh/g, which is significantly greater than MoS_2's theoretical capacity for intercalation alone. However, the main problem for SnS_2-based anode materials is electrode pulverization and capacity decline over prolonged cycling due to the significant volume expansion associated with the alloying reaction, which can reach up to 300% for full lithiation [28,38]. By offering mechanical confinement and lowering the absolute volumetric change per particle, carbon matrix encapsulation and smaller nanosheet dimensions have been shown to partially mitigate this volume expansion. This has resulted in experimentally measured capacities of 583 to 738 mAh/g for Na^+ storage in optimized SnS_2 architectures, as compiled in Table 2 [80,113–116].

2.8.3 WSe_2: Enhanced Conductivity and Selenide Advantages

The selenide analog of WS_2, WSe_2, has the identical trigonal prismatic 2H ground state coordination. However, because of the chalcogen identity effects discussed in Section 2.8.1, its electrical and electrochemical properties are very different from those of its sulfide counterpart. Compared with WS_2, WSe_2's narrower bandgap lowers charge-transfer resistance at the electrode-electrolyte interface and increases the pseudocapacitive contribution to total charge storage, resulting in better rate capability under comparable cycling conditions. DFT calculations show that Li^+ adsorbs on the pristine basal plane of WSe_2 with energies typically in the range of −1.2 to −1.5 eV, and adsorption is substantially strengthened at selenium vacancy sites [117], representing stronger adsorption than the equivalent sulfide values for WS_2 due to the enhanced polarizability of the Se anion and the stronger orbital hybridization between Li s-orbitals and Se 4p states.

The interlayer spacing of WSe_2 in its native 2H phase is approximately 6.5 Å, slightly larger than MoS_2 and WS_2, which provides marginally improved accommodation of Na^+ and K^+ ions during intercalation and reduces the diffusion barrier for large ion transport [118–120].

In heterostructure configurations combining 1T-WSe_2 with carbon nanotube scaffolds, experimentally measured specific capacities of 508 mAh/g for Na^+ storage have been reported alongside charge-transfer resistance values of less than 50 Ω, demonstrating that the combination of selenide-enhanced conductivity and heterostructure architecture delivers electrochemical performance exceeding that of equivalent WS_2-based systems [5,121]. The DFT-predicted conductivity enhancement is experimentally validated by recent work by Ismail et al. on tungsten-based chalcogenides, which shows that the selenide substitution consistently provides 15 to 25% improvements in rate capability relative to the sulfide analog at high current densities [122–124].

2.8.4 $ReSe_2$: Anisotropic Structure and Unique Ion Transport Properties

Because of its deformed 1T crystal structure, where rhenium atoms form diamond-shaped Re_4 clusters within each layer instead of the regular hexagonal arrangement typical of MoS_2 and WSe_2, $ReSe_2$ has a unique place among 2D chalcogenides. This structural distortion breaks the MX_2 lattice's in-plane isotropy, resulting in a highly anisotropic electronic structure with direction-dependent ion transport and electrical conductivity. In order to improve rate performance beyond what isotropic TMC electrodes can accomplish, orientated electrode manufacturing can take advantage of the preferred ion diffusion paths created by the significantly higher in-plane conductivity of $ReSe_2$ along the Re_4 chain direction than perpendicular to it.

$ReSe_2$'s distorted 1T structure also provides remarkable interlayer decoupling: its weak and anisotropic interlayer interactions result in an interlayer spacing of about 6.7 Å with a much lower interlayer binding energy than MoS_2 or WSe_2, allowing for stable cycling performance without the interlayer expansion engineering strategies needed for Na^+ and K^+ storage in tightly coupled TMC systems [125,126]. $ReSe_2$ is a high-rate SIB anode material whose kinetic advantages come from structural anisotropy rather than phase engineering or interlayer expansion [126,127]. DFT calculations of the Na^+ diffusion barrier in $ReSe_2$ yield values of roughly 0.18 to 0.24 eV along the Re_4 chain direction, which is significantly lower than the 0.62 eV barrier in 2H-MoS_2 and even competitive with values achieved in engineered expanded-spacing MoS_2 structures.

2.8.5 Quantitative Comparison of Sulfide and Selenide Systems

Key electrical and electrochemical parameters for representative sulfide and selenide TMC systems are compiled in Table 2, allowing for a direct quantitative comparison of how chalcogen identity affects performance throughout the property space pertinent to ion storage applications.

Table 2: Comparative electronic and electrochemical parameters for sulfide and selenide 2D chalcogenide electrode systems.

Material	Structure	Bandgap (eV)	Interlayer Spacing (Å)	Eads Li^+ (eV)	Diffusion Barrier Na^+ (eV)	Experimental Capacity (mAh/g)	Ion System	Ref.
MoS_2 (2H)	Trigonal prismatic	1.8 (ML)	6.2	−1.20	0.62	167 (theoretical)	Li^+	[26,128]
MoS_2 (expanded interlayer) 2H/1T	Octahedral	Metallic	6.2	−2.15	0.28	854	Na^+	[32,76,128]
WS_2 (2H)	Trigonal prismatic	2.0 (ML)	6.2	−1.35	0.44	174 (theoretical)	Li^+	[88,124]
WS_2 (heterostructure) 1T	Octahedral	Metallic	6.2	−2.28	0.22	508	Na^+	[79,129]
SnS_2 (1T)	Octahedral (native)	2.2 (bulk)	5.9	−1.94	0.41	583 to 738	Na^+	[79,120]
WSe_2 (2H)	Trigonal prismatic	1.2 (ML)	6.5	−1.52	0.38	195	Na^+	[79,123]
WSe_2/CNT (1T)	Octahedral	Metallic	6.5	−2.41	0.22	508	Na^+	[79,126]
$ReSe_2$ (distorted 1T)	Distorted octahedral	1.3 (bulk)	6.7	−1.78	0.18 to 0.24	420 to 560	Na^+	[130]
VS_2 (1T)	Octahedral (native)	Metallic	5.8	−2.05	0.19	466	Na^+	[120,131]

ML = monolayer; Eads = adsorption energy; diffusion barrier and Eads values from DFT calculations; experimental capacities from cited references.

3 Synthesis Methods for 2D Chalcogenides

The synthesis of 2D chalcogenide nanomaterials is the most critical step in determining the final material's phase (2H or 1T), defect density, layer thickness, and overall electrochemical performance. The choice of synthesis technique has a major impact on the material's scalability, cost-effectiveness, and environmental friendliness in addition to its structural quality and phase purity as 2D chalcogenide research advances from fundamental laboratory examination to practical device application. You et al. [132] outlined four typical pathways for the synthesis of TMD materials. A closer look at these pathways shows that

synthesis techniques can be broadly classified into two categories: top-down and bottom-up methods. Each of these approaches has specific trade-offs in terms of cost, environmental impact, throughput, and structural quality that must be carefully balanced against the requirements of the intended application [133].

The benefits of top-down approaches include low capital costs, simple equipment needs, and interoperability with large-scale manufacturing facilities. They start with bulk layered crystals and transform them into monolayer or few-layer sheets. Mechanical exfoliation, liquid-phase exfoliation (using shear force or ultrasonication), and electrochemical exfoliation are examples of top-down techniques. Among these, liquid-phase exfoliation has shown that large-scale production is feasible [134,135]. Even though these techniques typically maintain high crystalline quality, they frequently have low yield and little control over phase purity; defect concentration and the polydisperse nanosheet dimensions created by mechanical exfoliation processes reduce batch-to-batch reproducibility in a way that is challenging to overcome without downstream size-selection processing, which raises costs and decreases yield [106,136,137].

By building the 2D structure atom by atom from molecular precursors, bottom-up techniques, on the other hand, offer greater control over phase composition, defect engineering, and layer number uniformity. But compared to top-down approaches, they have a much higher capital cost and a lower throughput. Bottom-up synthesis techniques include colloidal synthesis, chemical vapor deposition (CVD), hydrothermal/solvothermal synthesis, and atomic layer deposition (ALD). Because these synthesis techniques offer more control over morphology, phase composition, and intentional fault introduction, they are more appropriate for scalable manufacture and tailored electrochemical properties [138]. For instance, because CVD necessitates specialized reactor systems, high-purity precursor gases, elevated processing temperatures, and stringent control of growth parameters, it has substantially higher capital and operating costs than liquid-phase exfoliation even though it can produce high-quality, wafer-scale films. Hydrothermal and solvothermal methods, in contrast to CVD, provide greater scalability and lower equipment costs while maintaining a respectable level of control over crystal form and composition. Their batch-processing nature limits continuous manufacturing, and their use of aqueous or organic solvents necessitates solvent recovery, wastewater treatment, and energy-intensive drying and annealing. These factors must therefore be considered in life-cycle and techno-economic assessments [139].

For both tactics to be optimized, DFT is necessary. It is frequently used in growth mechanism modeling, defect formation simulation, phase stability prediction, and formation energy estimates. This computational guidance significantly reduces experimental trial-and-error, focuses research goals, and lowers research costs by helping researchers select the optimal synthesis parameters, such as temperature, pressure, and precursors, to favor the desired metallic 1T phase or controlled defect density [121]. Advances in these areas have shown that integrating DFT-guided predictions with bottom-up synthesis routes provides the most effective pathway for producing high-performance 2D chalcogenides with tunable electronic and electrochemical properties for energy storage applications [33,140,141].

3.1 Top-down Synthesis: Exfoliation Methods

By overcoming the weak van der Waals interactions between adjacent layers, bulk layered crystals can be mechanically or chemically separated into few-layer or monolayer 2D sheets using top-down production techniques. These methods are typically straightforward, economical, and appropriate for large-scale manufacturing. The most popular method among them is Liquid Phase Exfoliation (LPE). To delaminate the layers in LPE, bulk powders are dissolved in suitable solvents and exposed to high shear mixing or ultrasonication. To increase dispersion stability and reduce restacking of exfoliated flakes, recent efforts have concentrated on using eco-friendly green solvents and surfactants [25,30]. Cyrene, a bio-based green

solvent made from cellulose, was shown by Fernandes et al. [142] to perform exceptionally well as a liquid-phase exfoliation medium for 2D materials, providing a less toxic and sustainable substitute for traditional toxic solvents like NMP and DMF. Similar to this, Akeredolu et al. [2] created 2D MoS_2 and graphene nanosheets from bulk materials using a modified LPE approach (see Fig. 5). Vertical heterojunctions were made possible by the sequential deposition or hybridization of these nanosheets to create MoS_2/graphene heterostructures. Compared with devices based on individual materials or conventional LPE-derived films, the photodetector device built using the resulting heterostructures demonstrated improved optoelectronic performance (see Fig. 6).

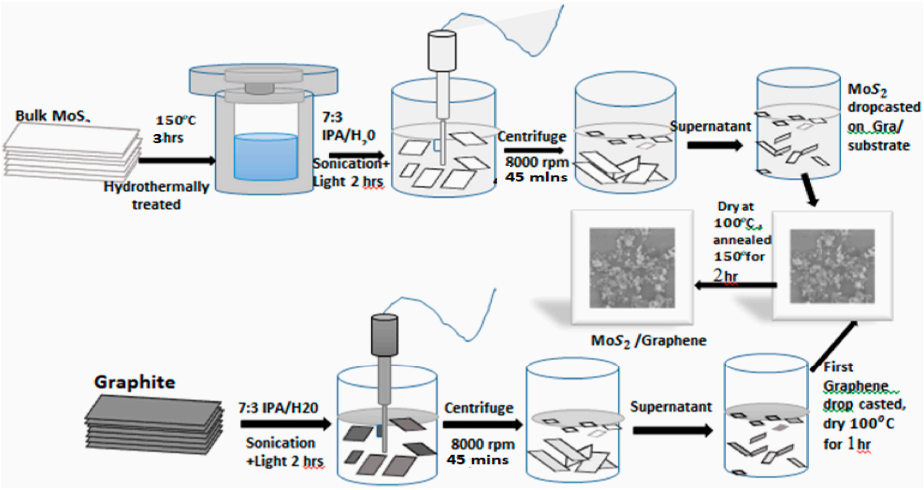

Figure 5: Schematic method of preparation of MoS_2/graphene heterostructure Reproduce from [2] under a Creative Commons Attribution (CC BY 4.0) license.

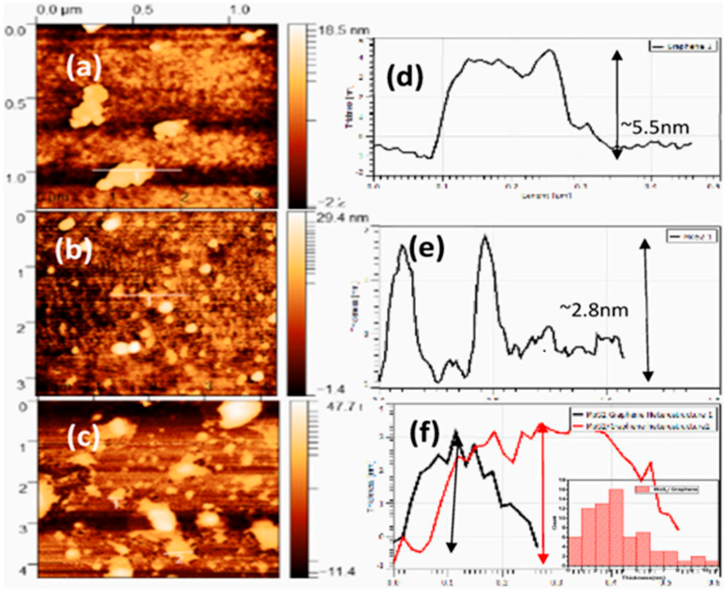

Figure 6: AFM images of (**a**) graphene nanosheets, (**b**) MoS_2 nanosheets, and (**c**) MoS_2/graphene heterostructure, while (**d**–**f**) represent the corresponding thickness distributions of particles in the AFM images, respectively. Scale bars are indicated in the original figure reproduce from [2] under a Creative Commons Attribution (CC BY 4.0) license.

Ion intercalation, which involves inserting tiny ions like Li^+ into the van der Waals galleries of layered crystals, is another potent top-down technique. This insertion makes exfoliation easier by increasing interlayer separation and reducing interlayer interactions. In addition to encouraging layer separation, chemically driven intercalation with organolithium reagents causes a structural phase transition from the thermodynamically stable semiconducting 2H phase to the metallic 1T phase, which dramatically increases electronic conductivity [17,143]. Within the framework of the top-down synthesis technique, ion intercalation is a relatively new phenomenon. This is demonstrated by the work described in [31], which produced thin, superior 2H phase MoS_2 nanosheets from bulk MoS_2 using a cathodic electrochemical exfoliation technique. Large organic trimethylalkylammonium cations were used as intercalants in this method. The resultant nanosheets retained the semiconducting 2H phase while displaying characteristics appropriate for lithium-ion battery anodes. Significantly, these nanosheets outperformed materials made using traditional liquid-phase exfoliation techniques (Fig. 7).

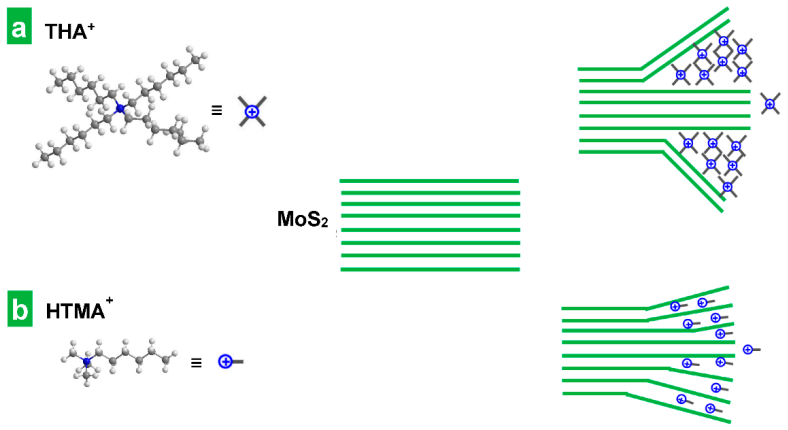

Figure 7: Schematic of the intercalation and exfoliation of layered MoS_2 by tetraalkylammonium and alkyltrimethylammonium cations. Intercalation and exfoliation of MoS_2 with (**a**) larger cross-section tetraalkylammonium cations, and (**b**) alkyltrimethylammonium cations, with a smaller cross-section in the direction of the long alkyl chain. Reproduced from [31] under a Creative Commons Attribution (CC BY 4.0) license.

For mineral rich resource countries like Nigeria, top-down methods such as LPE hold special promise, as they can potentially utilize locally sourced mineral precursors (e.g., lithium-bearing ores or natural molybdenite) for domestic production of 2D nanosheets [1]. See Fig. 8 for a comparison between the two methods.

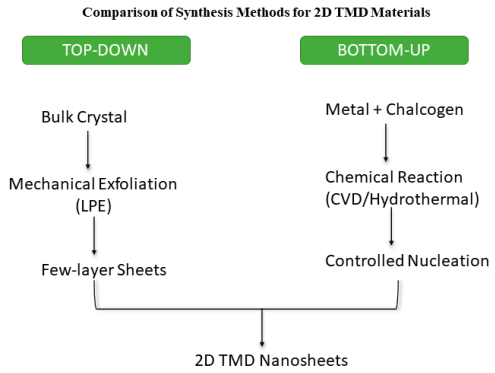

Figure 8: Schematic comparison of top-down (exfoliation from bulk crystals) and bottom-up (growth from precursors) synthesis approaches for 2D chalcogenide nanomaterials. Adapted from [32,106].

3.2 Bottom-up Synthesis: Chemical Vapor Deposition (CVD) and Related Methods

Bottom-up approaches construct 2D chalcogenide layers atom-by-atom from vapor or solution precursors, in contrast to Top-Down approaches. Among these, chemical vapor deposition (CVD) is the most widely used technique for producing high-quality, large-area 2D films. Molybdenum trioxide (MoO_3) and sulfur powder are evaporated and interact on a heated substrate in a conventional MoS_2 CVD method [144–146].

CVD provides excellent structural control, enabling precise customization of layer number, domain size, grain boundaries, and defect density by altering precursor ratios, temperature profiles, and carrier gas flow rates [18,32]. Researchers may deliberately add chalcogen vacancies or change cooling rates to produce defect structures that function as active sites for ion adsorption and diffusion, which is crucial for high-power energy storage applications. For particular device layouts, other bottom-up techniques like hydrothermal/solvothermal synthesis and atomic layer deposition (ALD) provide extra benefits in terms of cost, uniformity, and substrate compatibility.

The efficiency of CVD for the production of nanosheets has been shown in numerous studies. For instance, Tummala et al. [147] used atmospheric pressure chemical vapor deposition (AP CVD) to create MoS_2 nanosheets. Amorphous SiO_2 (50 nm)/Si (100) substrates were utilized for initial development, whereas sulfur powder (S, 99.98%, Sigma Aldrich) and molybdenum trioxide (MoO_3, 99.97%, Sigma Aldrich) were used as precursor sources. Later, pre-patterned SiO_2 and tantalum nitride (TaN) substrates were included in the optimized growth formula. The upstream sulfur and downstream MoO_3 boats were properly positioned in a two-zone furnace with a 2-inch quartz tube (150 cm long) for their AP CVD experiments (see Fig. 9). This work demonstrated a controllable and scalable route for synthesizing large-area MoS_2 ranging from monolayers to few-layer structures.

Similarly, Seravalli et al. [146] reviewed the use of CVD for synthesizing 2D MoS_2 flakes. Owing to the simplicity of the CVD setup (see Fig. 10), precursor delivery typically involves sulfur alone or a combination of sulfur and molybdenum compounds in gaseous form. These precursors are transported to a heated substrate placed on a graphite or similar susceptor, where the chemical reactions required for MoS_2 deposition occur. By altering precursor chemistry and reactor setups, a number of researchers have effectively modified CVD techniques to grow other TMDs, including WS_2, building on these developments in MoS_2 synthesis.

Xu et al. [148] proposed an alternative sealed-tube CVD approach for the creation of monolayer WS_2 by using a homogeneous blend of WS_2 powder and sodium thiosulfate ($Na_2S_2O_3$) as precursor materials, as opposed to the conventional WO_3/sulfur precursor system. The precursor mixture was placed in a quartz boat beneath a face-down SiO_2/Si substrate, and crystal formation was conducted in an Ar/H_2 (5% H_2) environment at 500 and 700°C. Their results demonstrated that growth temperature significantly affected crystal shape, with triangular monolayer domains formed at 500°C and leaf-like WS_2 films forming at 700°C. The study shows how nucleation and growth kinetics may be successfully altered by temperature control and precursor engineering, enabling morphology-controlled synthesis. Furthermore, the relatively low growth temperatures employed in contrast to conventional CVD techniques suggest a potentially more energy-efficient approach for WS_2 synthesis. However, the sealed-tube configuration inherently provides limited control over precursor flux and vapor mobility, which may restrict scalability for continuous wafer-scale manufacture and reduce process repeatability.

In contrast, Thangaraja et al. [149] employed a more conventional atmospheric-pressure CVD (AP-CVD) technique based on sulfurizing WO_3 powder in a two-zone quartz tube reactor utilizing sulfur vapor. By spatially separating the tungsten precursor from the sulfur supply, the authors were able to independently manage precursor evaporation and sulfurization. This made it possible to systematically investigate how

growth temperature and precursor loading affect the production of WS_2 crystals. Their results showed that these variables significantly affected layer thickness, crystal shape, and nucleation density. Growth at 750°C was the primary source of triangular and star-shaped WS_2 crystals, while higher temperatures promoted further crystal evolution and morphological modifications. The AP-CVD arrangement provides more flexibility in controlling precursor movement and reaction kinetics than the sealed-tube method described by Xu et al., which makes it more appropriate for process optimization and scaling up. However, the narrow processing window associated with AP-CVD is highlighted by the strong dependence of crystal quality on precise temperature control and precursor concentration, posing ongoing challenges for producing uniform, defect-controlled, wafer-scale WS_2 films suitable for industrial production. Taken together, these findings demonstrate the broad applicability of CVD as a dependable and adaptable method for creating nanomaterials [45,106]. Fig. 11 shows the sample of the morphological modification, as demonstrated in MoS_2, while Table 3 outlines the various properties of the synthesis strategies.

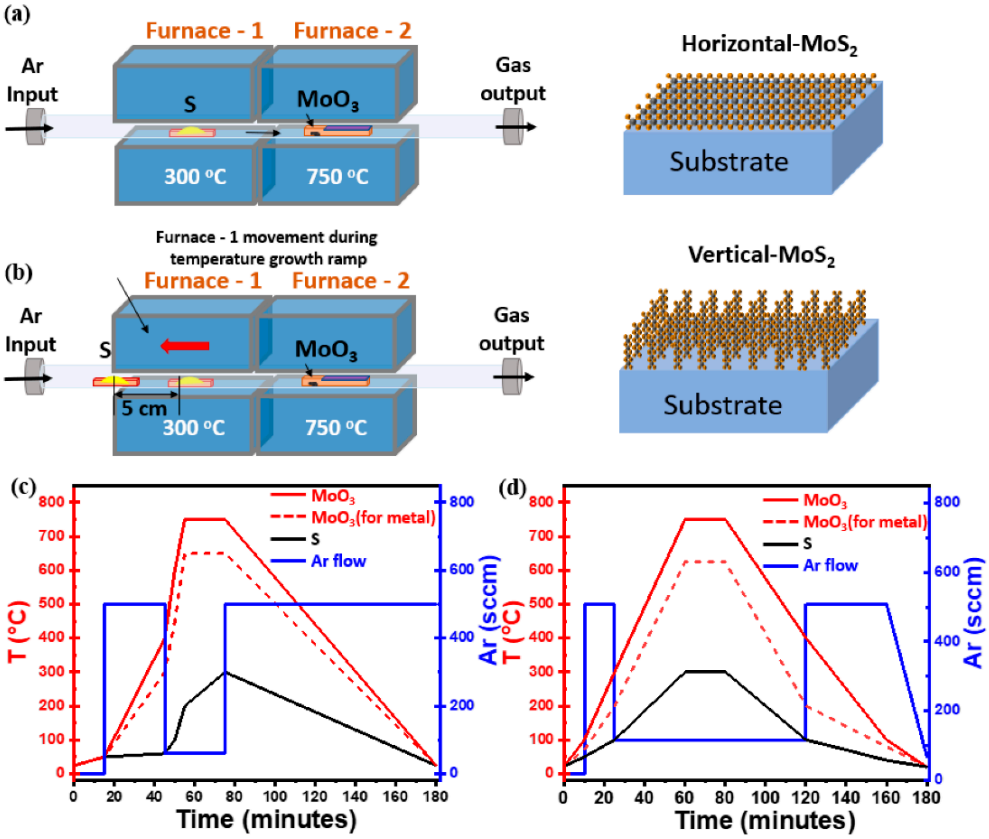

Figure 9: (**a**) Schematic diagram of the horizontal two-zone CVD furnace for the synthesis of flat-MoS_2. (**b**) Modified CVD setup used to synthesize vertical-MoS_2 nanosheets by adjusting the boat position during the growth temperature ramp on different substrates. (**c**) Different steps of temperature profile (left *y*-axis) adopted for the synthesis of flat-MoS_2 nanosheets with growth ramp at 750°C (solid line, SiO_2/Si) and 650°C (dash line, TaN) for 20 min; in the same graph the Ar flux changes during the CVD process are also plotted (blue solid line, right *y*-axis). (**d**) Three step temperature profile (left *y*-axis) used for the synthesis of vertical-MoS_2 nanosheets with growth ramp at 750°C (solid line, SiO_2/Si) and 625°C (dash line, TaN) for 20 min; in the same graph the Ar flux changes during the CVD process are also plotted (blue solid line, right *y*-axis). Reproduced from [147] under a Creative Commons Attribution (CC BY 4.0) license.

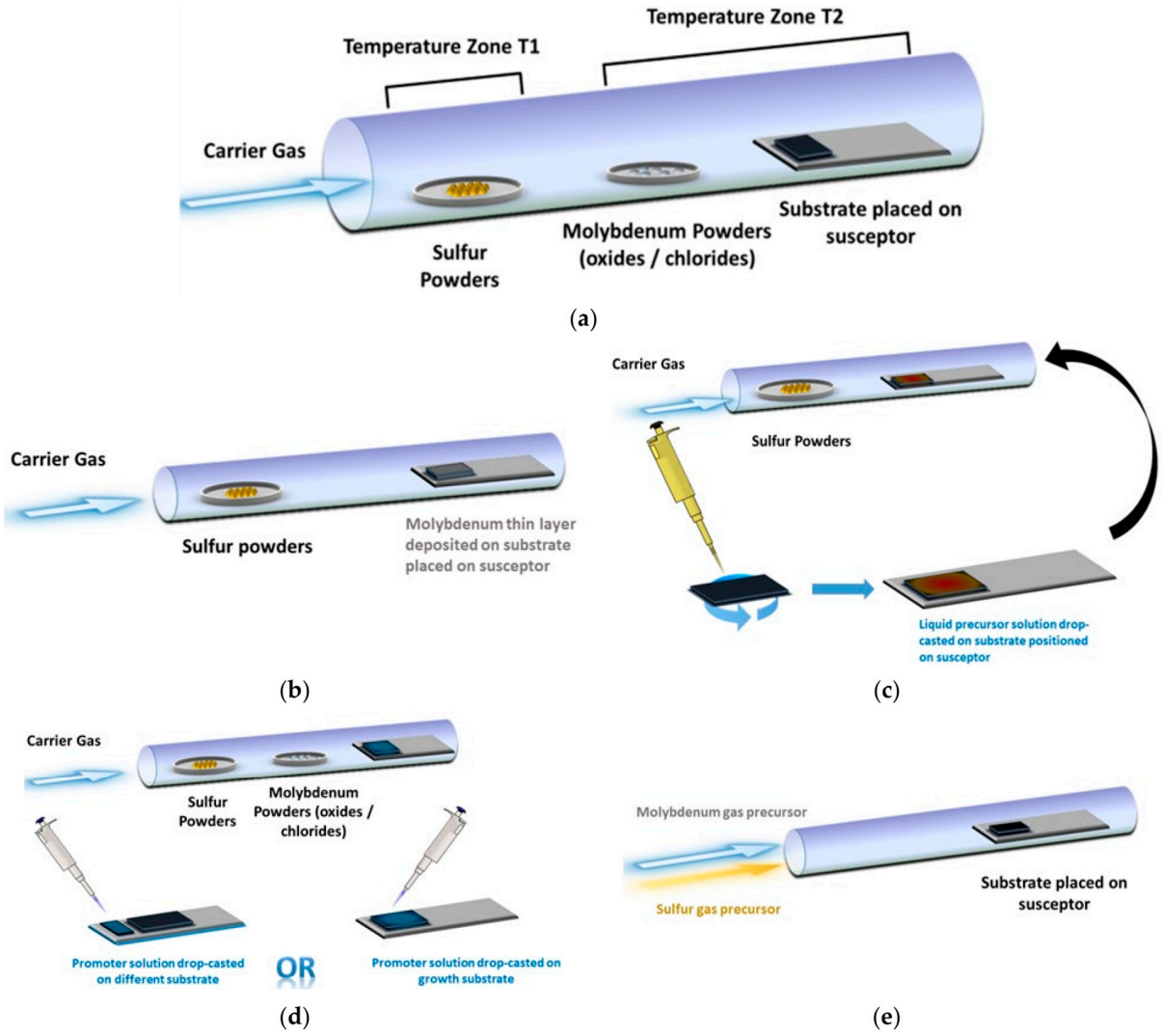

Figure 10: Schematic view of the CVD tube in different configurations for MoS_2 flake growth: (**a**) with solid precursors separated by substrate; (**b**) with solid molybdenum deposited on growth substrate; (**c**) with liquid molybdenum precursors; (**d**) with solid precursors and drop-casted promoters (either on growth substrate or a different substrate); (**e**) with gaseous precursors. Reproduced from [146] under a Creative Commons Attribution (CC BY 4.0) license.

Table 3: Comparison of synthesis strategies for 2D chalcogenides.

Method	Scaling Potential	Structural Quality	Phase Control	DFT Utility
Liquid-Phase Exfoliation	High	Moderate (polydisperse)	Limited	Solvent interaction & exfoliation energy
Ion Intercalation	Moderate	High	Excellent (2H to 1T)	Ion insertion energy & phase transition barrier
Chemical Vapor Deposition	Low to Medium	Excellent (large-area)	Very High	Growth kinetics, defect formation energy

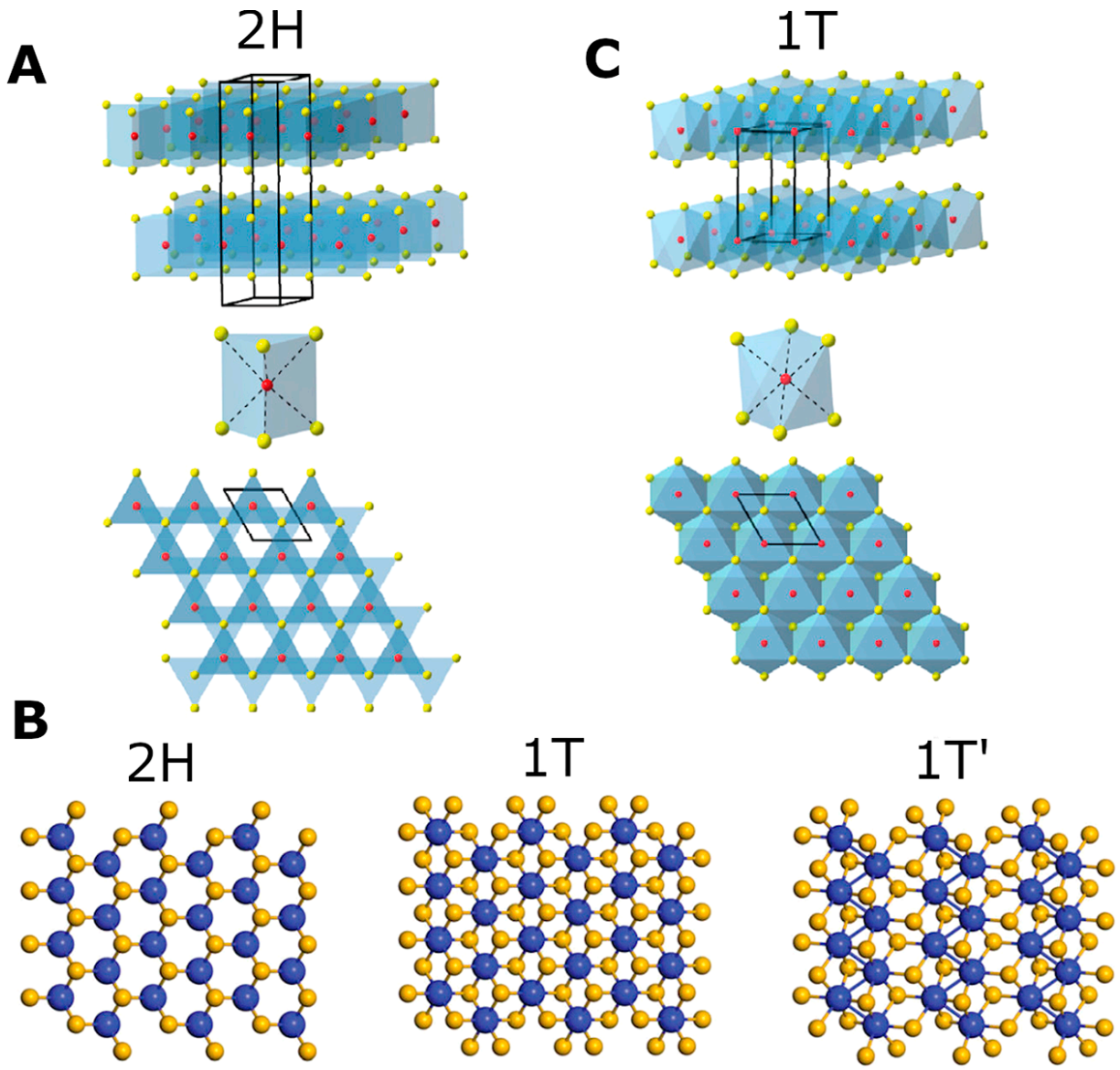

Figure 11: Structural representation of the polymorphs of MoS_2. Red/blue atoms indicate Mo, and yellow atoms depict S. (**A**) Alignment of atoms in two adjacent layers of 2H MoS_2, trigonal prismatic coordination of Mo atom, and top view (*c*-axis direction) of 2H nanosheet plane. (**B**) Top view of *c*-axis plane of the 2H, 1T, and 1T′ MoS_2. (**C**) Alignment of two adjacent layers of 1T MoS_2, octahedral coordination of Mo atom, and top view of 1T nanosheet plane. (**A**,**C**). Reproduce from [53] under a Creative Commons Attribution (CC BY 4.0) license.

3.3 Critical Synthesis Parameters Governing Reproducibility

The remarkable variation in electrochemical performance observed across investigations using seemingly equal or very similar synthesis techniques is one of the most enduring and significant issues in 2D chalcogenide research. TMC electrodes with specific capacities, rate capabilities, and cycling stabilities that differ by factors of two to five or more are frequently produced by nominally equivalent CVD or liquid-phase exfoliation processes carried out in different laboratories, or even within the same laboratory under slightly different ambient conditions. This disparity in repeatability is not solely due to measurement error and inconsistent electrochemical testing protocols. This phenomenon stems from the remarkable sensitivity of 2D

chalcogenide phase identity, defect concentration, layer number, and microstructural uniformity to a set of synthesis parameters that are frequently underreported, poorly controlled, or regarded as secondary variables in published studies. The CVD synthesis parameters covered by Tummala et al. [147] and Seravalli et al. [146], include temperature profile, furnace zone arrangement, substrate selection, and precursor identity. When these characteristics are not thoroughly described and controlled, they each have an independent impact on the final material qualities in ways that make direct cross-study comparison unreliable. Therefore, a thorough understanding of how each critical synthesis parameter affects the final material is necessary to translate laboratory results into scalable and reproducible electrode production processes.

3.3.1 Precursor Purity and Phase Selectivity

Precursor purity is the key factor influencing synthesis repeatability in both CVD and solution-based TMC production, despite being one of the most inconsistently reported parameters in the literature [150,151]. The vapor pressure profile of the molybdenum source during CVD synthesis of MoS_2 using MoO_3 and elemental sulfur is altered by trace impurities in MoO_3, particularly residual molybdenum suboxides (MoO_2 and MoO) resulting from incomplete oxidation during precursor preparation, according to Tummala et al. [147]. As a result, oxygen contaminates the developing TMC film, selectively stabilizing the 2H phase through substitution at sulfur vacancy sites. Even under growth conditions that are supposed to promote 1T formation, this suppresses the electronic reorganization required for the nucleation of the 1T phase, leading to 2H-dominant films.

The purity of ammonium tetrathiomolybdate (ATM) precursors has a major impact on the sulfur activity during crystallization for solution-based processes, such as the hydrothermal and solvothermal methods described in Section 3.1. Commercial ATM reagents of nominally equivalent purity grades from different suppliers exhibit measurable variations in residual oxide and water content during hydrothermal treatment, which alter the local sulfur-to-molybdenum chemical potential and shift the phase equilibrium between 2H and 1T products in ways that cannot be predicted from nominal synthesis conditions alone. Researchers trying to duplicate published results must specify not only the precursor grade but also the supplier, lot number, and storage conditions of all reagents because moisture absorption during storage can alter precursor reactivity and phase selectivity even within a single batch of nominally identical material.

3.3.2 Sulfur-to-Metal Ratio and Chalcogen Stoichiometry

The sulfur-to-metal (S/Mo) ratio supplied during CVD synthesis is the primary determinant of chalcogen stoichiometry and vacancy concentration in the final TMC film. At stoichiometric and superstoichiometric S/Mo ratios, the growing film approaches the ideal MoS_2 composition with low intrinsic vacancy density, producing a predominantly 2H-phase product with relatively low ion adsorption capacity but high structural stability during cycling. At substoichiometric S/Mo ratios, sulfur vacancies are introduced at concentrations proportional to the chalcogen deficit, enhancing ion adsorption and lowering diffusion barriers as discussed in Section 2.5, while simultaneously increasing susceptibility to 1T phase reversion during cycling as discussed in Section 2.6.

The practical challenge is that the effective S/Mo ratio experienced by the growing film is not simply the ratio of precursor masses loaded into the CVD furnace. As demonstrated in the two-zone furnace configuration employed by Tummala et al. [147] and shown in Fig. 9, it is determined by the vapor pressures of the sulfur and molybdenum sources at the growth temperature, the carrier gas flow rate transporting sulfur vapor to the substrate, the temperature gradient between the sulfur source and the substrate, and the residence time of sulfur vapor above the substrate surface. Small changes in any of

these variables alter the effective S/Mo ratio at the growth front independently of the loaded precursor ratio, explaining why nominally identical precursor loadings in different furnace configurations or at slightly different temperatures produce films with substantially different vacancy concentrations and electrochemical performances. Systematic calibration of the effective S/Mo ratio through post-synthesis XPS quantification of sulfur vacancy concentration, rather than reliance on loaded precursor ratios alone, is therefore essential for achieving reproducible defect engineering in CVD-grown TMC electrodes.

3.3.3 Carrier Gas Flow Rate and Vapor Transport

The local chalcogen partial pressure at the growth front is determined by the carrier gas flow rate, which also controls the movement of chalcogen vapor from the precursor source to the substrate surface [152,153]. As seen in the Ar flux patterns presented by Tummala et al. [147] in Fig. 9, argon is commonly used as the carrier gas in CVD synthesis of MoS_2 and WS_2 at flow rates ranging from 10 to 200 sccm depending on furnace design and tube diameter. Synthesis optimization studies often ignore the non-monotonic impact of carrier gas flow rate on phase composition and film quality within this range [152,153].

At low flow rates, sulfur vapor collects above the substrate and provides a locally high chalcogen partial pressure that supports stoichiometric growth with low vacancy density. The chalcogen partial pressure is lowered to a level that introduces regulated vacancy concentrations while preserving an adequate supply of sulfur for ongoing film growth at intermediate flow rates. Rapid removal of sulfur vapor from the growth zone at high flow rates produces a highly chalcogen-deficient environment that can promote phase-selective 1T nucleation at the expense of decreased film uniformity and increased surface roughness [152,153]. In addition to its direct effect on chalcogen partial pressure, carrier gas flow rate influences the residence time of volatile molybdenum suboxides above the substrate, which influences nucleation density and, in turn, the final grain size and domain boundary density of the film. Grain boundaries are favored sites for both ion intercalation and structural degradation during cycling; therefore, carrier gas flow rate simultaneously influences stoichiometry, phase composition, and grain microstructure, which has a compound effect on electrochemical performance.

3.3.4 Heating Ramp Rate and Nucleation Control

The heating ramp rate from ambient to the target growth temperature determines the nucleation density of TMC domains, which in turn determines the ultimate grain size, layer number uniformity, and phase composition of the deposited film. The temperature profiles published by Tummala et al. [147,154,155] for flat and vertical MoS_2 development in Fig. 9 demonstrate how alternative ramp profiles applied to the same furnace configuration result in films with distinct morphologies and phase compositions. This demonstrates that the ramp rate is not a procedural feature but rather an independent synthesis variable.

In the early phases of growth, rapid heating ramps provide high supersaturation of reactive vapor species at the substrate surface, which promotes high nucleation density and results in films with small grain sizes, high domain border density, and generally uniform layer thickness [154,155]. Slow heating ramps reduce the concentration of reactive monomer species available for surface nucleation and produce films with larger grain sizes and more layer-to-layer thickness variability by allowing precursor decomposition products to pre-react in the gas phase for extended periods of time at intermediate temperatures. The ideal ramp rate for electrochemical energy storage applications is a compromise: while small grains with high boundary density maximize surface area and edge site availability but add more sites for structural degradation and phase reversion, large grains with low boundary density minimize structural degradation during cycling but decrease accessible surface area for ion adsorption. Therefore, it is crucial for synthesis

methods to precisely specify the heating ramp rate in order to direct researchers toward the appropriate microstructural regime for their intended use.

3.3.5 Cooling Rate and Phase Preservation

A crucial but often overlooked synthesis parameter, the cooling rate after TMC film formation, impacts whether the phase composition created during growth is maintained or changed upon return to ambient temperature [147,152,155]. The cooling rate directly impacts the likelihood of 1T to 2H phase reversion before the film reaches ambient temperature for 1T-phase TMC films formed under kinetic phase selection conditions. This is because the cooling rate controls the thermal energy available to the system during the post-growth period.

By quickly lowering the thermal energy available for chalcogen plane glide, rapid cooling from the growth temperature to below around 200°C, which may be accomplished by removing the substrate from the furnace hot zone right after development, kinetically traps the 1T phase composition [155]. By keeping the film at temperatures where the reversion barrier may be thermally overcome for prolonged periods, slow furnace cooling gradually transforms 1T domains into 2H and results in a final phase composition that is significantly different from that at the growth temperature. Cooling rate variation within a single CVD protocol results in measurably different structural outcomes, as demonstrated by the cooling profiles reported by Tummala et al. [147] in Fig. 9. This provides direct experimental evidence that cooling rate must be specified and standardized along with growth temperature and precursor conditions in reproducible synthesis protocols. This cooling-rate-dependent phase evolution has been directly visualized by studies using *in situ* Raman spectroscopy during controlled cooling. These studies show that the 1T phase fraction in MoS_2 films decreases monotonically with decreasing cooling rate and that films cooled at rates below about 5°C per minute retain less than 50% of the 1T phase fraction present at the growth temperature.

3.3.6 Substrate Selection and Epitaxial Constraints

Three mechanistically different pathways are used by substrate selection to affect TMC film growth: chemical interaction between the substrate surface and TMC precursors, epitaxial strain imposed by lattice mismatch between the substrate and the growing film, and substrate thermal conductivity, which determines the local temperature gradient experienced by the growing film [147,156]. By comparing film morphology and quality on SiO_2/Si and TaN substrates using identical precursor conditions, Tummala et al. [147] clearly illustrated the substrate dependence of MoS_2 CVD growth. They discovered that different substrates required different growth temperatures and produced films with distinct structural characteristics despite nominally equivalent synthesis protocols. This substrate sensitivity links the synthesis repeatability topic to the larger context of TMC heterostructure production and is directly related to the review's discussion of TaN as a substrate material.

Through geometric lattice matching and van der Waals epitaxy, epitaxial substrates including c-plane sapphire, mica, and hexagonal boron nitride encourage oriented TMC film formation, resulting in films with preferred grain orientations and less rotational disorder than amorphous SiO_2 substrates. A direct mechanistic connection between substrate choice and phase engineering results is established by the lattice mismatch between the substrate and the TMC overlayer, which introduces biaxial strain that, as covered in Section 2.5.3, can promote the 2H to 1T transition when tensile and suppress it when compressive. In fundamental research contexts, the preference for epitaxially ideal substrates may be superseded by practical constraints such as compatibility with electrode fabrication processes, electrolyte stability, and current collector integration when choosing a substrate for electrochemical device applications [157,158].

3.3.7 Defect Concentration Control and Characterization-Guided Synthesis

Achieving reproducible and targeted defect concentrations in 2D TMC electrodes requires a shift from empirical synthesis optimization toward characterization-guided defect engineering [159,160]. Defect concentration is not a directly controllable synthesis variable but an emergent property of the combined influence of precursor purity, S/Mo ratio, carrier gas flow, temperature profile, and substrate chemistry described in the preceding subsections. Small and difficult-to-control variations in any of these parameters translate into significant and often unpredictable variations in final vacancy concentration, producing the performance variability that currently limits direct comparison between studies in the 2D chalcogenide literature [27,161].

Establishing a reproducible defect engineering protocol therefore requires closing the feedback loop between synthesis and characterization. Post-synthesis XPS quantification of the S/Mo atomic ratio, as employed across the studies reviewed in Section 4, provides a direct measure of bulk vacancy concentration. Atomic-resolution ADF-STEM enables direct visualization and counting of individual vacancy sites, while Raman spectroscopy provides a rapid non-destructive probe of vacancy concentration through the vacancy-induced broadening and red-shifting of the A_{1g} mode, enabling high-throughput screening across large sample sets. By developing calibration curves that correlate specific synthesis parameters with XPS-measured vacancy concentrations and Raman spectroscopic signatures, researchers can design synthesis parameter windows that consistently produce targeted vacancy concentrations within predefined tolerance ranges. This method transforms defect engineering from an empirical approach into a quantitatively controlled fabrication workflow.

If the 2D chalcogenide research community embraced characterization-guided synthesis procedures, the performance variability that currently hinders direct cross-study comparison and makes it challenging to establish true material performance limits would be greatly reduced. For publications in this field that aim to provide truly reproducible and actionable synthesis guidance, standardized reporting of all seven synthesis parameters discussed in this section, along with post-synthesis characterization data verifying phase composition, vacancy concentration, and microstructural properties of the electrode material, should be regarded as a minimum reporting requirement [159,162,163].

4 Characterization Techniques for 2D Chalcogenides

Characterization is an essential link between synthesis and performance evaluation. It provides crucial evidence of effective defect engineering, phase transitions, and structural alterations in 2D chalcogenide nanomaterials. Density Functional Theory (DFT) theoretical predictions are correlated with modern spectroscopic, microscopic, and electrochemical techniques used to verify the quality of synthesized materials.

4.1 Spectroscopic Analysis: Raman and XPS

Researchers can examine the structural and chemical characteristics of 2D chalcogenide nanomaterials without harming the sample by using spectroscopic techniques that provide non-destructive fingerprinting. The most popular methods for verifying phase transitions, locating defect structures, and assessing chemical composition are Raman spectroscopy and X-ray photoelectron spectroscopy (XPS).

Raman spectroscopy is particularly useful for distinguishing between the semiconducting 2H phase and the metallic 1T phase. The 2H phase often exhibits two unique vibrational modes: the in-plane E^1_{2g} mode and the out-of-plane A_{1g} mode. During the transition to the 1T phase, these peaks weaken, shift, or widen due to changes in lattice symmetry. More importantly, new features known as J peaks (J_1, J_2, and J_3) show the decreased symmetry associated with octahedral coordination in the 1T phase.

An excellent example of Raman spectroscopy's capabilities is found in the publication MoS_2 Coexisting in 1T and 2H Phases Synthesized by Common Hydrothermal Method for Hydrogen Evolution Reaction. In this work, MoS_2, including both 1T and 2H phases with improved catalytic capabilities, was generated using a hydrothermal process followed by a solvothermal treatment. The two main activation modes for the 2H phase was identified by Raman spectra (Fig. 12) A_{1g} at 404 cm^{-1}, which corresponds to out-of-plane vibrations of sulfur atoms, and E^1_{2g} at 379 cm^{-1}, which results from in-plane vibrations of Mo and S atoms [164,165]. These fingerprints verified the structural changes brought about by synthesis and directly confirmed the coexistence of both phases.

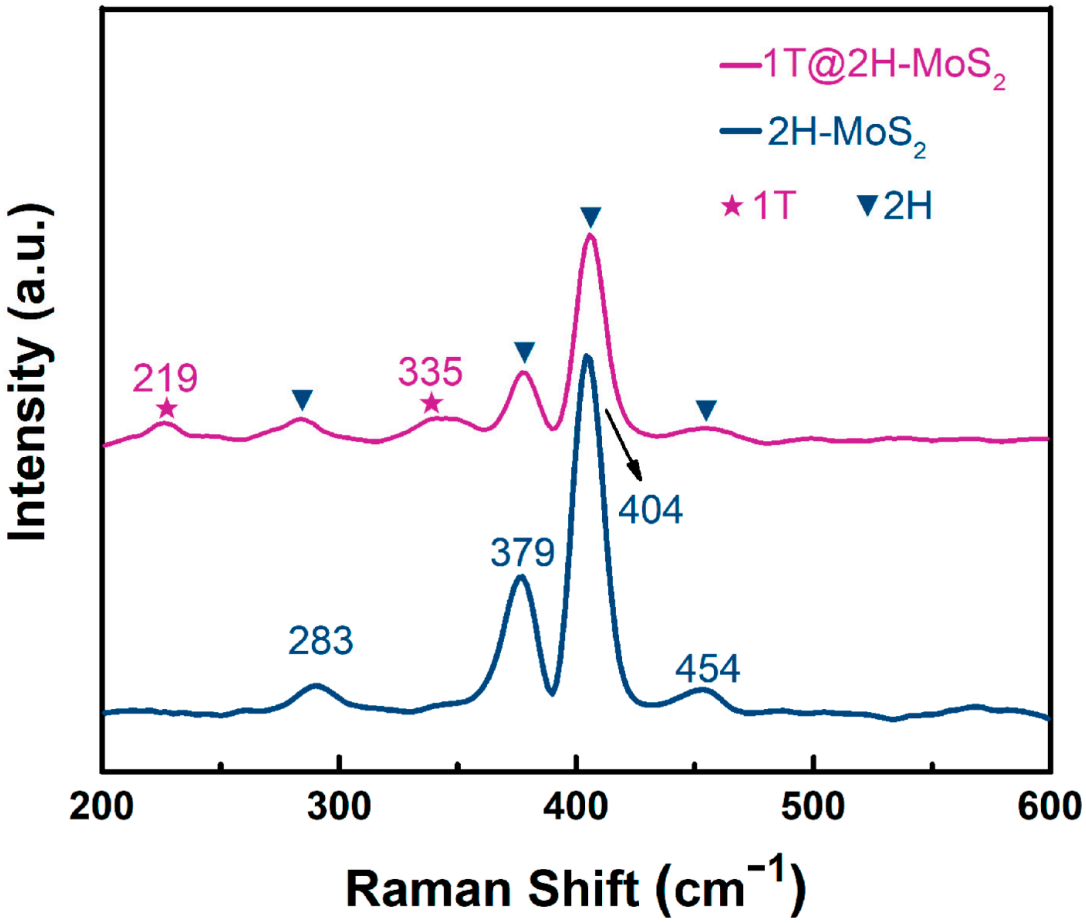

Figure 12: Raman spectrum of 1T@2H-MoS_2 and 2H-MoS_2. Reproduced from [166] under a Creative Commons Attribution (CC BY 4.0) license.

The existence and strength of these J-peaks are trustworthy markers of a successful phase transition to the metallic state [17,167].

The existence and strength of these J-peaks are trustworthy markers of a successful phase transition to the metallic state [18,106]. Raman and XPS together provide complementary information, with one revealing structural symmetry and phase identity, and the other revealing chemical composition and defect chemistry, forming a robust foundation for understanding the quality of synthesized 2D chalcogenide nanomaterials (see Fig. 13).

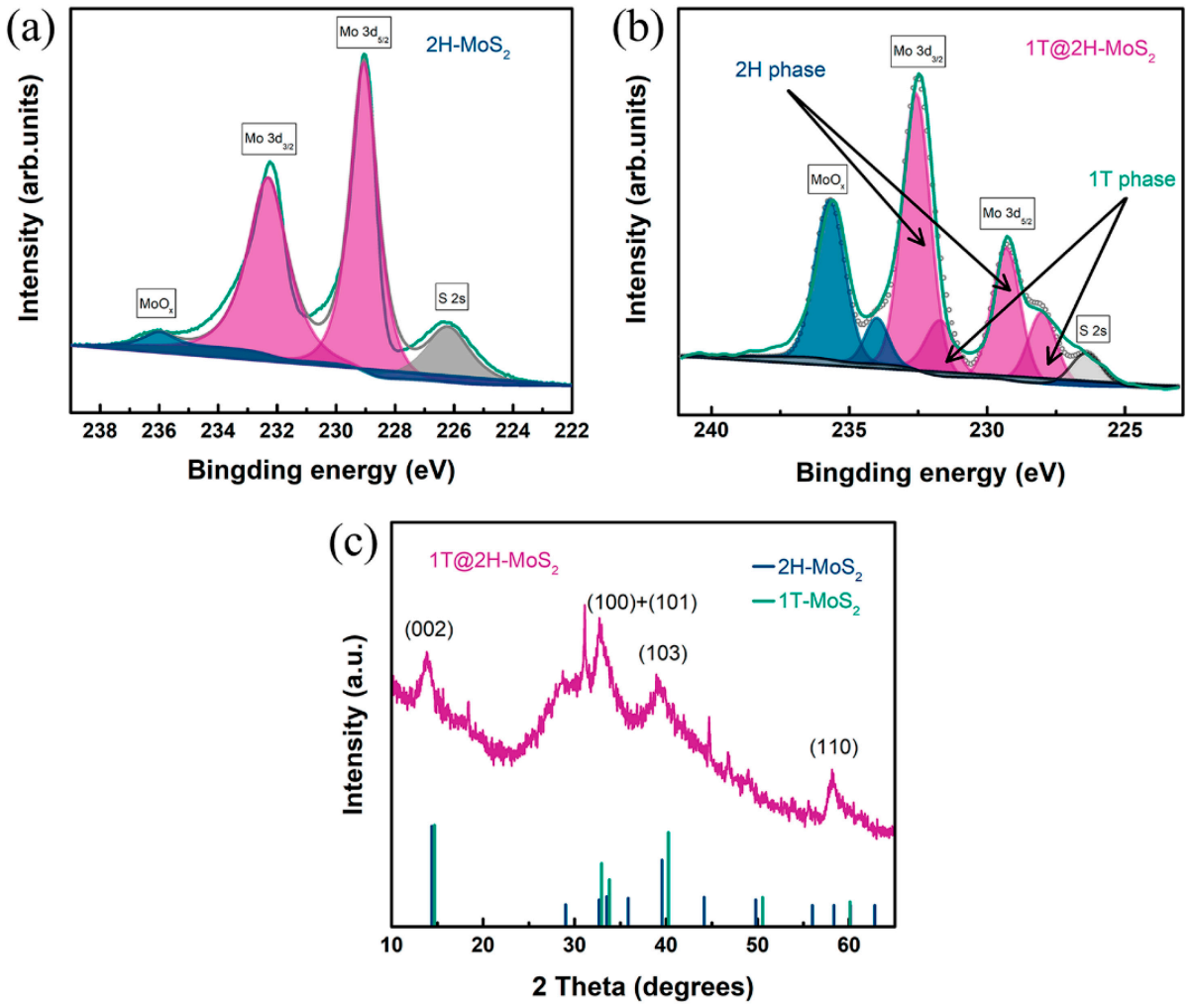

Figure 13: X-ray photoelectron spectroscopy (XPS) spectra of (**a**) 2H-MoS_2 and (**b**) 1T@2H-MoS_2, (**c**) XRD of 1T@2H-MoS_2. Reproduced from [166] under a Creative Commons Attribution (CC BY 4.0) license.

4.2 Microscopic Imaging: HR-TEM and AFM

While spectroscopic techniques provide averaged information about structural and chemical changes, microscopic techniques provide direct visual evidence at the nanoscale and atomic scale. Among these, high-resolution transmission electron microscopy (HR-TEM) and atomic force microscopy (AFM) are the most commonly used tools for characterizing 2D chalcogenide materials.

High-Resolution Transmission Electron Microscopy (HR-TEM) allows direct observation of atomic organization, grain boundaries, lattice fringes, and structural defects. It can clearly distinguish between the trigonal prismatic (2H) and octahedral (1T) coordination, and it reveals lattice distortions associated with chalcogen vacancies, strain, or phase transitions [32] (see Fig. 14).

Atomic Force Microscopy (AFM) is indispensable for measuring the thickness of nanosheets. By measuring step heights with sub-nanometer precision, AFM confirms whether the synthesized material consists of only a few atomic layers (typically 1 to 10 layers), thereby verifying the successful achievement of true two-dimensionality (see Fig. 14).

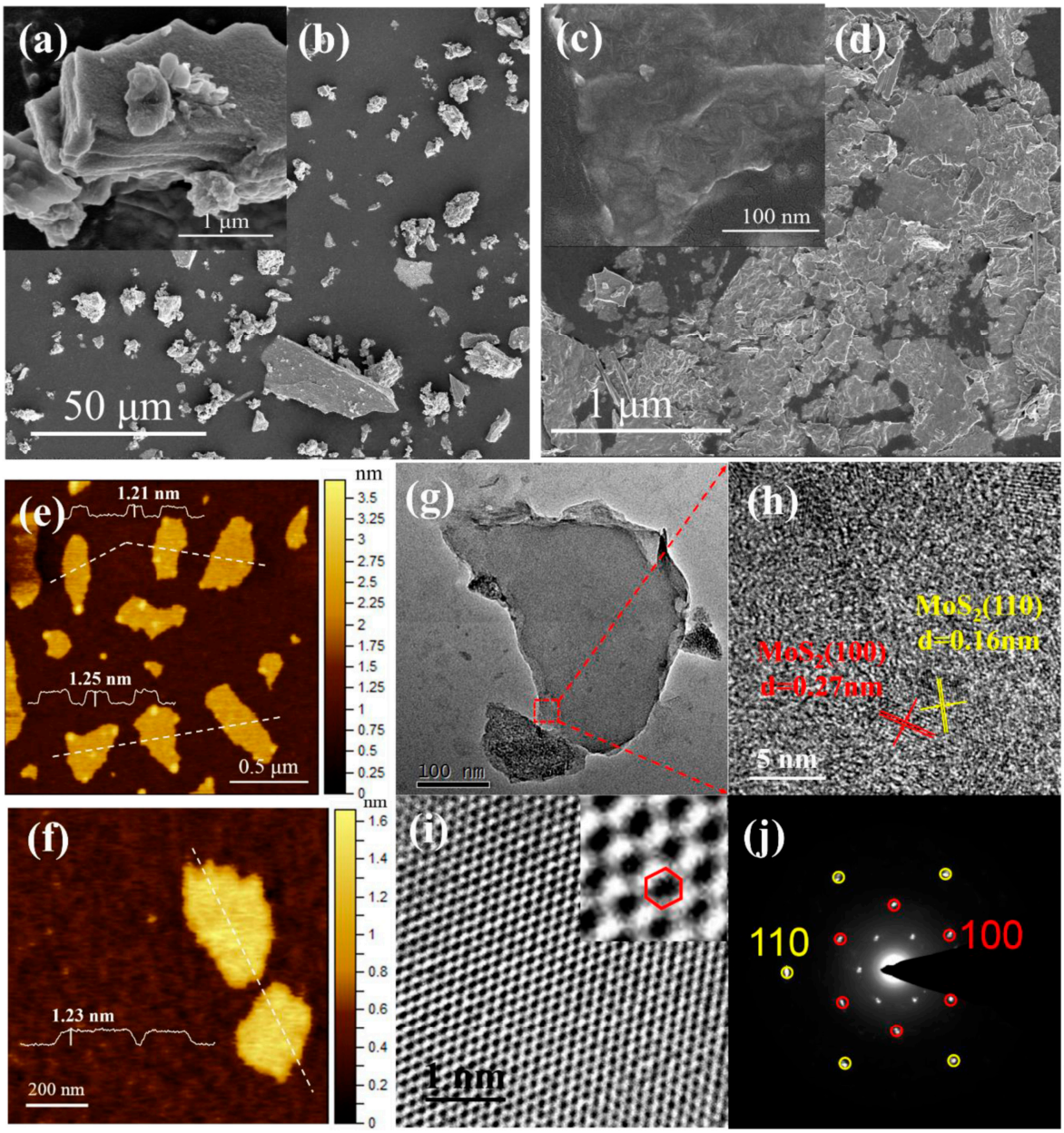

Figure 14: Field emission scanning electron microscope (FESEM) images (**a**–**d**) of the bulk MoS_2 and MoS_2-NS, atomic force microscope (AFM) images (**e**,**f**), height profiles (inset), (transmission electron microscope) TEM and high-resolution transmission electron microscope (HRTEM) images of MoS_2 nanosheets (**g**–**i**), and the fast Fourier transforms (FFT) pattern of MoS_2 NS (**j**). Scale bars are indicated in the original figure. Reproduced from [168] under a Creative Commons Attribution (CC BY 4.0) license.

In the context of local resources, HR-TEM and AFM can also reveal whether natural impurities in Nigerian ores act as natural pillars that maintain expanded interlayer spacing [1].

4.3 Electrochemical Characterization

Since the ultimate goal of developing 2D chalcogenide nanomaterials is their integration into energy storage devices, electrochemical characterization techniques are essential to evaluate real-world perfor-

mance under operating conditions. These methods directly assess how structural modifications, such as phase transitions, defect engineering and heterostructure formation, translate into improved charge storage capacity, rate capability, and cycling stability.

One essential method for locating redox peaks connected to ion intercalation and deintercalation processes is cyclic voltammetry (CV). Increased peak current densities and a discernible change in peak location toward lower potentials frequently signify improved electronic conductivity and a successful transition from the semiconducting 2H phase to the metallic 1T phase. The electrochemical behavior of MoS_2 electrodes made on fluorine-doped tin oxide (FTO) substrates was examined using CV in [169], which confirmed the enhanced electrochemical activity of the produced material and revealed unique redox characteristics related to ion transport (see Fig. 15).

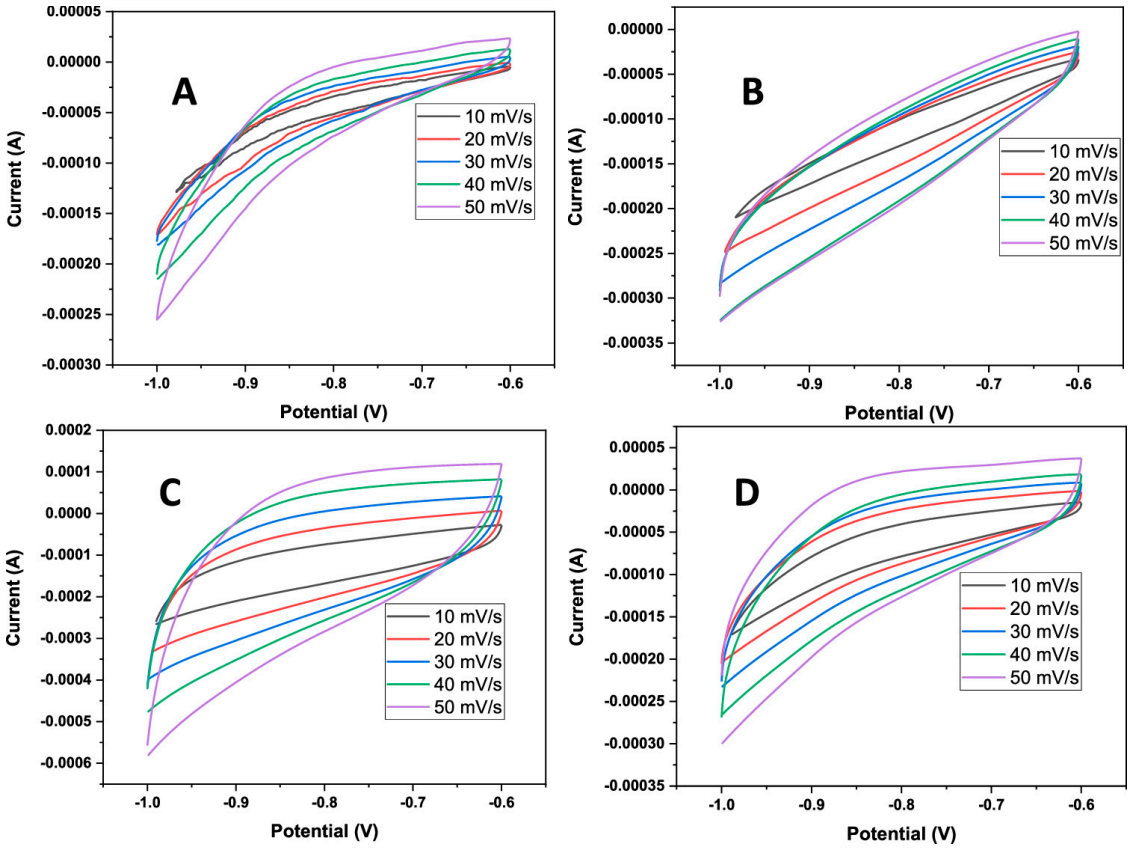

Figure 15: Graphical representation of CV signature of various samples of MoS_2 exfoliated in (**A**) ethanol, (**B**) EG, (**C**) DMF, and (**D**) DMSO. Reproduced from [169] under a Creative Commons Attribution (CC BY 4.0) license.

Similarly, the energy barrier for ion insertion can be lowered by the presence of chalcogen vacancies, leading to improved pseudocapacitive behavior and increased specific capacity [4,170].

To gain a deeper understanding of the kinetic limitations and resistance processes seen in CV, electrochemical impedance spectroscopy (EIS) is employed as an additional method. While CV displays the general charge-storage behavior, EIS measures the specific resistive and diffusive processes within the electrode. In particular, it monitors the charge-transfer resistance (Rct) and ion diffusion kinetics at the electrode-electrolyte interface. A significant decrease in Rct provides strong evidence of improved elec-

tronic conductivity, typically resulting from the formation of the highly conductive 1T phase or optimal defect topologies.

Furthermore, by examining the Warburg impedance zone in the Nyquist plot (see Fig. 16), ion diffusion behavior can be comprehended. Improved Warburg characteristics suggest faster ion transport, which is necessary for high power performance in supercapacitors and batteries [170]. Combining CV and EIS provides a comprehensive understanding of how structural engineering methods lead to improved electrochemical functionality.

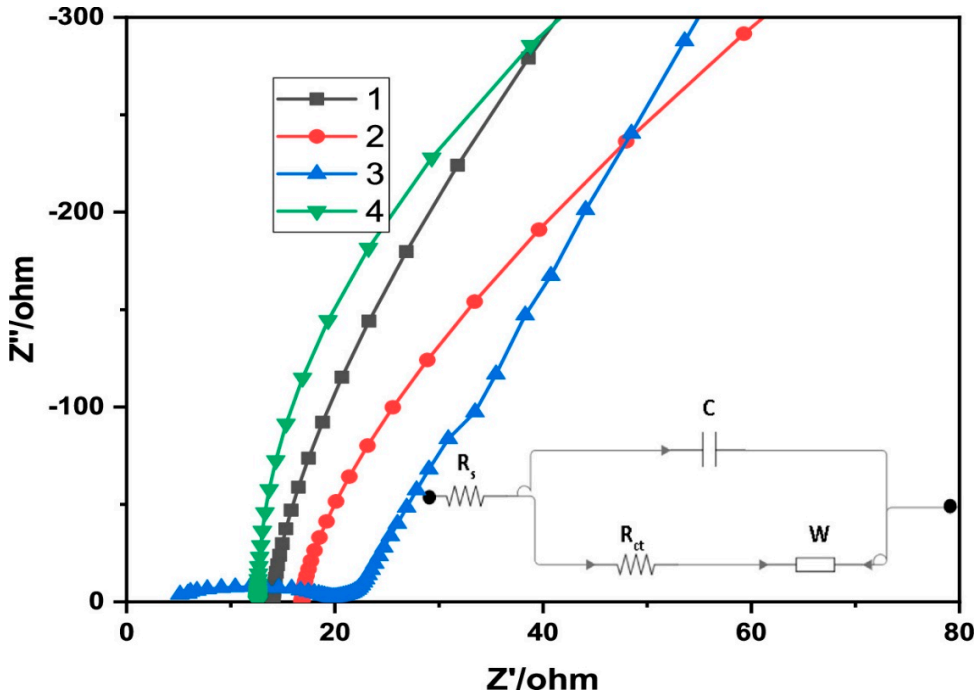

Figure 16: Figure 16: Plot showing Nyquist plot of MoS_2 samples exfoliated in (1) ethanol, (2) EG, (3) DMF, and (4) DMSO along with equivalent impedance circuit diagram. Reproduced from [169] under a Creative Commons Attribution (CC BY 4.0) license.

4.4 The DFT Approach to Characterization

While experimental methods provide direct measurements, Density Functional Theory (DFT) is a powerful auxiliary tool that links experimental results with fundamental understanding. DFT is crucial not just for prediction but also for the interpretation and validation of characterization data. DFT calculations yield simulated Raman spectra and XPS binding energies that may be directly compared with experimental results to accurately confirm phase identity (2H vs. 1T) and assess defect concentrations. Additionally, the electron-density distribution and the Electron Localization Function (ELF) demonstrate how chalcogen vacancies generate localized electronic states that act as hotspots for ion adsorption—electronic features that are invisible through traditional spectroscopy or microscopy [25,106]. Thanks to DFT.

By combining DFT with experimental characterization, researchers are able to fully understand structure-property connections. This combination approach not only verifies successful synthesis but also guides further 2D chalcogenide tailoring for enhanced electrochemical energy storage performance. Table 4 (collected and amended based on the literature, particularly [27,164], and related investigations) lists the primary characterization techniques.

Table 4: Summary of key characterization techniques for 2D chalcogenides and their link to DFT.

Technique	Primary Information Gained	Link to DFT Approach
Raman Spectroscopy	Phase identification (2H vs. 1T), vibrational modes	Comparison of experimental spectra with DFT-simulated vibrational modes
X-ray Photoelectron Spectroscopy (XPS)	Elemental composition, oxidation states, vacancy concentration	Validation of experimental binding energies against DFT-calculated values
High-Resolution Transmission Electron Microscopy (HR-TEM)	Atomic-scale structure, lattice defects, phase boundaries	Visual confirmation of DFT-predicted lattice distortions and defect structures
Electrochemical Impedance Spectroscopy (EIS)	Charge-transfer resistance (R_{ct}), ion diffusion kinetics	Correlation with DFT-calculated diffusion barriers (E_a) and charge transfer properties

5 Energy Storage Applications, Challenges, and Future Perspectives

To assess the practical performance of 2D chalcogenide nanomaterials in actual electrochemical energy storage devices (EESDs), this final chapter combines the synthesis procedures, characterization methods, and DFT-based theoretical insights covered in previous sections. It also suggests prospective paths for converting laboratory success into industrial applications and critically evaluates the current obstacles.

5.1 Performance in Supercapacitors and Batteries

Because of their large surface area, adjustable interlayer spacing, and diverse electrical characteristics, two-dimensional transition metal chalcogenides (TMCs) are mainly used in batteries and supercapacitors, the two main types of EESDs. The layered X-M-X structure is a great host for reversible ion intercalation in lithium-ion batteries (LIBs) and particularly sodium-ion batteries (SIBs). SIBs are more difficult because Na^+ has a greater ionic radius than Li^+, but TMCs' metallic 1T phase dramatically reduces the diffusion energy barrier, improving rate performance and cycling stability. Because of this, 2D TMCs are especially promising for large-scale, affordable stationary energy storage [4,167]. Because they can combine electric double-layer capacitance with pseudocapacitive charge storage, 2D chalcogenide nanomaterials are excellent in supercapacitors. High power density and superior rate capability are produced by the 1T phase's high electrical conductivity combined with quick surface redox reactions made possible by chalcogen vacancies and increased interlayer spacing (see Figs. 17 and 18). These features allow 2D TMC-based electrodes to deliver fast charge–discharge behavior while maintaining structural stability over extended cycling.

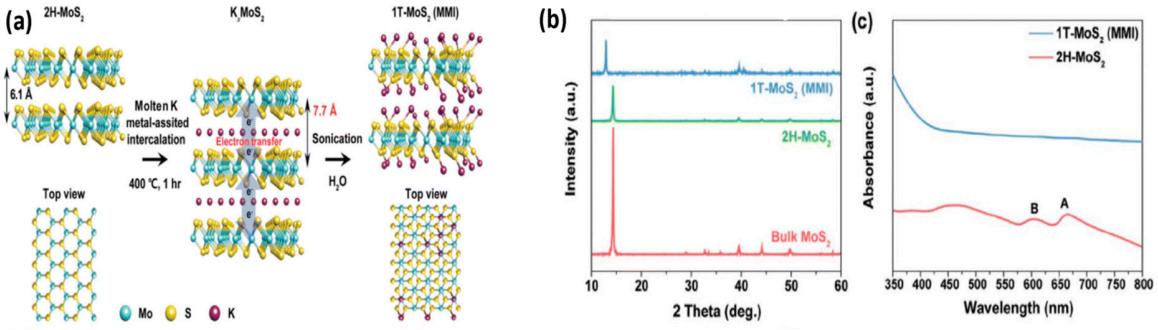

Figure 17: *Cont.*

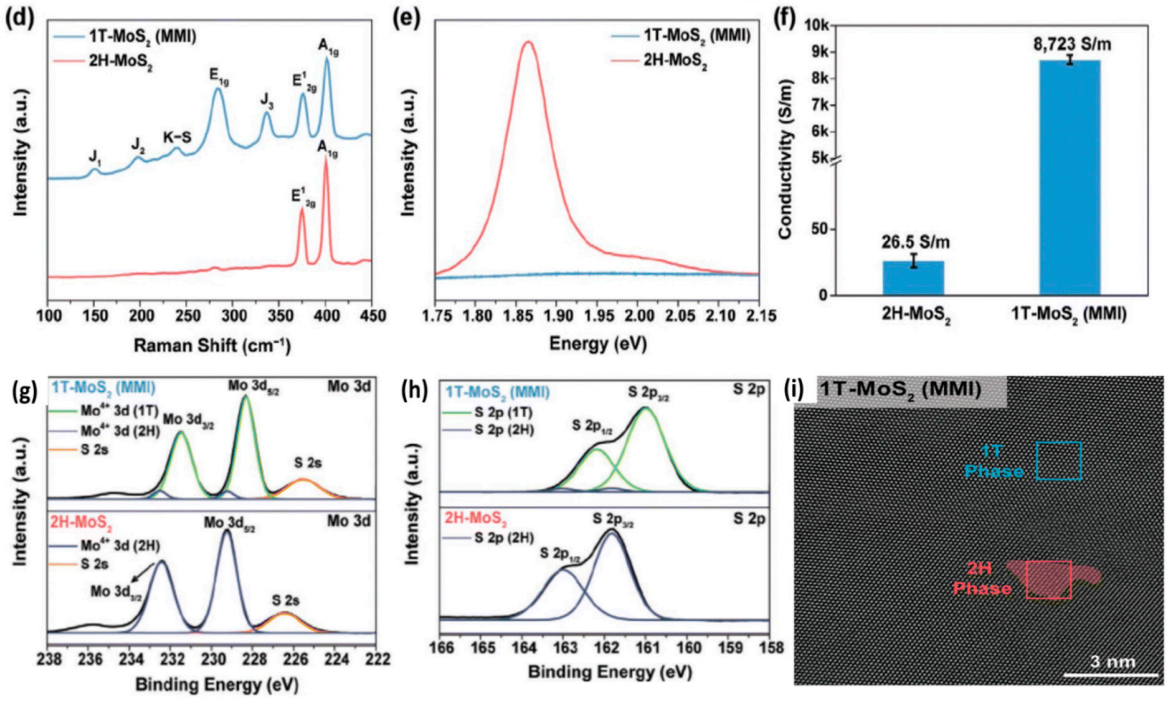

Figure 17: (**a**) Representation conversion of 2H-MoS_2 to 1T-MoS_2, (**b**) comparison of XRD spectra of 1T-MoS_2 (MMI), 2H-MoS_2 nanosheets, and bulk MoS_2, (**c**) UV-Vis–NIR spectra of 1T-MoS_2 (MMI) and 2H-MoS_2, (**d**) Raman spectra of 1T-MoS_2 (MMI) and 2H-MoS_2, (**e**) PL spectra of 1T-MoS_2 (MMI) and 2H-MoS_2, demonstrating the enhanced charge transfer in metallic 1T-MoS_2, (**f**) comparison of electrical conductivities between 1T-MoS_2 (MMI) and 2H-MoS_2 nanosheets, (**g**,**h**) XPS spectra of 1T-MoS_2 (MMI) and 2H-MoS_2, showing the Mo 3d, S 2p, and (**i**) HRTEM image of intercalated 1T-MoS_2, zoomed images of two phases (2H and 1T phase), Reproduced from [171] under a Creative Commons Attribution 3.0 Unported Licence.

These materials can endure rapid charge-discharge cycles with minimal structural degradation, outperforming traditional carbon-based electrodes in high-power applications [22].

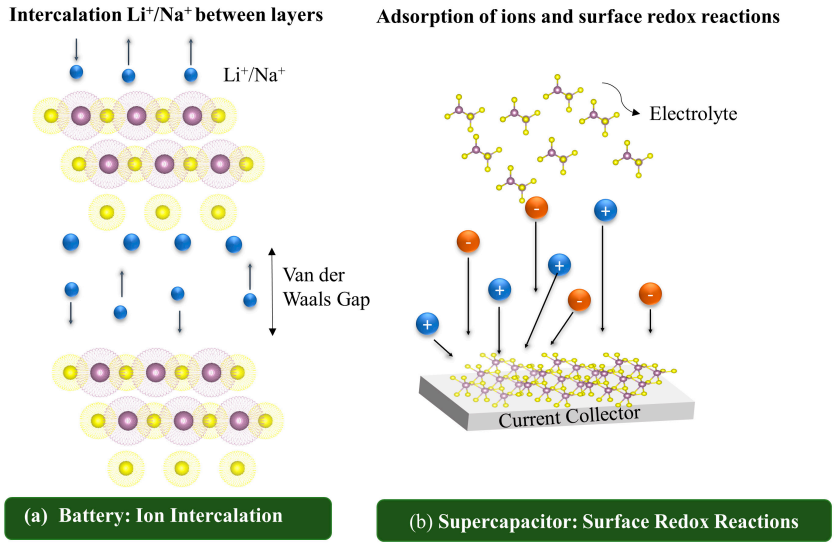

Figure 18: Schematic representation of 2D chalcogenide nanomaterials (e.g., MoS_2) in (**a**) lithium/sodium-ion batteries (ion intercalation) and (**b**) supercapacitors (surface redox reactions). Adapted from [22,167].

Dynamic in-Operando Phase Transitions during Electrochemical Cycling

The static characterization of 2H and 1T phase compositions in 2D chalcogenide electrodes, while essential for understanding the initial material properties, does not capture the dynamic structural evolution that occurs during the actual charging and discharging process in alkali-ion batteries. In-operando studies employing synchrotron X-ray diffraction, *in situ* Raman spectroscopy, and operando transmission electron microscopy have demonstrated that the phase composition of TMC electrodes evolves continuously and reversibly during electrochemical cycling, with the degree and rate of dynamic phase evolution being strongly dependent on the applied current density, the ion chemistry, and the depth of discharge [172].

During lithiation of 2H-MoS_2, ion intercalation progressively expands the interlayer spacing and transfers electrons to the MoS_2 layer, partially populating the conduction band and shifting the electronic structure from semiconducting toward metallic [173]. In-operando XRD studies reveal that this electronic restructuring is accompanied by a gradual shift of the MoS_2 (002) diffraction peak to lower angles, indicating continuous interlayer expansion of approximately 0.3 to 0.8 Å during initial lithiation, followed by the emergence of a new diffraction peak corresponding to a lithiated MoS_2 phase (Li_xMoS_2) with a modified stacking sequence [174]. At high lithiation depths corresponding to x greater than 0.5 in Li_xMoS_2, in-operando Raman spectroscopy reveals the progressive weakening of the 2H-characteristic E^1_{2g} and A_{1g} modes and the simultaneous growth of J-band features characteristic of local 1T coordination, confirming that deep lithiation drives a partial in-operando 2H to 1T phase transition that is not present in the as-synthesized electrode [174,175].

For sodiation of MoS_2, the larger ionic radius of Na^+ amplifies the magnitude of interlayer expansion during in-operando cycling, with operando XRD studies reporting interlayer spacings of up to 7.8 Å at full sodiation compared to the native 6.2 Å. This expansion of approximately 26% is accompanied by a more pronounced in-operando phase transition than observed during lithiation, with a larger fraction of 2H domains converting to 1T-like coordination at equivalent intercalation depths. The greater driving force for in-operando phase conversion during sodiation relative to lithiation is consistent with the DFT-predicted lower 2H to 1T transition barrier in the presence of larger interlayer strain, as discussed in Section 2.5, and provides a mechanistic explanation for the experimentally observed non-linear relationship between Na^+ storage capacity and current density in MoS_2 electrodes: at low current densities, sufficient time is available for the in-operando phase transition to occur and contribute additional metallic-phase capacity, while at high current densities, the kinetic limitation of the structural transition suppresses this contribution and reduces the total accessible capacity [176].

Crucially, complete desodiation or delithiation does not completely reverse the in-operando phase change. The fraction of 1T-like coordination retained after a full charge-discharge cycle is consistently higher in in-operando and *ex-situ* comparative Raman studies than in the as-synthesized material, suggesting that each cycle leaves a residual accumulation of 1T domains that gradually alters the electrode's phase composition over prolonged cycling. By raising the conducting phase fraction, this cycle-by-cycle 1T accumulation first improves electrode performance. However, as the accumulated 1T fraction increases, the thermodynamic driving force for reversion during rest periods or elevated-temperature operation eventually contributes to the thermodynamically driven 1T-to-2H reversion covered in Section 2.6. Optimizing the long-term electrochemical performance of 2D chalcogenide electrodes in realistic alkali-ion battery applications requires understanding and control of this dynamic phase evolution through temperature control, operating voltage window selection, and synthesis-defined initial phase composition [7,176].

5.2 Comparative Analysis of Li^+, Na^+, and K^+ Storage Mechanisms in 2D Chalcogenide Electrodes

It is common to consider the electrochemical storage of potassium, sodium, and lithium ions in 2D chalcogenide electrodes as a single phenomenon controlled by the same intercalation mechanisms. These three alkali metal ions, however, have sufficiently different physical and chemical characteristics that their storage methods, kinetic constraints, structural implications, and ideal electrode design requirements are essentially different [177]. Understanding why electrode compositions and synthesis conditions that provide excellent performance in lithium-ion systems often underperform in sodium-ion and potassium-ion applications, and *vice versa*, requires a thorough comparative analysis based on ionic radius, desolvation energy, adsorption energy, diffusion barrier, volume expansion, and interlayer spacing requirements [5,177].

5.2.1 Ionic Radius and Its Structural Consequences

Li^+, Na^+, and K^+ have ionic radii of around 0.76, 1.02, and 1.38 Å, respectively, which indicate an 81% rise from lithium to potassium. The structural compatibility of each ion with the van der Waals gallery of 2D chalcogenide hosts is directly and quantitatively affected by this size progression. MoS_2's native interlayer spacing in its 2H phase is around 6.2 Å, which permits Li^+ intercalation with minimal lattice strain [47,178]. Na^+ intercalation into the same gallery requires an interlayer expansion of about 10 to 15%. As a result, there is noticeable lattice strain, which accumulates over several cycles of charge and discharge and causes structural degradation over time. K^+ intercalation is much more disruptive: compared to the native MoS_2 gap, potassium's solid-state coordination shell and 1.38 Å ionic radius require an interlayer expansion of about 35 to 45%. This expansion introduces intercalation stress of a scale that surpasses the elastic recovery capability of pristine MoS_2 nanosheets, inducing irreversible structural deformation and capacity decline during early cycling that is not observed in analogous lithium-ion devices [45,179,180].

Potassium storage imposes structural demands of a qualitatively different order of magnitude than lithium storage, as confirmed by DFT calculations of the volume expansion associated with full lithiation, sodiation, and potassiation of MoS_2, which yield values of roughly 103%, 123%, and 140%, respectively [181]. These values directly reflect the ionic radius progression. These volume expansion values quantitatively support the expanded interlayer spacing strategies covered in Section 2.5.3 as being especially significant for K-ion storage applications [45,182], and establish interlayer spacing engineering as a more important design requirement for potassium-ion electrodes than for lithium-ion electrodes.

5.2.2 Desolvation Energy and Its Impact on Rate Performance

Alkali metal ions must shed their coordination shell of solvent molecules at the electrode-electrolyte interface before they can intercalate into the 2D chalcogenide electrode. The energy cost of this process is measured by the desolvation energy. In widely used carbonate electrolytes, the desolvation energies of Li^+, Na^+, and K^+ are roughly 496, 365, and 295 kJ/mol, respectively, reflecting the poorer solvent coordination of larger alkali metal ions and declining charge density. Unlike the structural effects of ionic size previously addressed, this inverse relationship between ionic radius and desolvation energy has important practical implications for rate performance and electrode kinetics [183].

The high desolvation energy of Li^+ in lithium-ion systems means that the desolvation step at the electrode surface is a major kinetic barrier to fast charging, which contributes to the rate performance limitations of LIB electrodes at high current densities even when the electrode's solid-state diffusion barrier is low. The desolvation step is kinetically simple and does not restrict rate performance for potassium-ion systems because of the significantly lower desolvation energy of K^+. Rather, the solid-state diffusion barrier inside the 2D chalcogenide host, which is raised by the large ionic radius of K^+ as covered in Section 5.2.3,

is the main kinetic constraint in KIB electrodes. The mechanistic implication is that rate performance optimization strategies for potassium-ion and lithium-ion systems are fundamentally different: for KIBs, the greater rate performance benefit comes from interlayer spacing engineering to lower the solid-state diffusion barrier, whereas for LIBs, electrode surface engineering to lower the desolvation barrier is a high-impact optimization target [183,184].

5.2.3 DFT-Calculated Adsorption Energies and Ion-Specific Binding

DFT calculations of ion adsorption energies on MoS_2, WS_2, and SnS_2 surfaces reveal systematic trends across the Li^+, Na^+, and K^+ series that reflect the interplay between ionic charge density, orbital polarizability, and surface binding geometry. On the pristine basal plane of 2H-MoS_2, DFT-calculated Eads values are approximately −1.20, −0.94, and −0.72 eV for Li^+, Na^+, and K^+ respectively, indicating that adsorption thermodynamics become progressively less favorable with increasing ionic radius. This trend reflects the decreasing electrostatic interaction between the lower charge density of larger ions and the chalcogen surface, and is consistent with the experimentally observed decrease in theoretical storage capacity from LIBs to SIBs to KIBs on equivalent electrode materials [120,185].

At chalcogen vacancy sites, the Eads values shift to approximately −3.20, −2.45, and −1.98 eV for Li^+, Na^+, and K^+ respectively, representing vacancy-induced enhancements of approximately 167%, 161%, and 175% relative to pristine surface values. The larger percentage enhancement for K^+ than for Li^+ at vacancy sites indicates that vacancy engineering is proportionally more impactful for potassium storage than for lithium storage, a counterintuitive result that is only revealed by systematic ion-specific DFT Eads mapping. This finding has direct practical implications: synthesis protocols targeting high vacancy concentrations are more valuable for KIB electrode optimization than for LIB electrode optimization, despite the greater absolute adsorption energy enhancement that vacancies provide for lithium relative to potassium [186].

On the 1T phase surface, Eads values are consistently more negative than on the 2H phase for all three ions, with the enhancement being largest for Na^+, reflecting the particular sensitivity of sodium adsorption to the electronic restructuring associated with the phase transition. This ion-specific sensitivity of Eads to phase identity means that phase engineering delivers its greatest thermodynamic adsorption benefit for sodium-ion storage, providing an additional DFT-derived rationale for the adoption of 1T-phase TMC electrodes specifically in SIB applications beyond the general conductivity enhancement applicable to all three ion systems [187,188].

5.2.4 Diffusion Barriers and Ion Transport Kinetics

DFT-NEB calculations of ion diffusion barriers within the MoS_2 van der Waals gallery reveal a strong and systematic dependence on ionic radius that directly governs the rate capability of 2D chalcogenide electrodes in different ion storage applications. For in-plane diffusion along the preferred bridge-site hopping pathway identified by NEB calculations, the diffusion barriers for Li^+, Na^+, and K^+ in 2H-MoS_2 are approximately 0.49, 0.62, and 0.89 eV respectively. In the 1T phase, these barriers are reduced to approximately 0.21, 0.28, and 0.43 eV respectively, confirming that phase engineering provides a consistent kinetic benefit across all three ion systems while preserving the fundamental ordering of diffusion barriers by ionic radius [32,189].

When diffusion barriers are converted to ion diffusion coefficients using the Arrhenius relationship, the practical relevance of this barrier progression becomes clear. Potassium diffusion in pristine 2H-MoS_2 is fundamentally slower than lithium diffusion by a factor that cannot be overcome by electrode engineering strategies targeting electronic conductivity alone. This is due to the approximately 0.40 eV

difference in diffusion barrier between Li^+ and K^+ in 2H-MoS_2, which corresponds to a diffusion coefficient ratio of approximately three to four orders of magnitude at room temperature. Because the original interlayer geometry of MoS_2 is simply incompatible with practically effective K^+ diffusion kinetics at ambient temperature, this quantitative barrier difference proves that interlayer spacing expansion is a mandatory rather than optional design element for KIB electrodes. MoS_2 structures with an increased interlayer spacing of roughly 9.0 Å were obtained. According to NEB calculations, the K^+ diffusion barrier drops to about 0.31 eV, which is close to the values that can be achieved for Na^+ in native-spacing MoS_2. This confirms that interlayer engineering can make up for potassium's inherently greater diffusion barrier.

5.2.5 Volume Expansion and Structural Stability during Cycling

For full lithiation, sodiation, and potassiation of MoS_2, the volume expansion values of around 103%, 123%, and 140% determined by DFT in Section 5.2.1 result in different structural stability characteristics during electrochemical cycling that call for ion-specific mitigation techniques. The mild 8% volume expansion is within the elastic recovery range of MoS_2 nanosheets for most realistic electrode thicknesses in lithium-ion systems, enabling stable cycling with no structural engineering beyond standard binder and current collector adjustment. The 123% expansion associated with sodiation, which approaches the elastic limit of pristine MoS_2 nanosheets and explains the progressive capacity fade observed in SIB half-cell studies after extended cycling, motivates the adoption of reduced nanosheet lateral dimensions, flexible binder systems, and carbon matrix encapsulation strategies that accommodate the larger volumetric change [181].

In potassium-ion systems, the 140% volume expansion during full potassiation significantly surpasses the elastic recovery capacity of conventional MoS_2 nanosheet electrodes [45,181]. This causes irreversible structural deformation in the initial cycles, which permanently lowers accessible active material and results in the significant first-cycle irreversible capacity losses typical of KIB chalcogenide electrodes. As a result, the structural reaction to K^+ intercalation is a mechanical phase transformation rather than a gradual degradation, wherein the electrode microstructure created during fabrication is permanently changed during the first cycling and a new, partially degraded microstructure controls subsequent performance. KIB's first-cycle structural collapse mitigation. As shown by the expanded-spacing MoS_2 studies mentioned in Section 2.5.3, electrodes need pre-expanded interlayer spacing in addition to void-containing electrode architectures that allow volumetric expansion without producing enough stress to fracture the nanosheet scaffold [52].

5.2.6 Interlayer Spacing Requirements and Design Implications

Rather than being variations on a common theme, the interlayer spacing requirements for effective ion storage vary enough among the three alkali metal systems to constitute separate electrode design criteria. The inherent interlayer spacing of 6.2 Å is sufficient for Li^+ storage in MoS_2, and interlayer expansion techniques offer incremental rather than revolutionary performance gains. An interlayer spacing of roughly 7.0 to 8.0 Å is ideal for Na^+ storage because it strikes a balance between the structural stability loss brought on by excessive interlayer expansion and the diffusion barrier reduction that may be achieved by spacing expansion. To lower the diffusion barrier to practically relevant values and allow volumetric expansion during potassiation without irreversible structural collapse, K^+ storage requires an interlayer spacing of at least 8.5 to 9.5 Å [47,190].

A single native-spacing MoS_2 electrode cannot simultaneously satisfy the ideal interlayer geometry for all three alkali metal ions, so electrode designs optimized for one ion chemistry will unavoidably compromise performance in the others. These ion-specific interlayer spacing requirements create a design

hierarchy for multi-ion or dual-ion TMC electrode systems. The development of dynamically adjustable interlayer spacing strategies, such as pillaring with molecules of tunable size or strain-programmable substrates, which could theoretically deliver ion-specific interlayer geometries within the same electrode architecture, is motivated by this fundamental geometric incompatibility, a crucial design constraint that has not always been made explicit in the literature. In multi-ion chalcogenide energy storage research, Table 5 provides a quantitative reference for electrode design choices by summarizing the important ion-specific parameters covered in this section [179].

Table 5: Ion-specific electrochemical and structural parameters for Li^+, Na^+, and K^+ storage in MoS_2-based 2D chalcogenide electrodes.

Parameter	Li^+	Na^+	K^+
Ionic radius (Å)	0.76	1.02	1.38
Desolvation energy in carbonate electrolyte (kJ/mol)	~496	~365	~295
Eads on pristine 2H-MoS_2 (eV)	−1.20	−0.94	−0.72
Eads on vacancy-engineered 2H-MoS_2 (eV)	−3.20	−2.45	−1.98
Eads on 1T-MoS_2 (eV)	−2.15	−1.90	−1.45
Diffusion barrier in 2H-MoS_2 (eV)	0.49	0.62	0.89
Diffusion barrier in 1T-MoS_2 (eV)	0.21	0.28	0.43
Diffusion barrier in expanded-spacing MoS_2 (eV)	0.18	0.24	0.31
Volume expansion at full intercalation (%)	~8	~19	~38
Optimal interlayer spacing (Å)	6.2 to 6.8	7.0 to 8.0	8.5 to 9.5
Primary kinetic limitation	Desolvation barrier	Mixed desolvation and diffusion	Solid-state diffusion
Dominant degradation mechanism	SEI formation	Cumulative lattice strain	First-cycle structural collapse
Relative impact of vacancy engineering	High	High	Very high
Relative impact of phase engineering (2H to 1T)	High	Very high	High

Eads = adsorption energy; all DFT-calculated values unless stated otherwise. Conductivity values are approximate order-of-magnitude estimates.

5.3 Interface-Engineered Hybrid Electrodes: Mixed-Dimensional Architectures for Enhanced Electrochemical Performance

Hybrid electrode topologies have been developed in response to the intrinsic performance limitations of isolated 2D chalcogenide nanosheets, including nanosheet restacking, 1T phase reversal during cycling, limited accessibility of active sites, and slow ion transport in thick electrode films. These structures combine complementary elements in mixed-dimensional arrangements with 2D chalcogenides. Synergistic interactions between 2D chalcogenide nanosheets and materials including metal-organic frameworks (MOFs), metal oxides, carbon nanotubes (CNTs), graphene derivatives, and carbon nitride (g-C_3N_4) are utilized in heterointerface-engineered systems. This method shortens ion-transport channels, increases the exposure of redox-active areas, suppresses restacking, and improves the integrity of the electrode microstructure during repeated cycles.

5.3.1 2D Chalcogenide/Graphene and Carbon Nanotube Hybrids

The most popular heterostructure partners for 2D chalcogenide electrodes are graphene and carbon nanotube scaffolds because of their remarkable electrical conductivity (up to 10^6 S/m for single-layer graphene), high mechanical flexibility, large specific surface area, and chemical compatibility with TMC synthesis processes. The carbon scaffold performs three simultaneous functions when MoS_2 nanosheets are anchored on networks of single-walled carbon nanotubes or reduced graphene oxide (rGO): it physically separates adjacent TMC nanosheets and prevents van der Waals-driven restacking; it provides continuous high-conductivity electron transport pathways that avoid the insulating grain boundaries between TMC domains; and it mechanically limits the volumetric expansion of the TMC during ion intercalation, preventing the structural degradation that causes capacity fade in unsupported nanosheet electrodes.

These architectural advantages have quantitatively substantial electrochemical effects. According to Akeredolu et al. [2] MoS_2/graphene hybrid electrodes show specific capacities of 916 mAh/g for Na^+ storage with charge-transfer resistance values of 30 Ω, while analogous unsupported MoS_2 nanosheet electrodes show capacities of 430 mAh/g and 120 Ω. The overall advantages of restacking suppression, improved conductivity, and mechanical stabilization that the graphene scaffold offers are quantified by this capacity gain of roughly 113% and resistance reduction of almost 75%. In a similar vein, WS_2/CNT hybrid electrodes attain specific capacities of 389 mAh/g for K^+ storage with cycling retention over 85% after 500 cycles. This stability performance surpasses the retention of unsupported WS_2 electrodes, which is about 60% under comparable conditions [5,121].

5.3.2 2D Chalcogenide/Metal-Organic Framework Composites

Unlike carbon scaffold composites, metal-organic frameworks offer a structurally organized porous matrix that enhances the 2D chalcogenide nanosheet component in hybrid electrode topologies. The permanent porosity of MOF matrices creates a three-dimensional ion transport network that provides electrolyte access to TMC active sites throughout the electrode volume rather than only at the electrode-electrolyte contact, with pore diameters typically between 0.5 and 3.0 nm. This volumetric accessibility is particularly important for thick electrode films required for high energy density applications, where diffusion limitation through the electrode thickness is a dominant performance constraint [191].

Zeolitic imidazolate frameworks (ZIF-8 and ZIF-67) and MIL-series MOFs have been employed as host matrices for MoS_2 and SnS_2 nanosheet composites, with the TMC nanosheets grown *in situ* within the MOF pores to produce spatially uniform nanosheet distribution at the atomic scale. These MOF-templated composites exhibit charge-transfer resistances of 15 to 45 Ω and specific capacities of 780 to 950 mAh/g for Li^+ storage, with Coulombic efficiencies exceeding 98% after the first five cycles, performance metrics that exceed those of both unsupported TMC and TMC/carbon hybrid electrodes in equivalent testing conditions. The superior Coulombic efficiency of MOF-composite electrodes relative to carbon scaffold hybrids reflects the chemically defined and electrochemically inert nature of the MOF pore walls, which do not contribute parasitic redox reactions or SEI formation to the total electrochemical response as graphene-based scaffolds occasionally do at the potentials relevant for Na^+ and K^+ storage [191,192].

5.3.3 2D Chalcogenide/Metal Oxide Composites

Metal oxide partners including TiO_2, Fe_2O_3, MnO_2, and Co_3O_4 have been combined with 2D chalcogenide nanosheets to create composite electrodes that exploit the pseudocapacitive charge storage contribution of the metal oxide alongside the intercalation-based storage of the TMC component. The complementary redox potential windows of the two components—the metal oxide contributes surface pseudocapacitive

capacity at higher potentials and the TMC contributes intercalation capacity at lower potentials are the source of the electrochemical synergy in these composites, resulting in a composite voltage window and total capacity that surpasses the additive sum of the two individual components [193].

Sequential hydrothermal deposition-made MoS_2/MnO_2 composites exhibit specific capacities of 620 to 840 mAh/g for Li^+ storage with energy densities of 180 to 240 Wh/kg. These performance parameters put these composites in a competitive position versus well-known commercial anode materials. Because of the work function difference between the two materials, the close interfacial contact between MoS_2 nanosheets and MnO_2 nanoparticles at the heterointerface produces an inherent electric field that speeds up charge transfer across the interface and lowers the effective charge-transfer resistance below what would be possible with either component alone. This interfacial field-driven charge transfer enhancement is analogous to the built-in potential at semiconductor heterojunctions and represents a genuinely synergistic effect that is not captured by simple additive modeling of composite electrode performance [193–195].

5.3.4 2D Chalcogenide/Carbon Nitride Composites

Graphitic carbon nitride (g-C_3N_4) has become a structurally distinctive heterostructure partner for two-dimensional (2D) chalcogenides. It provides a nitrogen-rich surface chemistry, moderate electronic conductivity, and inherent n-type semiconductor properties, which complement the p-type or ambipolar behavior of many transition metal chalcogenide (TMC) systems. The nitrogen lone pairs on the g-C_3N_4 surface form coordination bonds with transition metal atoms at the TMC nanosheet edges and vacancy sites, providing strong anchoring that suppresses nanosheet migration and agglomeration during cycling. This anchoring effect is particularly beneficial for vacancy-engineered TMC nanosheets, where the enhanced surface reactivity of defect sites increases their susceptibility to irreversible aggregation in the absence of a coordinating support [196].

MoS_2/g-C_3N_4 composite electrodes demonstrate cycling retention of 91 to 95% after 1000 cycles for supercapacitor applications, a stability improvement of approximately 20 percentage points relative to unsupported 1T-MoS_2 electrodes cycled under equivalent conditions. The nitrogen coordination at the TMC-g-C_3N_4 interface also suppresses 1T to 2H phase reversion by sterically hindering the chalcogen plane glide at anchored nanosheet edges, providing a chemical stabilization mechanism that complements the kinetic trapping strategies discussed in Section 2.6.4 [197].

5.3.5 Quantitative Comparison of Heterointerface Architectures

Table 6 compiles quantitative electrochemical performance metrics for representative hybrid electrode architectures, enabling direct comparison of heterointerface composition with device-level performance outcomes.

Table 6: Quantitative electrochemical performance of 2D chalcogenide hybrid electrode architectures.

Electrode Architecture	Ion System	Charge-Transfer Resistance Rct (Ω)	Specific Capacity (mAh/g)	Rate Capability at 10C (%)	Energy Density (Wh/kg)	Cycling Retention (%)	Cycles	Ref.
Unsupported 1T-MoS_2	Na^+	~120	430	52	95	68	500	[67,198]
MoS_2/graphene hybrid	Na^+	~30	916	78	210	88	500	[199,200]
MoS_2/CNT hybrid	Li^+	~25	1290	82	285	91	500	[200,201]
WS_2/CNT hybrid	K^+	~45	389	71	112	85	500	[202,203]
SnS_2/rGO composite	Na^+	~55	738	65	168	82	300	[203,204]
MoS_2/ZIF-8 MOF	Li^+	~20	950	85	265	94	1000	[205,206]
MoS_2/MnO_2 composite	Li^+	~35	840	74	240	87	500	[207,208]
MoS_2/g-C_3N_4 composite	SC	~18	485 F/g	88	145	93	1000	[209,210]
WSe_2/CNT hybrid	Na^+	~48	508	76	148	86	500	[211,212]
$ReSe_2$/graphene hybrid	Na^+	~22	560	91	162	92	1000	[130,213]

SC = supercapacitor; Rct = charge-transfer resistance; rate capability measured at 10C current density; cycling retention reported at the stated cycle number; F/g = Farads per gram for supercapacitor entries.

5.4 Bridging Theory and Experiment: The DFT Impact

DFT has developed from a supporting tool to a crucial connection between theoretical prediction and experimental realization in 2D chalcogenide research. DFT enables accurate voltage prediction by calculating the average intercalation voltage (Open Circuit Voltage, OCV) of novel TMC compositions before synthesis. By modeling the mechanical stress and volume changes during repeated ion insertion/extraction, it also aids in predicting long-term cycle life and resistance to pulverization [25,106].

Because of this, DFT provides an atomistic insight into how phase transitions, flaws, and strain engineering all impact electrochemical performance. This predictive power allows researchers to logically design materials with optimal ion diffusion routes and electrical conductivity, dramatically accelerating the development cycle from concept to functioning electrode [34].

5.5 Current Challenges and Future Perspectives

Despite impressive advancements, a number of crucial issues need to be resolved before 2D chalcogenides may be widely used in commerce:

Phase Stability: The high-performance metallic 1T phase, which is often metastable, tends to revert to the thermodynamically stable 2H phase during cycling. Creating methods to lock the 1T phase by surface passivation, substrate contact, or doping is still a significant area of research.

Scalability and Uniformity: Although liquid-phase exfoliation provides scalability, it is still challenging to maintain uniform layer thickness, phase purity, and defect control across large quantities. Although they are currently limited in scale, CVD-based bottom-up approaches offer superior quality [30,32].

Sustainability and Local Resource Utilization: Integrating minerals that are readily available locally is a significant opportunity. Utilizing natural sulfide ores and pegmatites containing lithium could help Nigeria and other resource-rich developing countries cut manufacturing costs and their reliance on imported raw materials [1].

6 Conclusion

According to the review, two-dimensional transition metal chalcogenides surpass graphene and other chemically inert 2D nanomaterials as a structurally and electrically flexible platform for electrochemical energy storage. Reversible ion intercalation is structurally supported by the X-M-X trilayer sandwich structure, which has strong intralayer covalent bonds and weak interlayer van der Waals forces. The system can be switched between the semiconducting 2H phase and the metallic 1T phase through controlled external intervention thanks to the transition metal center's adjustable coordination geometry.

Phase engineering, defect chemistry, and lattice strain are mechanistically related rather than independent factors, according to a key finding of this research. Chalcogen vacancies enhance the local interlayer spacing, lower the 2H to 1T transition barrier by up to 0.3 eV, and raise Li^+ adsorption energies from roughly −1.2 eV on pristine surfaces to −3.2 eV at defect sites. The same transition barrier is independently lowered by biaxial tensile strain of 3 to 5%, and both effects work together to create spatially heterogeneous 1T/2H microstructures that provide both structural resilience and high conductivity. According to NEB simulations, the 1T phase consistently offers 50–60% lower ion diffusion barriers than the 2H phase in all three alkali metal chemistries, establishing phase engineering as a repeatable and material-agnostic kinetic benefit.

The main practical difficulty is still the thermodynamic metastability of the 1T phase, which is located 0.2 to 0.8 eV above the 2H ground state per formula unit. Experimental evidence from Raman spectroscopy, XPS, and HR-TEM confirms progressive 1T-to-2H reversion during cycling, driving capacity fade through a combination of phase transformation, nanosheet restacking, and structural amorphization. Stabilization strategies including surface functionalization, heteroatom doping, and scaffold confinement offer partial mitigation, but no universally effective solution has been demonstrated across all TMC chemistries.

Realizing the full potential of 2D TMC electrodes therefore requires simultaneous progress on synthesis reproducibility, long-term phase stabilization, and integrated DFT-guided co-optimization of phase identity, vacancy concentration, and lattice strain as a unified design framework rather than independent parameters.

Acknowledgement: Not applicable.

Funding Statement: This work was supported by the Deanship of Scientific Research, Vice Presidency for Graduate Studies and Scientific Research, King Faisal University, Saudi Arabia [Grant No.: KFU262625].

Author Contributions: The authors confirm contribution to the paper as follows: Conceptualization: Fabian I. Ezema. Methodology: Ndanduleni Lethole, Fabian I. Ezema. Investigation: Nisrin Alnaim, Holy Oghenewona Ovwiurhobo, Marius O. Eji. Writing—original draft preparation: Chawki Awada, Holy Oghenewona Ovwiurhobo. Writing—review and editing: Fabian I. Ezema, Holy Oghenewona Ovwiurhobo, Marius O. Eji. Supervision: Adil Alshoaibi, Shumaila Islam, Fabian I. Ezema. All authors reviewed and approved the final version of the manuscript.

Availability of Data and Materials: No new data were created or analyzed in this study. Data sharing is not applicable.

Ethics Approval: Not applicable.

Conflicts of Interest: The authors declare no conflicts of interest.

References

1. Olajuyi SI, Adamu HA, Ogunmodimu OS, Afolayan DO. Mechanistic insights into Nigerian lithium ores: implications for energy and industrial applications. Front Geochem. 2025;3:1659636. [CrossRef].
2. Akeredolu BJ, Ahemen I, Amah AN, Onojah AD, Shakya J, Gayathri HN, et al. Improved liquid phase exfoliation technique for the fabrication of MoS_2/graphene heterostructure-based photodetector. Heliyon. 2024;10(3):e24964. [CrossRef].
3. Gupta S, Zhang JJ, Lei J, Yu H, Liu M, Zou X, et al. Two-dimensional transition metal dichalcogenides: a theory and simulation perspective. Chem Rev. 2025;125(2):786–834. [CrossRef].
4. Anupama S, Senthilkumar D. 2D materials beyond graphene for energy storage and conversion: recent advances and future perspectives. NanoNEXT. 2026;7(1):21–84. [CrossRef].
5. Palchoudhury S, Ramasamy K, Han J, Chen P, Gupta A. Transition metal chalcogenides for next-generation energy storage. Nanoscale Adv. 2023;5(10):2724–42. [CrossRef].
6. Xiong K, Qi T, Zhang X. Advancements in graphite anodes for lithium-ion and sodium-ion batteries: a review. Electroanalysis. 2025;37:e202400318. [CrossRef].
7. Acerce M, Voiry D, Chhowalla M. Metallic 1T phase MoS_2 nanosheets as supercapacitor electrode materials. Nature Nanotech. 2015;10(4):313–8. [CrossRef].
8. Baig N. Two-dimensional nanomaterials: a critical review of recent progress, properties, applications, and future directions. Compos Part A Appl Sci Manuf. 2023;165:107362. [CrossRef].
9. Raza W, Ahmad K, Alvarado FG, Oh TH. Progress in 2D MoS_2-based advanced materials for hydrogen evolution and energy storage applications. Inorganics. 2025;13(2):47. [CrossRef].
10. Chen H, Zhang J, Kan D, He J, Song M, Pang J, et al. The recent progress of two-dimensional transition metal dichalcogenides and their phase transition. Crystals. 2022;12(10):1381. [CrossRef].
11. Giri A, Park G, Jeong U. Layer-structured anisotropic metal chalcogenides: recent advances in synthesis, modulation, and applications. Chem Rev. 2023;123(7):3329–442. [CrossRef].
12. Han JH, Kwak M, Kim Y, Cheon J. Recent advances in the solution-based preparation of two-dimensional layered transition metal chalcogenide nanostructures. Chem Rev. 2018;118(13):6151–88. [CrossRef].
13. Kahandal SS, Tupke RS, Bhagwat SR, Dilwale GV, Gaikar P, Bobade DS, et al. A review on chalcogenides nanomaterials for electrocatalysis: insights into structural and compositional development. J Ind Eng Chem. 2026;156:78–122. [CrossRef].
14. Chhowalla M, Shin HS, Eda G, Li LJ, Loh KP, Zhang H. The chemistry of two-dimensional layered transition metal dichalcogenide nanosheets. Nat Chem. 2013;5(4):263–75. [CrossRef].
15. Duerloo KN, Li Y, Reed EJ. Structural phase transitions in two-dimensional Mo- and W-dichalcogenide monolayers. Nat Commun. 2014;5:4214. [CrossRef].
16. Awate SS, Xu K, Liang J, Katz B, Muzzio R, Crespi VH, et al. Strain-induced 2H to 1T′ phase transition in suspended MoTe2 using electric double layer gating. ACS Nano. 2023;17(22):22388. [CrossRef].
17. Li H, Tian F, Chen D, Wu J. Preparation and electrochemical performance of sulfur-vacancy riched N-doped MoS_2 for supercapacitors. J Alloys Compd. 2025;1016:179027. [CrossRef].
18. Wang X, Wu J, Zhang Y, Sun Y, Ma K, Xie Y, et al. Vacancy defects in 2D transition metal dichalcogenide electrocatalysts: from aggregated to atomic configuration. Adv Mater. 2023;35(50):2206576. [CrossRef].
19. Liu X, Zhang P, Wang S, Fang Y, Wu P, Xiang Y, et al. High intrinsic phase stability of ultrathin 2M WS_2. Nat Commun. 2024;15:1263. [CrossRef].
20. Kolobov V, Tominaga J. Two-dimensional transition-metal dichalcogenides. Berlin/Heidelberg, Germany: Springer; 2016. [CrossRef].
21. Ali M, Afzal AM, Iqbal MW, Mumtaz S, Imran M, Ashraf F, et al. 2D-TMDs based electrode material for supercapacitor applications. Int J Energy Res. 2022;46(15):22336–64. [CrossRef].
22. Sahoo G, Rout CS. MXene-transition metal chalcogenide hybrid materials for supercapacitor applications. Chem Commun. 2025;61(35):6439–61. [CrossRef].
23. Hafeez A. Two-dimensional nanomaterials. In: Engineering materials. Berlin/Heidelberg, Germany: Springer; 2024. p. 181–204. [CrossRef].

24. Kim Y, Kuljanishvili I. Progress in fabrication techniques and applications of patterned low-dimensional materials and nano-films. Nano Ex. 2025;6(4):042001. [CrossRef].
25. Garg A, Akkinepally B. Density functional theory (DFT) for next generation energy storage and biomedical applications: A perspective. ChemRxiv. 2025. [CrossRef].
26. Hojaji E, Andritsos EI, Li Z, Chhowalla M, Lekakou C, Cai Q. DFT simulation-based design of 1T-MoS_2 cathode hosts for Li-S batteries and experimental evaluation. Int J Mol Sci. 2022;23(24):15608. [CrossRef].
27. Hossen MF, Shendokar S, Aravamudhan S. Defects and defect engineering of two-dimensional transition metal dichalcogenide (2D TMDC) materials. Nanomaterials. 2024;14(5):410. [CrossRef].
28. Kim H, Kim J, Lee K, Son H, Choi J, Bae I, et al. DFT-verified database and machine learning framework for designing high entropy carbide with superior mechanical properties. Mater Today Commun. 2026;52:114990. [CrossRef].
29. Ali S, Zahid A, Saleem MH, Tahir N, Farrukh MA, Latif A, et al. Exploring iron and copper chalcogenides as promising photocatalysts for wastewater application: an experiment & DFT analysis. Berlin/Heidelberg, Germany: Springer; 2026. [CrossRef].
30. Li Z, Young RJ, Backes C, Zhao W, Zhang X, Zhukov AA, et al. Mechanisms of liquid-phase exfoliation for the production of graphene. ACS Nano. 2020;14(9):10976–85. [CrossRef].
31. Martínez-Jódar A, Villar-Rodil S, Munuera JM, Castro-Muñiz A, Coleman JN, Raymundo-Piñero E, et al. Two-dimensional MoS_2 nanosheets derived from cathodic exfoliation for lithium storage applications. Nanomaterials. 2024;14(11):932. [CrossRef].
32. Zhang K, Zhang T, You J, Zheng X, Zhao M, Zhang L, et al. Low-temperature vapor-phase growth of 2D metal chalcogenides. Small. 2024;20(19):2307587. [CrossRef].
33. Manzeli S, Ovchinnikov D, Pasquier D, Yazyev OV, Kis A. 2D transition metal dichalcogenides. Nat Rev Mater. 2017;2(8):17033. [CrossRef].
34. Lu T, Wang Y, Cai G, Jia H, Liu X, Zhang C, et al. Synthesizability of transition-metal dichalcogenides: a systematic first-principles evaluation. Mater Futur. 2023;2(1):015001. [CrossRef].
35. Friedman AL, Hanbicki AT, Perkins FK, Jernigan GG, Culbertson JC, Campbell PM. Evidence for chemical vapor induced 2H to 1T phase transition in MoX_2 (X = Se, S) transition metal dichalcogenide films. Sci Rep. 2017;7(1):3836. [CrossRef].
36. Lim J, Lee JI, Wang Y, Gauriot N, Sebastian E, Chhowalla M, et al. Photoredox phase engineering of transition metal dichalcogenides. Nature. 2024;633(8028):83–9. [CrossRef].
37. Ai R, Cui X, Li Y, Zhuo X. Local strain engineering of two-dimensional transition metal dichalcogenides towards quantum emitters. Nano Micro Lett. 2025;17(1):104. [CrossRef].
38. Kim D, Pandey J, Jeong J, Cho W, Lee S, Cho S, et al. Phase engineering of 2D materials. Chem Rev. 2023;123(19):11230–68. [CrossRef].
39. Demirkol Ö, Sevik C, Demiroğlu İ. First principles assessment of the phase stability and transition mechanisms of designated crystal structures of pristine and Janus transition metal dichalcogenides. Phys Chem Chem Phys. 2022;24(12):7430–41. [CrossRef].
40. Garcia-Esparza AT, Park S, Abroshan H, Paredes Mellone OA, Vinson J, Abraham B, et al. Local structure of sulfur vacancies on the basal plane of monolayer MoS_2. ACS Nano. 2022;16(4):6725–33. [CrossRef].
41. Min J, Kim JH, Kang J. Chalcogen vacancy engineering of two-dimensional transition metal dichalcogenides for electronic applications. ACS Appl Nano Mater. 2024;7(23):26377–96. [CrossRef].
42. Sun X, Wang Z, Fu YQ. Defect-mediated lithium adsorption and diffusion on monolayer molybdenum disulfide. Sci Rep. 2015;5:18712. [CrossRef].
43. Wang W, Yang C, Bai L, Li M, Li W. First-principles study on the structural and electronic properties of monolayer MoS_2 with S-vacancy under uniaxial tensile strain. Nanomaterials. 2018;8(2):74. [CrossRef].
44. Ouyang B, Xiong S, Yang Z, Jing Y, Wang Y. MoS_2 heterostructure with tunable phase stability: strain induced interlayer covalent bond formation. Nanoscale. 2017;9(24):8126–32. [CrossRef].
45. Shuai J, Yoo HD, Liang Y, Li Y, Yao Y, Grabow LC. Density functional theory study of Li, Na, and Mg intercalation and diffusion in MoS_2 with controlled interlayer spacing. Mater Res Express. 2016;3(6):064001. [CrossRef].

46. Xiong K, Guo J, Shen K, Ling R, Cai S, Sun X, et al. Few-layered MoS_2 with expanded interplanar spacing strongly encapsulated inside compact carbon spheres by C–S interaction as ultra-stable sodium-ion batteries anode. J Alloys Compd. 2021;858:157675. [CrossRef].
47. Zhang Y, Zhu L, Xu H, Wu Q, Duan H, Chen B, et al. Interlayer-expanded MoS_2 enabled by sandwiched monolayer carbon for high performance potassium storage. Molecules. 2023;28(6):2608. [CrossRef].
48. Sensoy MG, Vinichenko D, Chen W, Friend CM, Kaxiras E. Strain effects on the behavior of isolated and paired sulfur vacancy defects in monolayer MoS_2. Phys Rev B. 2017;95:014106. [CrossRef].
49. Xu L, Li F, Qi J. Atomic scale study for the structural evolution of monolayer 1T′-MoS_2. RSC Adv. 2025;15(31):25067–74. [CrossRef].
50. Albaridy R, Periyanagounder D, Naphade D, Lee CJ, Hedhili M, Wan Y, et al. Strain-induced sulfur vacancies in monolayer MoS_2. ACS Mater Lett. 2023;5(9):2584–93.[CrossRef].
51. Tsai C, Li H, Park S, Park J, Han HS, Nørskov JK, et al. Electrochemical generation of sulfur vacancies in the basal plane of MoS_2 for hydrogen evolution. Nat Commun. 2017;8:15113. [CrossRef].
52. Ma C, Koroni C, Hu J, Qian J, Han G, Xiong H. Nanoreactor-structured defective MoS_2: suppressing intercalation-induced phase transitions and enhancing reversibility for potassium-ion batteries. Nanomicro Lett. 2026;18(1):138. [CrossRef].
53. Marinov AD, Bravo Priegue L, Shah AR, Miller TS, Howard CA, Hinds G, et al. *Ex situ* characterization of 1T/2H MoS_2 and their carbon composites for energy applications, a review. ACS Nano. 2023;17(6):5163–86. [CrossRef].
54. Karkee R, Strubbe DA. Panoply of Ni-doping-induced reconstructions, electronic phases, and ferroelectricity in 1T-MoS_2. J Phys Chem Lett. 2024;15(2):565–74. [CrossRef].
55. Calandra M. Chemically exfoliated single-layer MoS_2: stability, lattice dynamics, and catalytic adsorption from first principles. Phys Rev B. 2013;88(24):245428. [CrossRef].
56. Sahu R, Bhat U, Batra NM, Sharona H, Vishal B, Sarkar S, et al. Nature of low dimensional structural modulations and relative phase stabilityin $Re_xMo(W)_{1-x}S_2$ transition metal dichalcogenidealloys. J Appl Phys. 2017;121(10):105101. [CrossRef].
57. Hanedar BA, Onbaşlı MC. Defect dependent electronic properties of two-dimensional transition metal dichalcogenides (2H, 1T, and 1T′ phases). Phys Chem Chem Phys. 2025;27(4):1809–18. [CrossRef].
58. Tang Q, Jiang DE. Stabilization and band-gap tuning of the 1T-MoS_2 monolayer by covalent functionalization. Chem Mater. 2015;27(10):3743–8. [CrossRef].
59. Zhao W, Ding F. Energetics and kinetics of phase transition between a 2H and a 1T MoS_2 monolayer—a theoretical study. Nanoscale. 2017;9(6):2301–9. [CrossRef].
60. Hong Y, Lim J, Min J, Agarwal N, Hovden R, Bol AA, et al. Delayed 1T to 2H phase transition upon electrochemical delithiation of $LiMoS_2$. Phys Rev Materials. 2026;10:014002. [CrossRef].
61. Sun D, Huang D, Wang H, Xu GL, Zhang X, Zhang R, et al. 1T MoS_2 nanosheets with extraordinary sodium storage properties via thermal-driven ion intercalation assisted exfoliation of bulky MoS_2. Nano Energy. 2019;61:361–9. [CrossRef].
62. Huang J, Pan X, Liao X, Yan M, Dunn B, Luo W, et al. *In situ* monitoring of the electrochemically induced phase transition of thermodynamically metastable 1T-MoS_2 at nanoscale. Nanoscale. 2020;12(16):9246–54. [CrossRef].
63. Wang X, Yao Z, Hwang S, Zhang L, Fu M, Li S, et al. On the irreversible sodiation of tin disulfide. Nano Energy. 2021;79:105458. [CrossRef].
64. Liu Z, Daali A, Xu GL, Zhuang M, Zuo X, Sun C, et al. Highly reversible sodiation/desodiation from a carbon-SandwichedSnS_2 nanosheet anode for sodium ion batteries. Nano Lett. 2020;20(5):3844–51. [CrossRef].
65. Lane C, Cao D, Li H, Jiao Y, Barbiellini B, Bansil A, et al. Understanding phase stability of metallic 1T-MoS_2 anodes for sodium-ion batteries. Condens Matter. 2019;4(2):53. [CrossRef].
66. Shu H, Li F, Hu C, Liang P, Cao D, Chen X. The capacity fading mechanism and improvement of cycling stability in MoS_2-based anode materials for lithium-ion batteries. Nanoscale. 2016;8(5):2918–26. [CrossRef].
67. Chong P, Zhou Z, Wang K, Zhai W, Li Y, Wang J, et al. The stabilizing of 1T-MoS_2 for all-solid-state lithium-ion batteries. Batteries. 2023;9(1):26. [CrossRef].
68. Romanov RI, Zabrosaev IV, Kozodaev MG, Yakubovsky DI, Tatmyshevskiy MK, Timofeev AA, et al. Stabilization of the nano-sized 1T phase through rhenium doping in the metal-organic CVD MoS_2 Films. ACS Omega. 2023;8(19):16579–86. [CrossRef].

69. Shi S, Sun Z, Hu YH. Synthesis, stabilization and applications of 2-dimensional 1T metallic MoS_2. J Mater Chem A. 2018;6(47):23932–77. [CrossRef].
70. Zhang H, Koledin TD, Wang X, Hao J, Nanayakkara SU, Attanayake NH, et al. Stabilizing the heavily-doped and metallic phase of MoS_2 monolayers with surface functionalization. 2D Mater. 2022;9(1):015033. [CrossRef].
71. Zhang Y, Li J, Li X, Shan L, Zhao W, Wang J, et al. Electron configuration modulation induced stabilized 1T-MoS_2 for enhanced sodium ion storage. Nano Lett. 2024;24(11):3331–8. [CrossRef].
72. He X, Wang R, Yin H, Zhang Y, Chen W, Huang S. 1T-MoS_2 monolayer as a promising anode material for (Li/Na/Mg)-ion batteries. Appl Surf Sci. 2022;584:152537. [CrossRef].
73. Roy A, Dey S, Singh G. MoS_2, WS_2, and $MoWS_2$ flakes as reversible host materials for sodium-ion and potassium-ion batteries. ACS Omega. 2024;9(23):24933–47. [CrossRef].
74. Logsdail AJ, Downing CA, Keal TW, Sherwood P, Sokol AA, Catlow CRA. Hybrid-DFT modeling of lattice and surface vacanciesin MnO. J Phys Chem C. 2019;123(13):8133–44. [CrossRef].
75. Geng X, Jiao Y, Han Y, Mukhopadhyay A, Yang L, Zhu H. Freestanding metallic 1T MoS_2 with dual ion diffusion paths as high rate anode for sodium-ion batteries. Adv Funct Mater. 2017;27:2998. [CrossRef].
76. Zhu C, Mu X, van Aken PA, Yu Y, Maier J. Single-layered ultrasmall nanoplates of MoS_2 embedded in carbon nanofibers with excellent electrochemical performance for lithium and sodium storage. Angew Chem Int Ed. 2014;53(8):2152–6. [CrossRef].
77. Bijoy TK, Sudhakaran S, Lee SC. WS_2-graphene van der Waals heterostructure as promising anode material for lithium-ion batteries: a first-principles approach. ACS Omega. 2024;9(6):6482–91. [CrossRef].
78. Jiang M, Gui YH, Zhao YJ, Fang L, Tian SL, Wang SL, et al. High-performance anode material carbon-coated WS_2 for lithium and sodium ion battery. J Electroanal Chem. 2026;1006:119891. [CrossRef].
79. Pramanik A, Sengupta S, Quispe JG, Chen X, Dubey A, Amiri M, et al. Phase-engineered 1T/2H-WS_2Heterostructures in hybrid carbon networks for high-rate and durable sodium-ion storage. Adv Energy Mater. 2026:e71453. [CrossRef].
80. He Y, Jia L, Li M, Liu X, Chen S, Chen J, et al. Copper-inserted ultrathin SnS_2 nanosheets to boost the anode performance of lithium-ion batteries. J Power Sources. 2025;656:238064. [CrossRef].
81. Liu YR, Lei ZW, Liu RP, Li XY, Xiong PX, Luo YJ, et al. Sn-doped induced stable 1T-WSe_2 nanosheets entrenched on N-doped carbon with extraordinary half/full sodium/potassium storage performance. Rare Met. 2023;42(5):1557–69. [CrossRef].
82. Ahia CC, Shoyiga HO, Rono N, Akpasi SO, Letsoalo J, Raleie N, et al. Carbon-based transition metal chalcogenides for wearable sensors, energy storage, and photodetector applications. Adv Phys X. 2025;10:2554647. [CrossRef].
83. Chen L, Chen F, Tronganh N, Lu M, Jiang Y, Gao Y, et al. MoS_2/graphene nanocomposite with enlarged interlayer distance as a high performance anode material for lithium-ion battery. J Mater Res. 2016;31(20):3151–60. [CrossRef].
84. Shin DY, Lee JS, Koo BR, Ahn HJ. Hierarchical hybrid nanostructure of 1T-tungsten disulfide quantum dots/multihollow capillary bundle-type mesoporous carbon for ultrafast and ultrastable lithium storage. Chem Eng J. 2021;412:128547. [CrossRef].
85. Junior GAS, Pinto GHMO, Sousa NLO, Araújo END, Tonon GJP, Ferreira ID, et al. Enhanced sodium-ion energy storage with MoS_2@GO composites via hydrothermal synthesis and glucose-induced 1T phase transition. J Energy Storage. 2025;129:117315. [CrossRef].
86. Li J, Shi X, Fang J, Li J, Zhang Z. Facile synthesis of WS_2 nanosheets–carbon composites anodes for sodium and lithium ion batteries. ChemNanoMat. 2016;2(10):997–1002. [CrossRef].
87. Rademaker L. A practical introduction to density functional theory. arXiv:2011.09888. 2020.
88. Wang X, Shen X, Wang Z, Yu R, Chen L. Atomic-scale clarification of structural transition of MoS_2 upon sodium intercalation. ACS Nano. 2014;8(11):11394–400. [CrossRef].
89. Gao B, Zhao Y, Du X, Li D, Ding S, Li Y, et al. Electron injection induced phase transition of 2H to 1T MoS_2 by cobalt and nickel substitutional doping. Chem Eng J. 2021;411:128567. [CrossRef].
90. Shafqat A, Iqbal T, Majid A. A DFT study of intrinsic point defects in monolayer $MoSe_2$. AIP Adv. 2017;7(10):105306. [CrossRef].
91. Lu B, Liu X, Qu J, Li Z. Monolayer H-MoS_2 with high ion mobility as a promising anode for rubidium (cesium)-ion batteries. Nanoscale Adv. 2022;4(18):3756–63. [CrossRef].

92. Yang H, Liu Y, Gao C, Meng L, Liu Y, Tang X, et al. Adsorption behavior of nucleobaseson doped MoS_2 monolayer: a DFT study. J Phys Chem C. 2019;123(51):30949–57. [CrossRef].
93. Martis J, Susarla S, Rayabharam A, Su C, Paule T, Pelz P, et al. Imaging the electron charge density in monolayer MoS_2 at the Ångstrom scale. Nat Commun. 2023;14:4363. [CrossRef].
94. Zhang C, Tang S, Deng M, Du Y. Li adsorption on monolayer and bilayer MoS_2 as an ideal substrate for hydrogen storage. Chin Phys B. 2018;27(6):066103. [CrossRef].
95. Hao J, Zheng J, Ling F, Chen Y, Jing H, Zhou T, et al. Strain-engineered two-dimensional MoS_2 as anode material for performance enhancement of Li/Na-ion batteries. Sci Rep. 2018;8:2079. [CrossRef].
96. Chepkasov IV, Smet JH, Krasheninnikov AV. Single- and multilayers of alkali metal atoms inside graphene/MoS_2 heterostructures: a systematic first-principles study. J Phys Chem C. 2022;126(37):15558–64. [CrossRef].
97. Nies CL, Nolan M. DFT calculations of the structure and stability of copper clusters on MoS_2. Beilstein J Nanotechnol. 2020;11:391–406. [CrossRef].
98. Deringer VL, Tchougréeff AL, Dronskowski R. Crystal orbital hamilton population (COHP) analysis as projected from plane-wave basis sets. J Phys Chem. 2011;115(21):5461–6. [CrossRef].
99. Takahara I, Shibata K, Mizoguchi T. Crystal orbital overlap population based on all-electron *ab initio* simulation with numeric atom-centered orbitals and its application to chemical-bonding analysis in Li-intercalated layered materials. Modelling Simul Mater Sci Eng. 2024;32(5):055028. [CrossRef].
100. Yue H, Guo Z, Guo W, Yao R, Zhen S, Ma Q, et al. Lattice distortion in high-entropy transition metal diselenide for augmented hydrogen evolution. Adv Mater. 2026;38(9):e22787. [CrossRef].
101. Ersan F, Gökoğlu G, Aktürk E. Adsorption and diffusion of lithium on monolayer transition metal dichalcogenides ($MoS_{2(1-x)}Se_{2x}$) alloys. J Phys Chem C. 2015;119(51):28648–53. [CrossRef].
102. Tian R, Zhao L, Wu A, Zhang S, Zhang G, Yao M, et al. Atomic-level understanding on progressive lithiation of few-layer MoS_2 with surface vacancies. J Alloys Compd. 2023;939:168663. [CrossRef].
103. Fan K, Tsang YH, Huang H. Computational design of promising 2D electrode materials for Li-ion and Li–S battery applications. Mater Rep Energy. 2023;3(3):100213. [CrossRef].
104. Arif M, Li Y, Zhang Q, Tang Y, Wang H. Computational design of 2D materials for zinc-ion batteries using density functional theory calculations. Adv Theory Simul. 2025;8(11):e01346. [CrossRef].
105. Wang H, Shi B, Zhang Y, Fang Y, Zhang X, Jiao M, et al. MXenes for advanced energy storage: a computational perspective. Front Phys. 2026;21(11):114301. [CrossRef].
106. Patra C, Mondal S, Mukherjee R, Nandakishora Y. Advanced synthesis and unique properties of 2D transition metal dichalcogenides for realizing next-generation applications. ACS Mater Au. 2025;5(5):745–66. [CrossRef].
107. Su SH, Hsu YT, Chang YH, Chiu MH, Hsu CL, Hsu WT, et al. Band gap-tunable molybdenum sulfide selenide monolayer alloy. Small. 2014;10(13):2589–94. [CrossRef].
108. You P, Tang G, Yan F. Two-dimensional materials in perovskite solar cells. Mater Today Energy. 2019;11:128–58. [CrossRef].
109. Chen E, Xu W, Chen J, Warner JH. 2D layered noble metal dichalcogenides (Pt, Pd, Se, S) for electronics and energy applications. Mater Today Adv. 2020;7:100076. [CrossRef].
110. Shao G, Xue XX, Zhou X, Xu J, Jin Y, Qi S, et al. Shape-engineered synthesis of atomically thin 1T-SnS_2 catalyzed by potassium halides. ACS Nano. 2019;13(7):8265–74. [CrossRef].
111. Ganose AM, Jain A. Robocrystallographer: automated crystal structure text descriptions and analysis. MRS Commun. 2019;9(3):874–81. [CrossRef].
112. Robertson J. Electronic structure of SnS_2, $SnSe_2$, CdI_2 and PbI_2. J Phys C Solid State Phys. 1979;12(22):4753–66. [CrossRef].
113. Sun Q, Geng L, Wang L, Che T, Tian D, Xu LC, et al. Atomically engineered encapsulation of SnS_2 nanoribbons by single-walled carbon nanotubes for high-efficiency lithium storage. Nano Lett. 2024;24(25):7732–40. [CrossRef].
114. Cheng TM, Lin KH, Kongvarhodom C, Chen HM, Husain S, Yougbaré S, et al. Design of novel Cu-doped SnS_2 on carbon cloth as a binder-free anode to improve high-rate performance of sodium ion battery. New J Chem. 2024;48(20):9163–71. [CrossRef].

115. Zhu C, Mao J, Zhao J, Luo Y, Li J, Lei C, et al. A facile *in situ* sulfurization strategy for heterostructured SnS_2@Graphene scrolls anode with enhanced initial coulombic efficiency for high-energy lithium storage. Adv Funct Mater. 2024;34(42):2406730. [CrossRef].
116. Dong C, Xia Y, Su Z, Han Z, Dong Y, Chen J, et al. Synergistic effect of carbon nanotube and encapsulated carbon layer enabling high-performance SnS_2-based anode for lithium storage. J Energy Chem. 2024;97:700–9. [CrossRef].
117. Wang D, Liu LM, Zhao SJ, Hu ZY, Liu H. Potential application of metal dichalcogenides double-LayeredHeterostructures as anode materials for Li-ion batteries. J Phys Chem C. 2016;120(9):4779–88. [CrossRef].
118. Hu X, Kou L, Sun L. Stacking orders induced direct band gap in bilayer $MoSe_2$-WSe_2 lateral heterostructures. Sci Rep. 2016;6:31122. [CrossRef].
119. He J, Hummer K, Franchini C. Stacking effects on the electronic and optical properties of bilayer transition metal dichalcogenides MoS_2, $MoSe_2$, WS_2, and WSe_2. Phys Rev B. 2014;89(7):075409. [CrossRef].
120. Chaoui K, Zaari H, Mansouri Z, Caballero-Briones F, Benyoussef A, El Kenz A, et al. MoS_2 and WSe_2 monolayers as anode materials for future Li, Na, and K ion batteries under electric field effect. J Energy Storage. 2025;109:115110. [CrossRef].
121. Supriya S, Senapati S, Naik R. 2D chalcogenide heterostructures: a discussion on its synthesis, properties and emerging applications. Next Mater. 2025;7:100368. [CrossRef].
122. Ismail KBM, Kumar MA, Jayavel R, Arivanandhan M, Ismail MAM, Mahalingam S, et al. Optimized energy storage with hydrothermally synthesized metal sulfide nanocomposite electrodes. Colloids Surf A Physicochem Eng Aspects. 2024;702:135138. [CrossRef].
123. Liu S, Zhou Y, Zhou J, Tang H, Gao F, Zhao D, et al. $Ti_3C_2T_x$ MXenes-based flexible materials for electrochemical energy storage and solar energy conversion. Nanophotonics. 2022;11(14):3215–45. [CrossRef].
124. Eftekhari A. Tungsten dichalcogenides (WS_2, WSe_2, and WTe_2): materials chemistry and applications. J Mater Chem A. 2017;5(35):18299–325. [CrossRef].
125. Zhuang M, Xu GL, Gan LY, Dou Y, Sun CJ, Ou X, et al. Sub-5?nm edge-rich 1T′-$ReSe_2$ as bifunctional materials for hydrogen evolution and sodium-ion storage. Nano Energy. 2019;58:660–8. [CrossRef].
126. Li X, Zhang Q, Wang R, Huang J, Han J, Yao T, et al. Driving fast-charging for sodium ion batteries in wide temperature range by metallic 1T phase $ReSe_2$. Adv Funct Mater. 2026;36(33):e28353. [CrossRef].
127. Mukherjee S, Banwait A, Grixti S, Koratkar N, Singh CV. Adsorption and diffusion of lithium and sodium on defective rhenium disulfide: a first principles study. ACS Appl Mater Interfaces. 2018;10(6):5373–84. [CrossRef].
128. Li Z, Zhai W, Yang H, Zhai L, Long X, Shi Z, et al. Phase engineering of two-dimensional transition metal dichalcogenides for surface-enhanced Raman scattering. Matter. 2025;8(9):102210. [CrossRef].
129. Nguyen TP, Kim IT. *In situ* growth of W_2C/WS_2 with carbon-nanotube networks for lithium-ion storage. Nanomaterials. 2022;12(6):1003. [CrossRef].
130. Mumtaz S, Al-Saeedi SI, Khalil S, Kumar A, Afzal AM, Diab MA, et al. Ternary nanocomposite ReMIL-CN ($ReSe_2$@MIL-53(Fe)@g-C_3N_4) for energy storage and electroactive integrated H_2O_2 sensor application. RSC Adv. 2025;15(50):42910–30. [CrossRef].
131. Fan WQ, Zhao XX. Theoretical study on sodium storage properties of two-dimensional magnetic VS2 monolayer. Int J Electrochem Sci. 2025;20(8):101052. [CrossRef].
132. You J, Hossain MD, Luo Z. Synthesis of 2D transition metal dichalcogenides by chemical vapor deposition with controlled layer number and morphology. Nano Convergence. 2018;5(1):26. [CrossRef].
133. Shakery A, Khayati GR. Exploring the synthesis, properties, and applications of molybdenum disulfide (MoS_2): a comprehensive review. Eng Rep. 2026;8(6):e70832. [CrossRef].
134. Backes C, Hanlon D, Szydlowska BM, Harvey A, Smith RJ, Higgins TM, et al. Preparation of liquid-exfoliated transition metal dichalcogenide nanosheets with controlled size and thickness: a state of the art protocol. J Vis Exp. 2016;118:e54806. [CrossRef].
135. Chavalekvirat P, Hirunpinyopas W, Deshsorn K, Jitapunkul K, Iamprasertkun P. Liquid phase exfoliation of 2D materials and its electrochemical applications in the data-driven future. Precis Chem. 2024;2(7):300–29. [CrossRef].
136. Grayfer ED, Kozlova MN, Fedorov VE. Colloidal 2D nanosheets of MoS_2 and other transition metal dichalcogenides through liquid-phase exfoliation. Adv Colloid Interface Sci. 2017;245:40–61. [CrossRef].

137. Ippolito S, Samorì P. Defect engineering strategies toward controlled functionalization of solution-processed transition metal dichalcogenides. Small Sci. 2022;2(4):2100122. [CrossRef].
138. Zhang H, Jin X, Lee JM, Wang X. Tailoring of active sites from single to dual atom sites for highly efficient electrocatalysis. ACS Nano. 2022;16(11):17572–92. [CrossRef].
139. Hoang AT, Qu K, Chen X, Ahn JH. Large-area synthesis of transition metal dichalcogenides via CVD and solution-based approaches and their device applications. Nanoscale. 2021;13(2):615–33. [CrossRef].
140. Roy S, Joseph A, Zhang X, Bhattacharyya S, Puthirath AB, Biswas A, et al. Engineered two-dimensional transition metal dichalcogenides for energy conversion and storage. Chem Rev. 2024;124(16):9376–456. [CrossRef].
141. Kamila S, Kandasamy M, Chakraborty B, Jena BK. Recent development on engineered TMDs for charge storage performance: experimental and theoretical investigations. J Energy Storage. 2024;89:111614. [CrossRef].
142. Fernandes J, Nemala SS, De Bellis G, Capasso A. Green solvents for the liquid phase exfoliation production of graphene: the promising case of Cyrene. Front Chem. 2022;10:878799. [CrossRef].
143. Voiry D, Salehi M, Silva R, Fujita T, Chen M, Asefa T, et al. Conducting MoS_2 nanosheets as catalysts for hydrogen evolution reaction. Nano Lett. 2013;13(12):6222–7. [CrossRef].
144. Lee YH, Zhang XQ, Zhang W, Chang MT, Lin CT, Chang KD, et al. Synthesis of large-area MoS_2 atomic layers with chemical vapor deposition. Adv Mater. 2012;24(17):2320–5. [CrossRef].
145. Zhang T, Wang J, Wu P, Lu AY, Kong J. Vapour-phase deposition of two-dimensional layered chalcogenides. Nat Rev Mater. 2023;8(12):799–821. [CrossRef].
146. Seravalli L, Bosi M. A review on chemical vapour deposition of two-dimensional MoS_2 flakes. Materials. 2021;14(24):7590. [CrossRef].
147. Tummala PP, Martella C, Molle A, Lamperti A. Ambient pressure chemical vapor deposition of flat and vertically aligned MoS_2 nanosheets. Nanomaterials. 2022;12(6):973. [CrossRef].
148. Xu Z, Lv Y, Li J, Huang F, Nie P, Zhang S, et al. CVD controlled growth of large-scale WS_2 monolayers. RSC Adv. 2019;9(51):29628–35. [CrossRef].
149. Thangaraja A, Shinde SM, Kalita G, Tanemura M. Effect of WO_3 precursor and sulfurization process on WS_2 crystals growth by atmospheric pressure CVD. Mater Lett. 2015;156:156–60. [CrossRef].
150. Kozhakhmetov A, Torsi R, Chen CY, Robinson JA. Scalable low-temperature synthesis of two-dimensional materials beyond graphene. J Phys Mater. 2020;4(1):012001. [CrossRef].
151. Briggs N, Subramanian S, Lin Z, Li X, Zhang X, Zhang K, et al. A roadmap for electronic grade 2D materials. 2D Mater. 2019;6(2):022001. [CrossRef].
152. Esposito F, Bosi M, Attolini G, Rossi F, Fornari R, Fabbri F, et al. Influence of the carrier gas flow in the CVD synthesis of 2-dimensional MoS_2 based on the spin-coating of liquid molybdenum precursors. Nanomaterials. 2024;14(21):1749. [CrossRef].
153. Cao Y, Luo X, Han S, Yuan C, Yang Y, Li Q, et al. Influences of carrier gas flow rate on the morphologies of MoS_2 flakes. Chem Phys Lett. 2015;631:30–3. [CrossRef].
154. Budimir Sacher J, Bolf N, Rogue M. Direct nucleation control with external heating loop: process system engineering, simulation and experimental investigation. Crystals. 2026;16(4):248. [CrossRef].
155. Pondick V, Woods JM, Xing J, Zhou Y, Cha JJ. Stepwise sulfurization from MoO_3 to MoS_2 via chemical vapor deposition. ACS Appl Nano Mater. 2018;1(10):5655–61. [CrossRef].
156. Li S, Ouyang D, Zhang N, Zhang Y, Murthy A, Li Y, et al. Substrate engineering for chemical vapor deposition growth of large-scale 2D transition metal dichalcogenides. Adv Mater. 2023;35(52):2211855. [CrossRef].
157. Choudhury TH, Zhang X, Al Balushi ZY, Chubarov M, Redwing JM. Epitaxial growth of two-dimensional layered transition metal dichalcogenides. Annu Rev Mater Res. 2020;50:155–77. [CrossRef].
158. Xue G, Qin B, Ma C, Yin P, Liu C, Liu K. Large-area epitaxial growth of transition metal dichalcogenides. Chem Rev. 2024;124(17):9785–865. [CrossRef].
159. Rosenberger MR, Chuang HJ, McCreary KM, Li CH, Jonker BT. Electrical characterization of discrete defects and impact of defect density on photoluminescence in monolayer WS_2. ACS Nano. 2018;12(2):1793–800. [CrossRef].
160. Fu X, Qiao Z, Zhou H, Xie D. Defect engineering in transition metal dichalcogenide-based gas sensors. Chemosensors. 2024;12(6):85. [CrossRef].

161. Liang Q, Zhang Q, Zhao X, Liu M, Wee ATS. DefectEngineering of two-dimensional transition-MetalDichalcogenides: applications, challenges, and opportunities. ACS Nano. 2021;15(2):2165–81. [CrossRef].
162. Edelberg D, Rhodes D, Kerelsky A, Kim B, Wang J, Zangiabadi A, et al. Approaching the intrinsic limit in transition metal diselenides via point defect control. Nano Lett. 2019;19(7):4371–9. [CrossRef].
163. Han X, Niu M, Luo Y, Li R, Dan J, Hong Y, et al. Atomically engineering metal vacancies in monolayer transition metal dichalcogenides. Nat Synth. 2024;3(5):586–94. [CrossRef].
164. Sun J, Li X, Guo W, Zhao M, Fan X, Dong Y, et al. Synthesis methods of two-dimensional MoS_2: a brief review. Crystals. 2017;7(7):198. [CrossRef].
165. Ding Q, Meng F, English CR, Cabán-Acevedo M, Shearer MJ, Liang D, et al. Efficient photoelectrochemical hydrogen generation using heterostructures of Si and chemically exfoliated metallic MoS_2. J Am Chem Soc. 2014;136(24):8504–7. [CrossRef].
166. Yao Y, Ao K, Lv P, Wei Q. MoS_2 coexisting in 1T and 2H phases synthesized by common hydrothermal method for hydrogen evolution reaction. Nanomaterials. 2019;9(6):844. [CrossRef].
167. Chen X, Wang C, Shi H, Li J, Wang J, Wang Z, et al. Enhanced sodium storage in MXene transition metal chalcogenides anode through dual molten salt etching. Electrochim Acta. 2025;509:145334. [CrossRef].
168. Huang S, You Z, Jiang Y, Zhang F, Liu K, Liu Y, et al. Fabrication of ultrathin MoS_2 nanosheets and application on adsorption of organic pollutants and heavy metals. Processes. 2020;8(5):504. [CrossRef].
169. Philip A, Kumar AR. Solvent effects on the electrochemical performance of few layered MoS_2 electrodes fabricated using FTO substrates. Nano Ex. 2024;5(1):015015. [CrossRef].
170. Freire RLH, Fonseca HAB, Moraes PIR, Mocelim M, Neto MMCB, Da Silva JLF. Defect-engineered MoS_2Supported transition metal clusters for electrochemical reactions. ACS Catal. 2025;15(23):20036–48. [CrossRef].
171. Getaneh SA, Magrez A, Workneh GA. Structural phases and electrochemical properties of 2D MoS_2 for supercapacitor applications. RSC Adv. 2026;16(6):4869–97. [CrossRef].
172. Dorri M, Anil Kumar MR, Zaghib K. In operando and *in situ* characterization tools for advanced rechargeable batteries: effects of electrode origin and electrolyte. J Power Sources. 2025;658:238188. [CrossRef].
173. Enyashin AN, Seifert G. Density-functional study of Li_xMoS_2 intercalates ($0 \leq x \leq 1$). Comput Theor Chem. 2012;999:13–20. [CrossRef].
174. Quilty CD, Housel LM, Bock DC, Dunkin MR, Wang L, Lutz DM, et al. *Ex situ* and operando XRD and XAS analysis of MoS_2: a lithiation study of bulk and nanosheet materials. ACS Appl Energy Mater. 2019;2(10):7635–46. [CrossRef].
175. Zhang L, Sun D, Kang J, Feng J, Bechtel HA, Wang LW, et al. Electrochemical reaction mechanism of the MoS_2 electrode in a lithium-ion cell revealed by *in situ* and operando X-ray absorption spectroscopy. Nano Lett. 2018;18(2):1466–75. [CrossRef].
176. Cen M, Feng Y, Fan S, Zhang S, Yan R, Chen B, et al. Bulk MoS_2 anodes engineered by solid-phase pre-sodiation for high-performance sodium-ion batteries. Adv Funct Mater. 2026;36(41):e74700. [CrossRef].
177. Zhang Y, Zhang L, Lv TA, Chu PK, Huo K. Two-dimensional transition metal chalcogenides for alkali metal ions storage. ChemSusChem. 2020;13(6):1114–54. [CrossRef].
178. Fan S, Gong Y, Chen S, Zhang Y. Interlayer-spacing-modification of MoS_2 via inserted PANI with fast kinetics for highly reversible aqueous zinc-ion batteries. Micromachines. 2025;16(7):754. [CrossRef].
179. Rasamani KD, Alimohammadi F, Sun Y. Interlayer-expanded MoS 2. Mater Today. 2017;20(2):83–91. [CrossRef].
180. Ren X, Zhao Q, McCulloch WD, Wu Y. MoS_2 as a long-life host material for potassium ion intercalation. Nano Res. 2017;10(4):1313–21. [CrossRef].
181. Du X, Guo X, Huang J, Lu Z, Tan H, Huang JQ, et al. Exploring the structure evolution of MoS_2 upon Li/Na/K ion insertion and the origin of the unusual stability in potassium ion batteries. Nanoscale Horiz. 2020;5(12):1618–27. [CrossRef].
182. Wang G, Zhang Y, Cho HS, Zhao X, Kim F, Zou J. Revisiting the structural evolution of MoS_2 during alkali metal (Li, Na, and K) intercalation. ACS Appl Energy Mater. 2021;4(12):14180–90. [CrossRef].
183. Pham TA, Kweon KE, Samanta A, Lordi V, Pask JE. Solvation and dynamics of sodium and potassium in ethylene carbonate from *ab initio* molecular dynamics simulations. J Phys Chem C. 2017;121(40):21913–20. [CrossRef].

184. Bogle X, Vazquez R, Greenbaum S, von Wald Cresce A, Xu K. Understanding Li^+–solvent interaction in non-aqueous carbonate electrolytes with ^{17}O NMR. J Phys Chem Lett. 2013;4(10):1664–8. [CrossRef].
185. Lv X, Li F, Gong J, Gu J, Lin S, Chen Z. Metallic FeSe monolayer as an anode material for Li and non-Li ion batteries: a DFT study. Phys Chem Chem Phys. 2020;22(16):8902–12. [CrossRef].
186. Barik G, Pal S. Defect induced performance enhancement of monolayer MoS_2 for Li- and Na-ion batteries. J Phys Chem C. 2019;123(36):21852–65. [CrossRef].
187. He H, Lu P, Wu L, Zhang C, Song Y, Guan P, et al. Structural properties and phase transition of Na adsorption on monolayer MoS_2. Nanoscale Res Lett. 2016;11(1):330. [CrossRef].
188. Olsson E, Yu J, Zhang H, Cheng HM, Cai Q. Atomic-scale design of anode materials for alkali metal (Li/Na/K)-ion batteries: progress and perspective. Adv Energy Mater. 2022;12(25):202200662. [CrossRef].
189. Sukhanova EV, Bereznikova LA, Manakhov AM, Al Qahtani HS, Popov ZI. A novel membrane-like 2D A'-MoS_2 as anode for lithium- and sodium-ion batteries. Membranes. 2022;12(11):1156. [CrossRef].
190. Di S, Ding P, Wang Y, Wu Y, Deng J, Jia L, et al. Interlayer-expanded MoS_2 assemblies for enhanced electrochemical storage of potassium ions. Nano Res. 2020;13(1):225–30. [CrossRef].
191. Ye Z, Jiang Y, Li L, Wu F, Chen R. Rational design of MOF-based materials for next-generation rechargeable batteries. Nano Micro Lett. 2021;13(1):203. [CrossRef].
192. Han M, Ma J, Luo Y, Han S, Huang Y. ZIF-67 clusters with small-size particles confined by a graphene framework as a promising lithium-ion battery anode. ACS Omega. 2025;10(15):15181–90. [CrossRef].
193. Qu B, Sun Y, Liu L, Li C, Yu C, Zhang X, et al. Ultrasmall Fe_2O_3 nanoparticles/MoS_2 nanosheets composite as high-performance anode material for lithium ion batteries. Sci Rep. 2017;7:42772. [CrossRef].
194. Xiong W, Lin J, Wang H, Li S, Wang J, Mao Y, et al. Construction of strong built-in electric field in binary metal sulfide heterojunction to propel high-loading lithium-sulfur batteries. J Energy Chem. 2023;81:492–501. [CrossRef].
195. Lee J, Choi C, Park JB, Yu S, Ha J, Lee H, et al. Optimally arranged TiO_2@MoS_2 heterostructures with effectively induced built-in electric field for high-performance lithium-sulfur batteries. J Energy Chem. 2023;83:496–508. [CrossRef].
196. Zhao Z, Luo S, Ma P, Luo Y, Wu W, Long Y, et al. *In situ* synthesis of MoS_2 on C_3N_4 to form MoS_2/C_3N_4 with interfacial Mo–N coordination for electrocatalytic reduction of N_2 to NH_3. ACS Sustainable Chem Eng. 2020;8(23):8814–22. [CrossRef].
197. Wang W, Xu M, Sun J, Zuo K, Wang X, Lan J, et al. Novel g-$C3N_{4-x}$ nanosheets/MoS_2 binary photocatalyst achieves stable construction of Z-scheme heterojunction via nitrogen defect induced 2D interface C-S bonds for efficient PMS activation and degradation of sulfamethoxazole. Environ Res. 2025;279:121888. [CrossRef].
198. Yang Y, Hu W, Liu F, Li A, Huang D, Zou R. Glucose-assisted hydrothermal synthesis of hierarchical MoS_2/C structures with expanded interlayer spacing and 1T/2H hybrid phases for enhanced lithium and sodium storage. Chem Eng J. 2025;521:166766. [CrossRef].
199. Yang Y, Zheng F, Wang L, Liu Y. 3D MoS_2/graphene oxide integrated composite as anode for high-performance sodium-ion batteries. Sci Rep. 2024;14:19231. [CrossRef].
200. Yang B, Wang Z, Yin X, Liu B, Tong X, Lu Z, et al. Nano-bowl-like carbon confined 1T/2H-MoS_2 hybrids as anode for high-performance sodium-ion storage. J Power Sources. 2024;597:234136. [CrossRef].
201. Liu X, Zhou X, Zhao S, Li J, Zhang P, Xu B. 1T MoS_2/C composites for enhanced Li-ion storage performance. Mater Lett. 2025;400:139075. [CrossRef].
202. Ruan J, Li S, Deng C, Xiao J, Zheng S, Wang F, et al. Effect of heteroatom doping and morphology tuning of CNT-derived material for potassium-ion hybrid capacitors. Chem Eng J. 2021;410:128421. [CrossRef].
203. Wu D, Le X. Research progress on applying tin disulfide in the anode of high-performance sodium-ion batteries. J Solid State Electrochem. 2026;30(1):269–300. [CrossRef].
204. Dey S, Ragupathi V. Tin chalcogenides as a prospective anode material for Li and Na-ion batteries: a mini review. Ionics. 2026;32(4):3733–48. [CrossRef].
205. Wang Z, Sun Z, Li J, Shi Y, Sun C, An B, et al. Insights into the deposition chemistry of Li ions in nonaqueous electrolyte for stable Li anodes. Chem Soc Rev. 2021;50(5):3178–210. [CrossRef].
206. Tang Z, Lei Y, Deng Y, Chen J, Liu K, Zhang C, et al. MOF-derived MoS_2/nitrogen-doped graphene aerogel for supercapacitor electrodes. Diam Relat Mater. 2025;153:112098. [CrossRef].

207. Zhang H, Wei J, Yan Y, Guo Q, Xie L, Yang Z, et al. Facile and scalable fabrication of MnO_2 nanocrystallines and enhanced electrochemical performance of MnO_2/MoS_2 inner heterojunction structure for supercapacitor application. J Power Sources. 2020;450:227616. [CrossRef].
208. Hu R, Liao Y, Qiao H, Li J, Wang K, Huang Z, et al. Electrochemical method integrating exfoliation and *in-situ* growth to synthesize MoS_2 nanosheets/MnO_2 heterojunction for performance-enhanced supercapacitor. Ceram Int. 2022;48(16):23498–503. [CrossRef].
209. Ramalingam G, Arunkumar P, Alqahtani MD, Elgarahy AM. Photocatalytic activity of microwave-assisted synthesized MoS_2/g-C_3N_4 composite for efficient decomposition of aniline green dye. J Clust Sci. 2025;36(5):171. [CrossRef].
210. Chaturvedi R, Anju, Pandey R, Singhania S, Garg A. Synergic energy storage performance of MoS_2/g-C_3N_4 composite on screen-printed carbon electrode. Electrochim Acta. 2025;539:147090. [CrossRef].
211. Gao YM, Liu Y, Feng KJ, Ma JQ, Miao YJ, Xu BR, et al. Emerging WS_2/WSe_2@graphene nanocomposites: synthesis and electrochemical energy storage applications. Rare Met. 2024;43(1):1–19. [CrossRef].
212. Wang Q, Wang Y, Zhang X, Wang G, Ji P, Yin F. WSe_2/reduced graphene oxide nanocomposite with super-fast sodium ion storage ability as anode for sodium ion capacitors. J Electrochem Soc. 2018;165(16):A3642–7. [CrossRef].
213. Liao Y, Chen C, Yin D, Cai Y, He R, Zhang M. Improved Na^+/K^+ storage properties of $ReSe_2$-carbon nanofibers based on graphene modifications. Nanomicro Lett. 2019;11(1):22. [CrossRef].